MARSHALL PLAN REPORT

In Situ Fracture Toughness of Nitronic 50

Size and strain rate effects

Eric Hintsala

In Situ TEM and SEM fracture toughness measurements are made for Nitronic 50 Stainless Steel. This is accomplished using pre-notched three point bend test specimens fabricated via Focused Ion Beam Machining. The results are analyzed to explore how fracture toughness is affected by the variables of size and strain rate.

Table of Contents:

Chapter 1: Introduction

The ultimate goal of studying the mechanical behavior of materials is to be able to precisely predict the resulting deformation from a generic applied stress state for any given material. For direct applications, knowledge of the conditions required for failure of a component is critical. Unfortunately, obtaining this knowledge requires understanding of the connection between structure, composition and properties which are complex and diverse. Even the most fundamental and small scale local processes are not completely understood, since they occur at such small length scales. By performing deformation experiments on small volumes in situ it is possible to study these local processes with unprecedented levels of characterization. These in-situ experiments can take place utilizing SEM or TEM and are a growing field of research [1-5]. These types of studies can also improve understanding in the bulk. When dealing with bulk sized components, a statistical distribution of flaws is inevitable. Due to stress concentrations and mismatch effects, deformation is usually concentrated around the largest flaws or inclusions present. This is why fracture mechanics are used universally as design criteria for industrial components. Rather than make assumptions regarding the critical flaw, small scale experiments allow direct observation and control. This allows the researcher to introduce their own flaws that are similar in scale to the microstructural flaws that are preexisting in bulk, such as grain boundaries, pre-notches, or inclusions [6-8]. The coupling of flaw control and improved characterization means that these types of experiments allows for studying fundamental deformation processes with unprecedented detail. These types of experiments are crucial input for modeling efforts; the cycle of experimental validation and model/theory development is the essence of scientific advance.

Material properties are a function of size, such that nano-volumes display very different behavior than their corresponding bulk components [1-3, 9-12]. As such, there are many direct applications of these types of experiments. As the field of nanotechnology grows, particularly with regards to MEMS and NEMS devices, precise measurements of properties at the same scale are crucial. A property change with size is linked to changes in deformation mechanisms is referred to as a "size effect." Size effects are observed both in non-constrained volumes, such as a nanoparticle or nanowhisker, and constrained volumes, as found in nanograined bulk materials and multilayered thin films. Nanograined materials are a growing field of research where the size effects are engineered to improve performance of bulk components [13, 14].

Deformation behavior can be divided into two broad types: brittle and ductile. Traditionally, metals are dominated by ductile processes while ceramics are dominated by brittle processes. However, in real materials, a mixture of both types of behavior usually observed. There is an energetic competition between these processes, and the favorable mechanism can vary locally. By applying a load to a material, an energy is applied that must be dissipated. Crystalline materials can accommodate some amount of energy initially by elastically stretching the atomic bonds in its lattice, but when the elastic limit is reached, behavior can diverge significantly. Ductile processes dissipate energy by step-wise deformation processes that result in a permanent shape change, where brittle processes dissipate energy by the formation of new surfaces. The fundamental unit of plastic (ductile) deformation is a one-dimensional crystalline defect known as a dislocation, which are nucleated and then propagate through a material. In a brittle material, the energy cost of nucleated and/or propagating dislocations is much higher and unfavorable. The differences in energy cost are based on bonding character and crystal structure. The energetics can be affected by several variables, such as temperature, strain rate, presence of

impurities and as previously mentioned, size, such that a given material may behave in a brittle or ductile manner depending on the situation. The fact that a material can transition in its behavior gives opportunities for engineering. Brittle materials have a number of attractive qualities, such as lower conductivities, transparency, high hardness and band gaps that can be engineered for use in electronic devices. A major limitation to the use of these materials is their brittleness [15, 19], so if their ductility could be enhanced, much more reliable and robust devices could be produced.

Chapter 2: Background

2.1: Basic Fracture concepts

As described in the introduction, flaws in materials are important sources of deformation activity, due to their inherent stress concentration. In particular, it is important to understand the stress fields surrounding a crack tip. Linear elastic fracture mechanics is a well-developed field and some of the essential concepts will be briefly presented here [20].

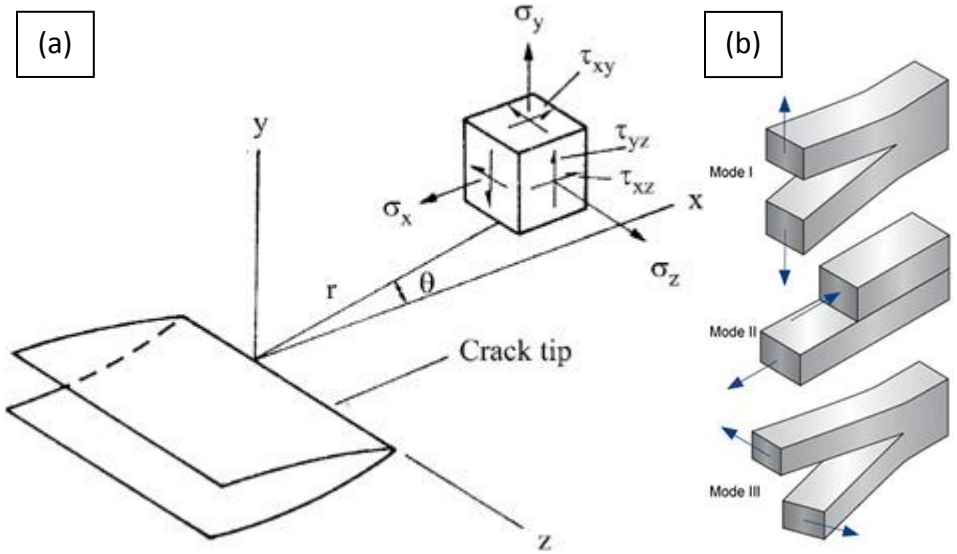

Figure 1: a) Components of a crack tip stress field b) Schematic of crack loading modes

To begin, there are three basic modes by which a crack or flaw can be extended, as illustrated in Fig. 1b. Mode I is a tensile opening mode, Mode II is an in-plane shearing mode, and Mode III is a transverse shear or tearing mode. Of the three, Mode I is the most destructive and is often the only one considered. For embedded flaws, high tensile stresses are typically present due to a hydrostatic, or triaxial, stress state. This is illustrated both in Fig 1a and described in Equation 1a-c for a perfectly sharp crack:

$$\sigma_x = \frac{K}{\sqrt{2\pi r}}\left[cos\frac{\theta}{2}\left(1 - sin\frac{\theta}{2}sin\frac{3\theta}{2}\right)\right] \quad (1a)$$

$$\sigma_y = \frac{K}{\sqrt{2\pi r}}\left[cos\frac{\theta}{2}\left(1 + sin\frac{\theta}{2}sin\frac{3\theta}{2}\right)\right] \quad (1b)$$

$$\tau_{xy} = \frac{K}{\sqrt{2\pi r}}\left(sin\frac{\theta}{2}cos\frac{\theta}{2}cos\frac{3\theta}{2}\right) \quad (1c)$$

where each stress component is labeled in Fig 1a. In Eq. 1a-c, θ represents the angle between the crack plane and the direction of interest, r is the distance from the crack tip to the point of interest, and K is known as the stress intensity factor. The stress intensity factor is given in Eq. 2:

$$K = \sigma^{\infty}\sqrt{\pi a} \quad (2)$$

where σ^{∞} is the applied far-field stress, and a is the flaw size. It can be seen that larger flaws are more destructive, but with sufficient applied stresses, even small flaws can induce large stress fields. It can also be seen from Eq 1a-c that the stresses near a crack tip are very large due to the inverse dependence on r. Of course, stresses do not truly approach infinity at the crack tip, but the presented stress field equations are accurate for most distances despite this limitation.

2.2: Griffith Criterion

One of the earliest accomplishments of fracture mechanics was the Griffith criterion [21, 22], which for a perfectly brittle material predicts the necessary stress to cause catastrophic failure from a flaw of given size based on an energy balance approach. Though perfect brittleness is generally not a realistic assumption, the Griffith criterion laid the groundwork for using energetics to predict fracture. This criterion will be re-derived here for instructive purposes. This derivation is done in two dimensions for simplicity, and so all the terms presented in the following discussion are with respect to thickness. To start with, the excess elastic energy arising from an externally applied stress that's unsupported due to a crack is given in Eq. 3:

$$U_E = -\frac{\pi a^2 \sigma^2}{E} \tag{3}$$

where a is again the crack length, σ the applied stress and E the elastic modulus. The surface energy of the crack is given by Eq 4:

$$U_S = 4a\gamma_S \tag{4}$$

where γ_S is the free surface energy. These two terms may be summed together to give the total energy of the crack, as shown in Eq 5:

$$\Delta U = U_S + U_E \tag{5}$$

Next, this is differentiated with respect to crack length and set equal to zero, to establish the minimum needed stress to extend the crack length. This is shown in Eq. 6:

$$\frac{d\Delta U}{da} = 0 = \frac{d}{da}\left(4a\gamma_S - \frac{\pi a^2 \sigma^2}{E}\right) \tag{6}$$

This, upon simplification, yields the final result shown in Eq. 7:

$$\sigma = \left(\frac{2E\gamma_S}{\pi a}\right)^{1/2} \tag{7}$$

Essentially, the Griffith criterion states that the elastic energy that is relieved by extending the crack by an increment *da* must equal the energy cost of forming new free surfaces over the same interval *da*. This is also is where the concept of a critical stress intensity factor was first introduced. A simple rearrangement of Eq. 7 gives Eq. 8:

$$\sigma_c\sqrt{\pi a} = (2E\gamma_S)^{1/2} \equiv K_{Ic} \tag{8}$$

where the subscript *c* denotes a critical value. K_{Ic} is defined as the critical mode I stress intensity factor, and is a material property which describes a materials ability to resist crack growth. Because of this, it is often referred to as the fracture toughness. Another useful term that can be defined here is *G*, such that $G = K^2/E$ and is known as the strain-energy release rate. There is a G_{Ic} which corresponds to K_{Ic} where a crack will propagate unstably towards fracture. In the case of a brittle material, G_{Ic} is simply equal to $2\gamma_S$, but as will be seen in the next section, *G* can incorporate other strain energy dissipation mechanisms. Another consequence of the Griffith criterion is that in brittle materials, fracture occurs along well defined atomic planes, known as cleavage planes. This is because the surface energy of these planes is the lowest, and have the lowest energy cost for fracture. Many redunant cleavage planes exist within a given lattice, so the one with the highest resolved stress on it will fracture first. This is reminiscent of Schmid's Law [28] for plasticity.

2.3: Plasticity corrections

For all the successes of the Griffith criterion, it does not account for plasticity. Even in many materials that are considered brittle, some amount of plasticity will occur. This reduces the accuracy of the Griffith criterion. To understand plasticity, the critical concept is the

dislocation, which is a linear defect representing a fundamental unit of plastic deformation. The original concept for a dislocation dates back many years, long before any proof of their existence was presented. This proof later came in many forms, but most notably with the invention of the Transmission Electron Microscope [23]. Any dislocation has two important vector quantities associated with it, the Burger's vector and its line vector [24, 25]. The line vector represents the boundary between deformed and undeformed regions of a crystal; for a curved dislocation at a specific point it is the local tangent. The Burger's vector represents the resulting deformation caused by the passage of the dislocation. The Burger's vector is always the same along a given dislocation. Dislocations move stepwise throughout a crystalline material under shear stresses until they terminate at a free surface, resulting in an atomic step at the surface. The combined termination of many dislocations can be summed to give an overall permanent shape change. The angle between the line vector and Burger's vector is used to define a dislocation's character; if they are parallel a screw dislocation is formed and if they are perpendicular, an edge dislocation results. Mixed character dislocations with intermediate angles between the line vector and Burger's vector also exist and are in fact the most common. Edge and screw dislocations, as limiting cases, have different stress fields associated with them, and different mobilities based on different mechanisms for moving through a material.

To understand how dislocation processes operate at crack tips, the energetics of nucleation and propagation need to be understood. The energy cost of forming a dislocation arises from the stress field of the dislocation itself and the energy cost to sever the necessary atomic bonds. Therefore, it makes sense that materials with stronger bonding, like ionic and covalent compared to metallic bonding, have a higher energy cost associated with dislocation nucleation.

In order for a dislocation to propagate through a crystalline material, a stress needs to be applied which can overcome the resistance of the lattice. This concept was introduced by Peierls, and is named the Peierls' barrier [26, 27]. The physical interpretation of the Peierls' barrier is quite complex and quantum mechanical in nature, but in general it is the lowest for dislocations that exist on the highest atomic density planes. Similarly to dislocation nucleation, materials with stronger bonding or more complicated crystal structures have higher Peierls' barriers, making dislocation processes energetically less favorable. The combination of slip plane (which contains both the Burger's vector and line vector) and slip direction (direction the dislocation propagates along) are known as a slip system. Different favorable slip systems exist in different crystal structures, such that the crystallographic direction with the lowest Peierls barrier is the one that is favored for dislocation motion. There are several redundant slip systems, but the one with the highest resolved shear stress will be the first to activate, as described by Schmid's law [28].

In materials that show high ductility, final failure is significantly different than in more brittle materials. As previously discussed, brittle materials fail on well-defined planes, which produces smooth fracture surfaces. In the case of a more ductile material, significant localized plasticity will occur at stress concentration sites, which will lead to formation of microvoids. Upon further deformation, these microvoids will grow and coalesce until the remaining material is finally torn away. A typical fracture surface for a ductile material is shown in Fig. 2a and for a brittle material in Fig. 2b. These are the limiting cases and mixtures of these two behaviors are also often observed, such as quasi-cleavage and fatigue.

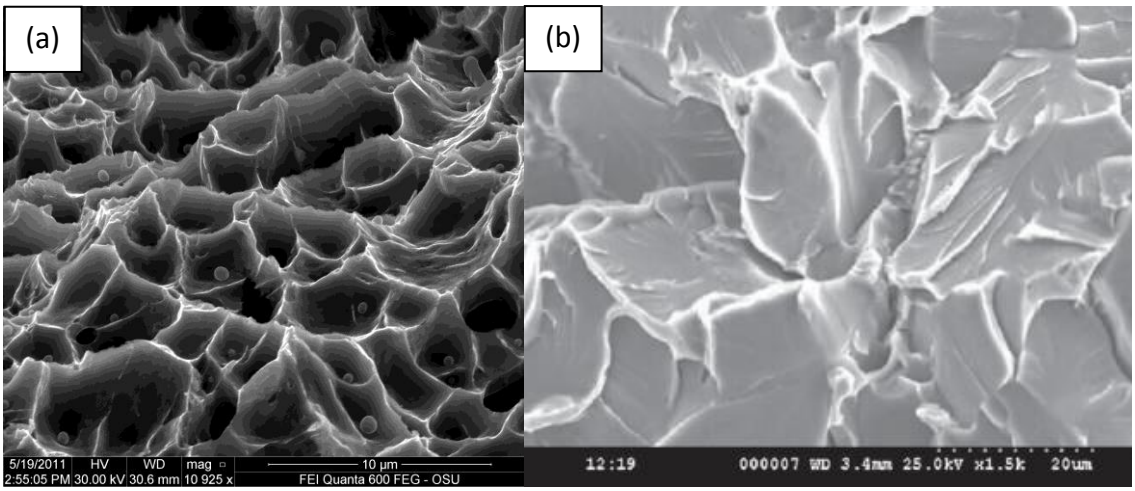

Figure 2: a) Ductile Fracture surface b) Brittle intergranular fracture

Next, the interaction between cracks and dislocations needs to be explored. The stress concentration that exists at crack tips make them favored locations for initial dislocation activity. The impact of considering plasticity at crack tips is twofold. As previously stated, dislocation nucleation and motion represent a method for dissipation of the elastic energy associated with a crack tip, and need to be taken into account for a valid determination of the fracture toughness of a material. Additionally, plasticity produces blunting or rounding of the crack tip, thereby reducing the stress concentration factor of such a flaw, which will be discussed later. To start, we can simply modify the energy balance presented in the previous section and add a term to represent energy dissipated by plasticity, as shown in Eq. 9:

$$\Delta U = U_S + U_E + U_P. \tag{9}$$

U_P is a difficult quantity to measure. All the same, several approaches have been developed over the years in the attempt to do so.

As the crack tip emits dislocations, they travel a certain distance away but will slow to the inverse r dependence of the crack tip stress field. The furthest extent of the dislocation motion is known as the plastic zone. Any region ahead of the crack tip where the stress field reaches the yield stress (the minimum stress for nucleating dislocations) is within the plastic

zone. This is shown in Fig 3, where r_y is the radius of the plastic zone [29, 30]. In a perfect elastic-plastic material (with no strain hardening due to interaction of the stress fields of dislocations), this region is incapable of bearing any more stress, so this can be thought of as an extended crack region, even though the crack is not physically there.

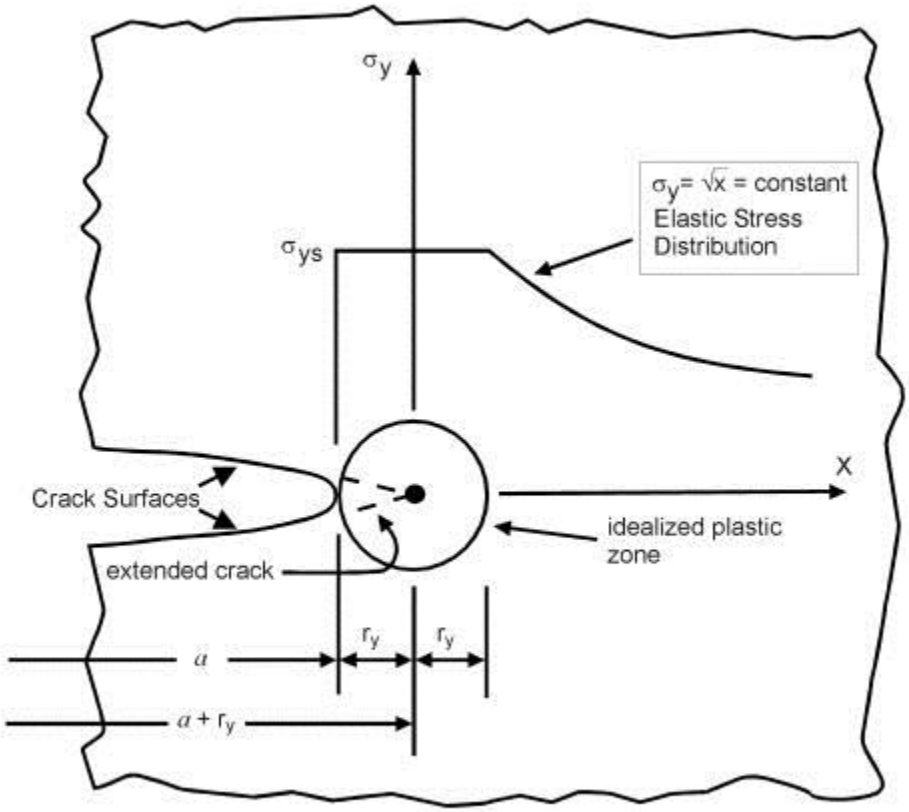

Figure 3: Illustration of the plastic zone ahead of a crack tip

The plastic zone size is approximated by Eq. 10a-b, depending upon whether the material is in plane strain or plane stress:

$$r_p = \frac{1}{2\pi}\frac{K^2}{{\sigma_{ys}}^2} \tag{10a}$$

$$r_p = \frac{1}{6\pi}\frac{K^2}{{\sigma_{ys}}^2} \tag{10b}$$

where σ_{ys} is the yield stress. In a thick specimen, the material in the interior is confined by the surrounding material such that the strain is confined to be in its plane, hence the name plane strain. In much a much thinner specimen, the material is no longer confined and can be strained out of the plane. This requires that the stresses are confined to the plane, hence the name plane stress. It should be noticed that the plane strain plastic zone size is a factor of 3 smaller, due to a suppression of yielding resulting from the increased triaxiality of the stress state.

One approach for crack tip plasticity, originally proposed by Dugdale [29-31], is crack-opening displacement, which is valid for plain stress. This approach can be described by considering the material ahead of the crack to be made up of several tensile specimens that must fail in order for crack propagation. The displacement of the tensile strip at the crack tip (as the crack tip blunts) is given by Eq. 11:

$$\delta = \varepsilon l = \varepsilon 2\rho \tag{11}$$

where ε is the strain, l is the length of the tensile specimen which is equal to 2ρ, where ρ is the radius of curvature of the crack tip. This allows definition of a critical displacement δ_c at which the fracture strain ε_f is reached, as shown in Eq. 12:

$$\delta_c = 2\rho\varepsilon_f = \varepsilon_f t \tag{12}$$

where t is the plate thickness. Since t is the transverse dimension of the tensile specimen, the right hand side of Eq. 12 is also a valid definition of δ_c. This can be related to the applied stress by Eq. 13:

$$\delta = \frac{\pi\sigma^2 a}{E\sigma_{ys}} \tag{13}$$

and since $G = \sigma_{ys}\delta$, we can determine Eq. 14:

$$G_{Ic} = \lambda \sigma_{ys} \delta_c \tag{14}$$

where λ is a geometric constant that depends on where the displacement of the crack surfaces is measured. λ is 1 if the displacement is measured at the root of the notch such that δ equals ρ. If it is measured at the widest part of the crack, i.e. furthest from the root of the crack, this can be called Δ, and may be expressed according to Eq. 15:

$$\Delta = \frac{4\sigma}{E}\left[\left(a + r_p\right)^2 - x^2\right]^{1/2} \tag{15}$$

where x is the distance from the widest part of the crack to the crack root.

A second approach for determining U_p is the J-integral [32]. Numerically, J is a strain-energy release rate that is set equal to G, but it is calculated in a special way. J is interpreted as the difference in energy as the crack is extended by an increment through the specimen by taking a path integral surrounding the crack and summing the total deformation energy contained within. J is defined in Eq. 16:

$$J = \int_{\Gamma} \left(W dy - T \frac{\partial u}{\partial x} ds\right) \tag{16}$$

where W is the strain energy per unit volume, Γ is the path of the integral which encloses the crack, T is the stress vector acting on the contour Γ, u is the displacement and ds is an increment of the path Γ. This type of integral is path-independent, allowing for flexibility in calculation. Finite Element analysis can be used to determine the stress across the contour and thereby calculate J. This method is adaptable to the type of testing being carried out. One common testing scheme is three-point bending with a corresponding J as shown in Eq. 17:

$$J = \frac{2A}{Bb} \tag{17}$$

where *A* is the area under the load-displacement curve, *B* is the specimen thickness, and *b* is the width of the specimen minus the crack length (unbroken ligament).

2.4: Ductile to Brittle Transitions

As previously explained, a given material might behavior in a brittle or ductile manner depending on several key variables. So called "Ductile-to-brittle transitions" (DBT) are complex in nature and have important ramifications for the engineering world. One of the first indications that this behavior existed (and was a real problem) is the famous cracking of the Liberty ships during WWII, shown in Fig. 4.

Figure 4: Liberty Ship which cracked in half as a result of a Ductile-to-Brittle Transition

In the liberty ship example, ferritic steel changed deformation behavior upon sailing into the cold sea, resulting in catastrophic failure. This was a result of reduced temperature, which reduces available energy for dislocation processes and thereby caused a change from ductile to brittle behavior. With all other variables held constant, a material has a Ductile-to-brittle transition temperature (DBTT). The DBTT is higher in materials with a larger Peierls' barrier or more boundaries to dislocation motion, due to less available slip systems. The yield stress at

which dislocations propagate freely through the material can be described as a sum of two components as shown in Eq. 18:

$$\sigma_{ys} = \sigma^* + \sigma_i \tag{18}$$

where the yield stress, σ_{ys}, is the sum of the constant internal stress σ_i which contains resistance to dislocation motion from obstacles and lattice resistance and the thermal dependent stress σ^*. As the temperature drops, σ^* is increased, requiring a concurrent increase in σ_{ys}. Eventually a threshold temperature will be reached where brittle fracture will be preferred to plasticity. The resulting change in K_{Ic} is shown schematically in Fig. 5.

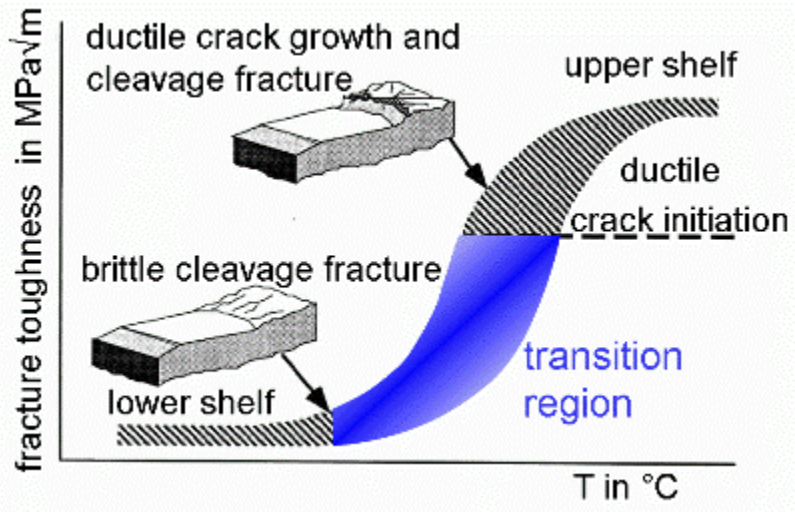

Figure 5: Schematic of rapid change in fracture toughness with temperature near a BDTT

The first to possibly discuss a thermal component of the yield stress was St. John [15]. This later developed into various dislocation nucleation controlled and dislocation propagation controlled approaches, both static and dynamic, and is a continuing area of research [16-18]. A metal typically exhibits a "soft transition" where K changes relatively slowly over a range of a few degrees. In semiconductors and ceramics, however, a "hard transition" is usually observed where K swiftly climbs with increasing temperature.

One possible physical interpretation is that the ability for a crack tip to emit dislocations depends most critically upon rapid movement of previous dislocations away from a crack tip. As dislocations have a stress field associated with them, they can exert a large back stress on the dislocation source, which increases the stress needed to nucleate subsequent dislocations. Dislocation motion can be described as an Arrhenius equation with an activation energy. In a metal (with soft transitions), this can be modified to be stress dependent by subtracting the thermal component of the yield stress multiplied by the activation volume, as shown in Eq. 19:

$$H_\sigma = H_0 - \sigma^* V^* \tag{19}$$

where H_σ is the stress-free activation energy, H_0 is the base activation energy, σ^* is the thermal stress and V^* is the activation volume. The activation volume is the volume within which a process occurs. For dislocation motion, V^* is b^2 (with b the Burger's vector) the deformation area induced by a dislocation, multiplied by the distance it has traveled. Multiplying V^* by the applied stress gives an energy for dislocation motion. Temperature has a profound effect upon dislocation velocity, a modified Cottrell formulation of dislocation velocity is shown in Eq. 20 [33, 34], with the stress free activation energy from Eq. 19:

$$v = v_0 \, exp \left[- \frac{(H_0 - \sigma^* V^*)}{kT} \right] \tag{20}$$

where v_0 is the velocity coefficient, v is the dislocation velocity, k is Boltzmann's constant, and T is the absolute temperature. Furthermore, if we consider the local process of dislocation emission from a crack tip as in [76], the critical strain energy release rate, G_{Ic}, can be expressed as Eq. 21:

$$G_{Ic} = \frac{\eta_0 V^* \sigma^* \varepsilon_p}{\mathrm{b}^2} \tag{21}$$

where η_0 is a constant based on Poisson's ratio, V^* is the activation volume for dislocation emission from the crack tip, b the Burger's vector, σ^* the thermal component of the yield stress and ε_p the plastic strain. As such, G_{Ic} is proportional to the plastic strain energy in the activation volume divided by the area of initiation of b^2. In order to combine Eq. 20 and Eq. 21, we need to consider the effect of strain rate, which is done next.

2.4.1 Strain Rate Effects:

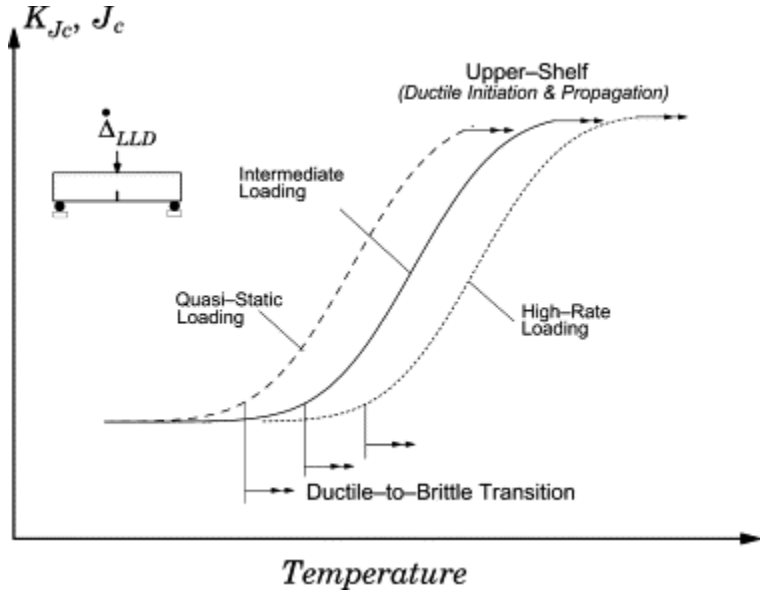

Figure 6: A general shift in BDTT due to a change in strain rate

Strain rate has an effect on the BDTT [35], which is shown schematically in Fig. 6. It can be seen that increasing strain rate reduces ductility and increases the BDTT. Why this occurs can be shown with the Orowan equation, which is presented as Eq. 22:

$$\dot{\gamma} = \rho b v \tag{22}$$

where $\dot{\gamma}$ is the shear strain rate, ρ is the dislocation density and v is the velocity of dislocations. By increasing the strain rate, this necessitates an increase in v as ρ and b are constant. However, the velocity of dislocations is limited based on the amount of thermal energy available as

accomplished in the previous section. As strain rate is increased, the fracture toughness decreases as more of the deformation is taken up by brittle processes. Utilizing Eqs. 20-22 results in Eq. 23, which combines the effect of these variables into a simple analytical model:

$$G_{Ic} = \left\{\frac{V^*\Psi_0\sigma^*}{b^2\dot{\varepsilon}_p}\right\}\exp\left\{-\frac{H_0-\beta\sigma^*V^*}{kT}\right\}. \quad (23)$$

with Ψ_0 and β as fitting parameters. This model is the focus of a paper currently under review for publication.

2.5: Size Effects

Materials properties are defined by quantities such as stress and strain, which are normalized with respect to a specimen's dimensions, allowing properties to be size-independent. Despite the convenience of this approach, this is not valid when the size of the specimen is reduced so that it is comparable to the length scale over which the deformation mechanisms operate [12]. When this occurs, new mechanisms become favorable and properties change dramatically. In terms of mechanical properties, fracture toughness, yield strengths and work-hardening are all known to undergo strong size effects at the submicron regime [1-3].

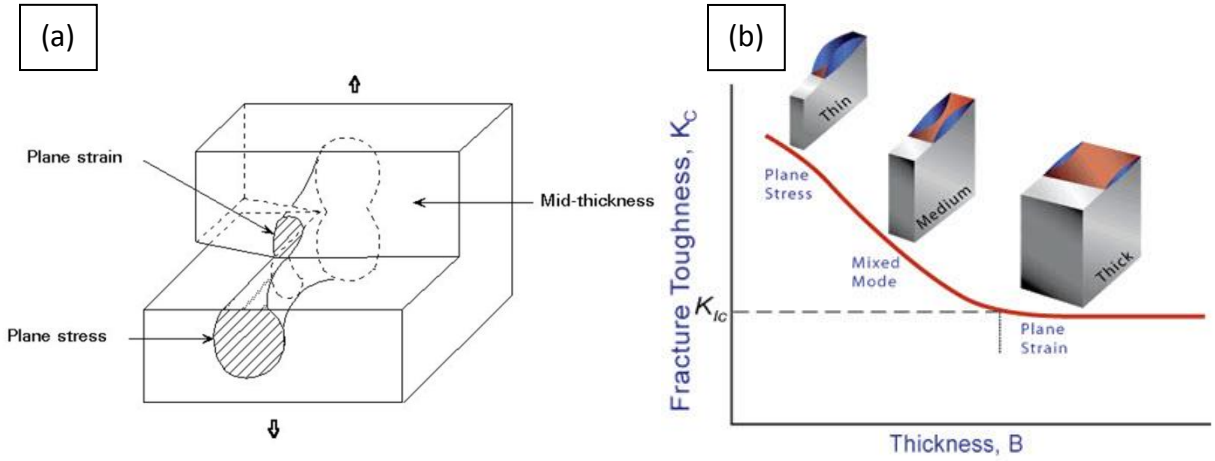

Figure 7: a) Illustration of the shape of plane stress and plane strain plastic zones b) Decrease in fracture toughness with increasing thickness due to the larger portion of the material being in plain strain

One classical size effect is the transition from plane strain to plane stress with reduced thickness, which is illustrated in Fig. 7a. This transition results in suppressed plasticity and lower energy dissipation at the crack tip as previously discussed, and a corresponding decrease in fracture toughness as illustrated in Figure 7b. This effect surfaced dramatically in early airplane design, where in order to strengthen components the thickness was increased, but the opposite result was achieved. Plane stress vs. plane strain is not the only size effect that can be observed with regards to fracture toughness [36, 37]. A size dependent brittle-to-ductile transition at constant temperature was observed by Ostlund et al. in Silicon [37]. Figure 8 shows a DBT with a very subtle decrease in Silicon pillar diameter from 400nm to 310nm. The reasons behind this behavior are somewhat uncertain. It was proposed in the paper that when the size of the pillar was reduced enough, the leading partial dislocation could terminate at the pillar surface before the trailing partial was nucleated. This explains the ductile transition when one considers that the trailing partials have lower mobility and produce a drag on the leading partial.

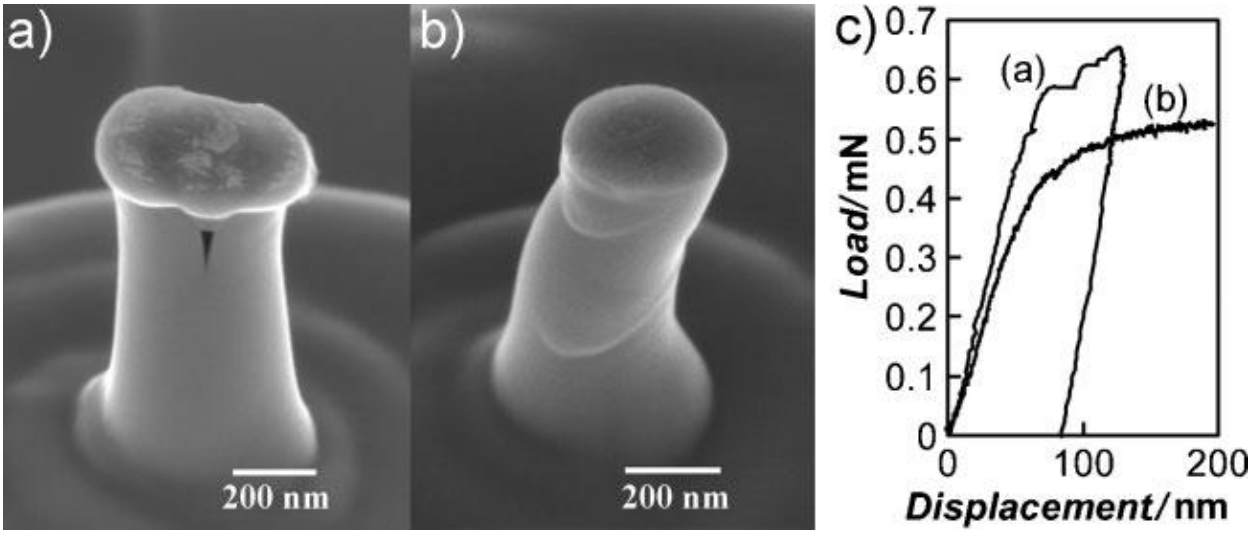

Figure 8: A BDT based solely on size effects in Si. The pillar diameter on the left is 400nm, and 310nm on the right.

Other types of size effects have been observed as well, generally concluding that the greater the reduction in size, the higher the toughness [1, 2]. The underlying physical mechanisms of size effects are elusive as they challenge the limits of our characterization capabilities and are an area of active research.

Hopefully the background section has illustrated the immense complexity and inter-dependence of several variables when it comes to deformation processes and DBTs and what the consequences may be for engineering design. It is imperative that continued experimentation and modeling being conducted to continue to develop our understanding. The purpose of this study is to add to this pool of knowledge by attempting to develop novel methods for in-situ fracture toughness testing.

Chapter 3: Experimental Methods

3.1: Material Introduction

The material being used in this study is an austenitic steel alloy, Nitronic 50. It is a specialized alloy utilized for its high corrosion resistance and fracture toughness, while still possessing high strength. The "Nitronic" comes from the 0.50% N in the material, which added to increase the strength via interstitials that can drag dislocations. The high Ni content stabilizes the austenite phase, and the high Cr content grants protection from corrosion via surface pacification. Such highly alloyed steel only ends up having about 60% Fe content. The chemical requirements for Nitronic 50 are shown in Table 1.

Table 1: Chemical Composition of Nitronic 50

Chemical Requirements							
	Ni	Cr	Mo	Mn	C	Si	Fe
Max	13.5	23.5	3.00	6.0	0.06	1.00	Bal
Min	11.5	20.5	1.50	4.0			

Nitronic 50 is most commonly employed in harsh chemical environments, for example in chemical plants and sheathing for light water nuclear reactors. As such, understanding of the resistance to embrittlement and the behavior of the DBTT is of great interest. Fig. 9a shows a typical light water reactor that Nitronic 50 could be utilized in, and Fig. 9b shows a chemical plant component made of Nitronic 50.

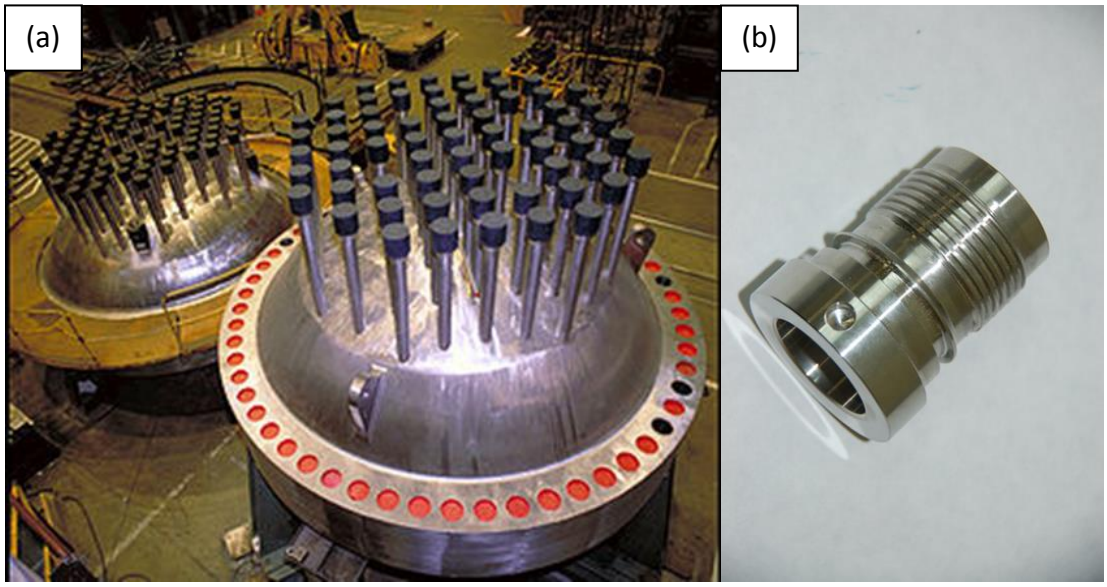

Figure 9: a) Light water nuclear reactor b) Chemical plant fitting made of Nitronic 50

3.2: Bending beam geometry standards:

In order to test fracture toughness, a number of configurations may be utilized. One popular test method is three point bending. A basic bending beam schematic is shown in Fig. 10. As a crack advances through the material, the mode I loading continues to be focused directly on

the crack tip which is placed directly opposite the applied load. Simple beam theory can show that the bending stress is in tension on the bottom surface of the beam as shown in Fig. 10, and in compression on the top surface. The transition between these is linear, such that the maximum stress states occur at the outermost fibers of the beam.

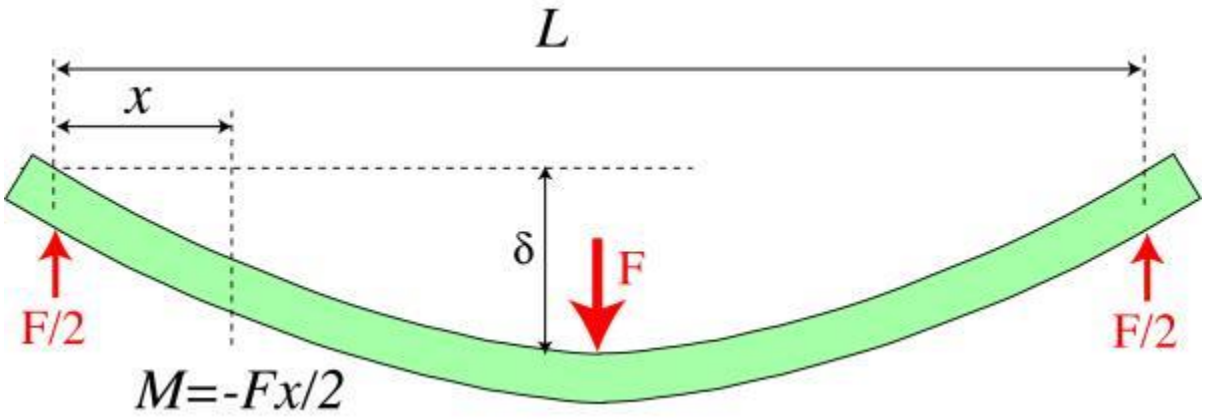

Figure 10: Schematic of the forces in a three point bending test

There exists an ASTM geometry standard for bending beams, with a corresponding empirical analysis method as shown in Eq. 25a&b [38, 39]:

$$K_I = \frac{PL}{BW^{3/2}} Y \tag{24a}$$

$$Y = \frac{3(a/W)^{1/2}\left[1.99 - a/W(1-a/W)\left(2.14 - \frac{3.93a}{W} + 2.79\left(\frac{a}{W}\right)^2\right)\right]}{(1+2a/W)(1-a/W)^{3/2}} \tag{24b}$$

where *P* is the load applied, *L* is the length, *B* is the thickness, *W* is the width, and *a* is the crack length. The corresponding required aspect ratio is 4:2:1, for length to width to thickness. Additionally, a notch is placed in the center of the beam lengthwise, opposite to where the load is applied from the tension surface to the half the width. This is shown as an illustration in Fig. 11. In this illustration, the dimensions of the beam are suitable for use in a TEM, as ~100nm thickness or less is required for transmission of the beam. Other sample sizes will be tested, as will be described, but the same aspect ratio is maintained throughout.

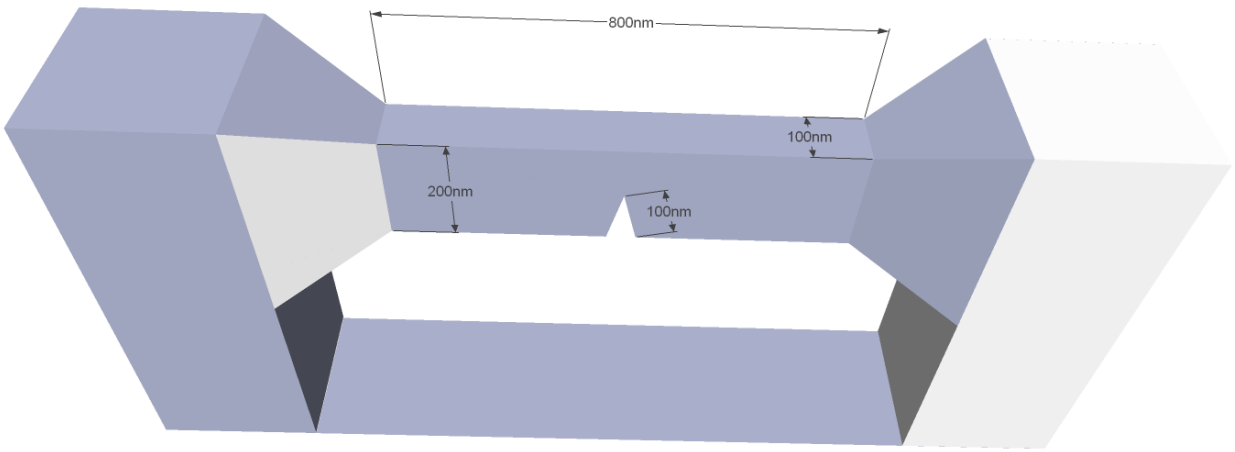

Figure 11: Sketch of the geometry utilized for bending beams in this study; the aspect ratios are maintained for all beam sizes

It should be noted that the ASTM E 399 method is designed for use on bending beams with free ends, rather than clamped to the substrate as depicted here. However, there is no way to avoid the clamping of these beams for in-situ experiments, as will be explained, and the clamped geometry offers some advantages of its own, despite the limitation of more difficult analysis.

3.3: Sample preparation

The most popular method employed for fabrication of test specimens on the micron and submicron scale is by Focused Ion Beam (FIB) milling. The FIB instrument, pictured in Fig. 12a, can cut away material via bombardment with high energy Ga+ ions, knocking away atoms of the host material. This is shown schematically in Fig 12b.

Samples were taken from a 20% cold-rolled bar provided Idaho National Laboratories. This bar was then sliced down to 2.5mmx2.5mmx1mm pieces via electrical discharge machining. Electrical discharge machining was used to limit the amount of plastic deformation induced into the material. Next, these small pieces were thinned used conventional polishing to

a thickness of approximately 100μm. These pieces were then electropolished selectively using a stop-off lacquer to mask about ¾ of the sample. The edge left exposed was then thinned selectively, down to approximately 10μm. This region was then suitable for FIB milling, as there are practical limitations to the amount of material that can be removed with the FIB. The sample was placed in a holder that was compatible with FIB, SEM and TEM as in [77] and as shown in Fig. 14a.

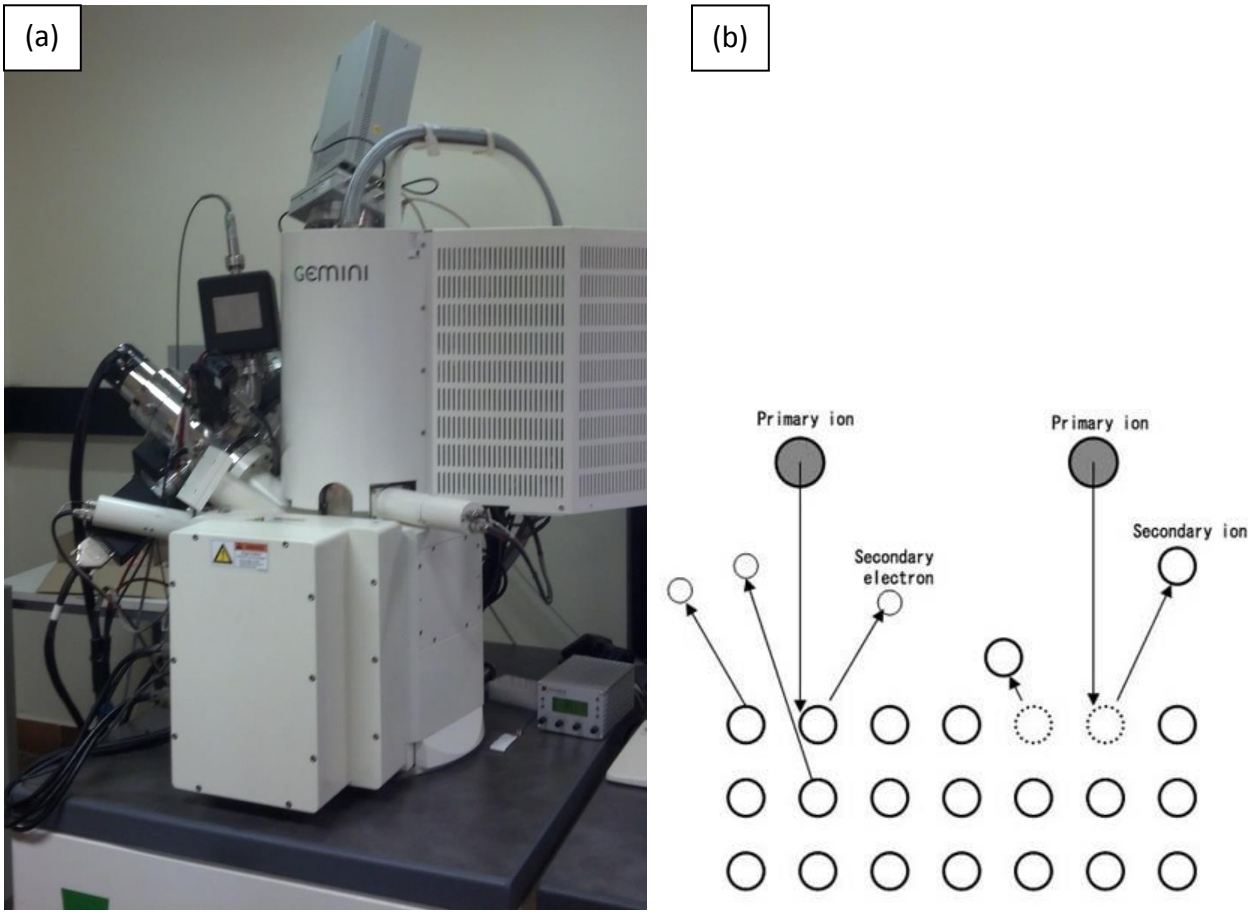

Figure 12: a) Picture of the Zeiss Gemini FIB b) Schematic of the milling process utilized by FIB

Several sizes of specimens were fabricated to explore any size effects. The three beam thicknesses investigated were: 100nm, 500nm, and 2500nm. FIB machining was accomplished by multiple steps shown schematically in Fig. 13, with 30keV accelerating voltage. First, the electropolished edge was cut flat using a large beam current of 10 nA. The sample was then

turned and reinserted into the FIB and cut on both sides to produce lamellae of thickness appropriate for the size of samples being fabricated, typically 3x thicker than the final bending beam geometry, utilizing 10nA current. At this point, the beam current was reduced to 0.5nA to cut the basic shape of the bending beams. Next, smoothing the sides and removing FIB tapering was performed. This was accomplished by using a beam current of 50pA and tilting by 2° into the side walls of the bending beam. The final step was introducing the pre-notch into the center of the beam, cut through half the width. For this step, a very minimal current of 10pA was used in an attempt to produce the sharpest notch possible. An example of a finished beam is shown in Fig. 14b.

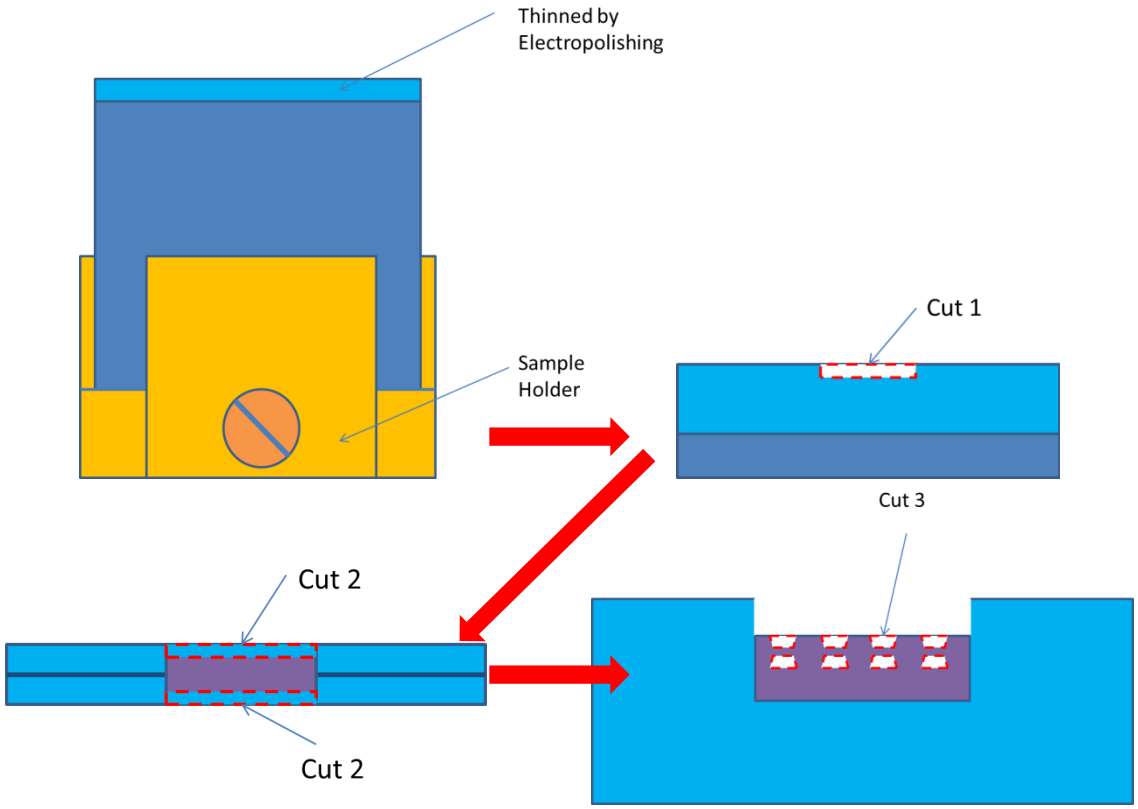

Figure 13: Illustration showing the multistep process used to fabricate bending beam specimens

For the 100nm beams, prenotching by the FIB was precluded by the high inherent beam width of the FIB of about 100nm. This means that for a 100nm beam, the notch as fabricated by the FIB was about 200nm thick, or about ¼ of the length of the beam. As this is unacceptably

blunt relative to the specimen size, an alternate method for pre-notching the 100nm beams was needed. This was accomplished by utilizing the fully converged beam in the TEM. A fully converged 200keV beam is capable of cutting through most materials in a few seconds, by virtue of local heating and knock-on damage accumulation eventually sputtering the material away. By operating the TEM in diffraction mode during this process, the center disc shows an image of the notch as its being fabricated, so that the TEM beam can be appropriately moved to fabricate a notch.

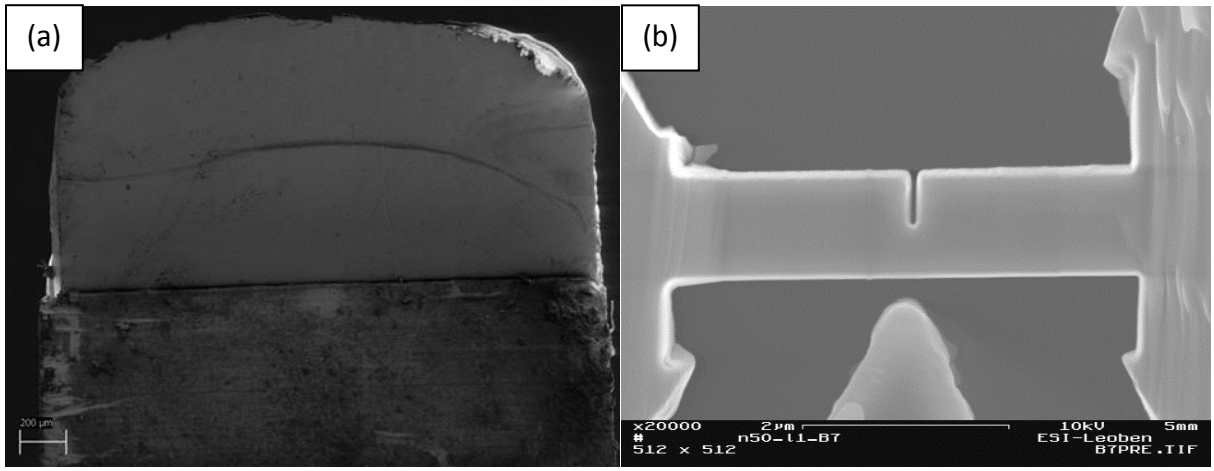

Figure 14: a) SEM micrograph of the lamellae b) A SEM micrograph of a completed bending beam sample

3.4: Testing methods

The FIB-fabricated 3-point bending beams were tested with two separate in-situ testing instruments, one for use in the SEM and one for use in the TEM. The 500nm and 2500nm thick beams were too thick to achieve electron transparency, thus requiring testing in the SEM. The in-situ SEM instrument utilized was an Asmec system. Fig. 15a shows the basic arrangement of the testing apparatus, with the electron beam column, indenter and sample. The door to the SEM is open and when it is closed the sample will slide to be in-line with the indenter. The Asmec system is inside of a Zeiss Leo 982 SEM as shown in Fig. 15b. Imaging was performed using 10

keV accelerating voltage and in secondary electron mode. Testing was performed utilized a wedge geometry tip and in displacement control, for better sensitivity.

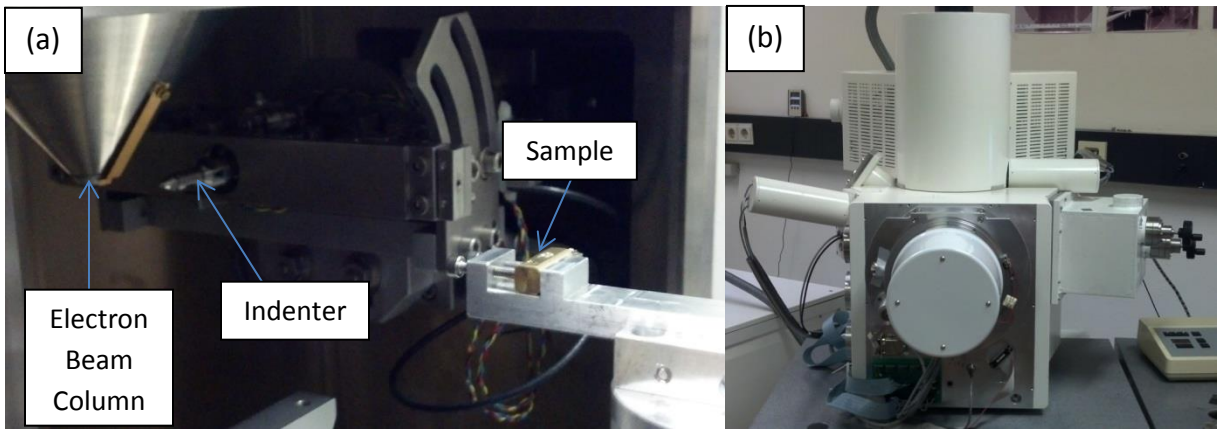

Figure 15: a) The Asmec indenter system b) The Zeiss Leo 982 SEM the Asmec is housed in

For the TEM experiments, a Hysitron PI-95 Picoindenter holder was utilized. It is essentially a modified TEM holder that is equipped with an indenter. The end of the holder is shown in Fig. 16. Testing was performed in-situ an image-corrected JEOL 2100F operating at 200keV.

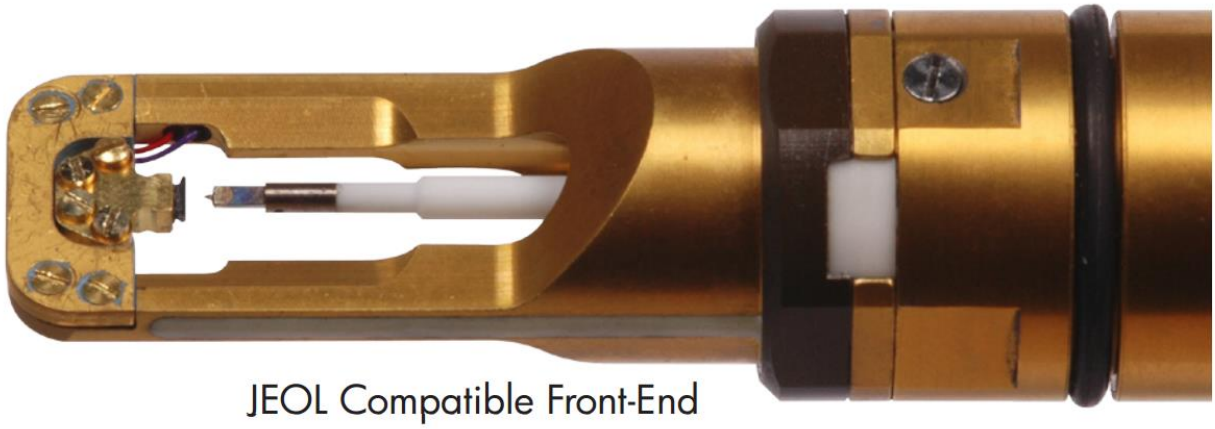

Figure 16: End of the Hysitron PI-95 PicoIndenter TEM Holder

Electron Backscatter Diffraction (EBSD) was performed on the 2500nm beams between test cycles, to track the corresponding crystallographic changes induced by the plastic deformation occurring. This was also attempted for 500nm beams, but their size was a bit too small to acquire useful signal for EBSD analysis. The instrument used to perform the EBSD

analysis is shown in Fig. 17a. For reference, Figure 17b shows an EBSD scan of bulk polished Nitronic 50; the average grain size is approximately 10um with very subtle (111) texture.

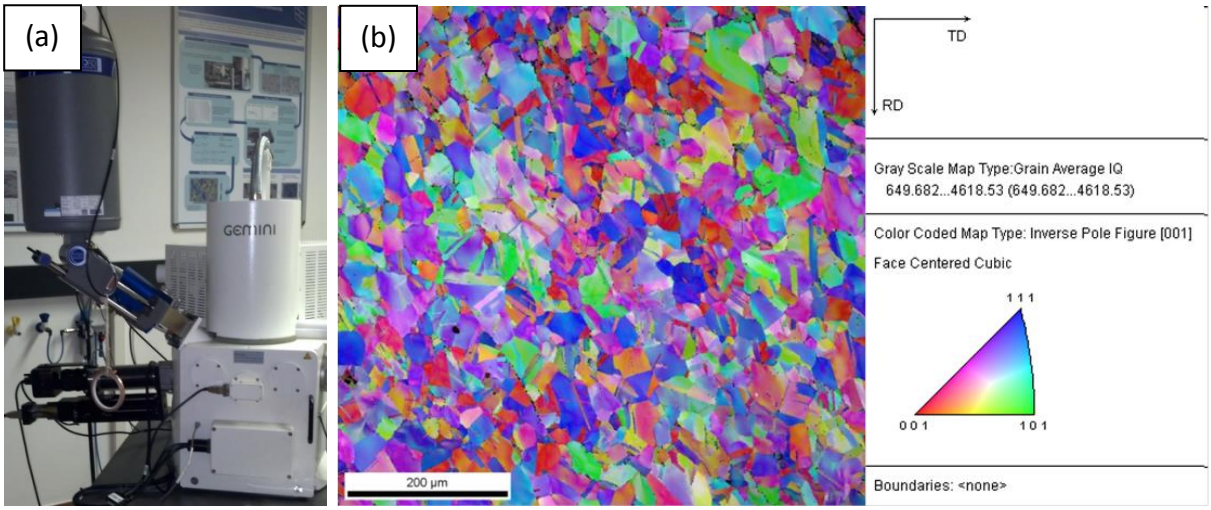

Figure 17: a) Picture of the Zeiss SEM the EBSD measurements were carried out in b) EBSD of polishing Nitronic 50

3.5: Some additional considerations

3.5.1: Doubly clamped Beams

As previously mentioned, there is one important difference between the specimens used in this testing and standard 3-point bend tests: the constraint of the ends. Specifically, the ends of a standard 3-point bend test are free, while in the presented geometry, they are fixed. The primary effect of having fixed ends of a bending beam is that the ends would like to bend downwards in response to the center of the bending beam being bent upwards. The fixing prevents this and introduces an additional stress field into the beam. The ends need to at least be partially fixed for FIB-fabricated bending beams, which was illustrated by describing the sample fabrication scheme. The only other option for bending sample geometry at this size is a single cantilever as utilized in [68] and others. This geometry has the advantage of easier analysis. However, Jaya et al. [40, 41] showed that doubly clamped three-point bending beams possess inherently higher stability both in terms of position and stress intensity factor than single

cantilevers. Additionally, doubly clamped beams allow for better visibility of the crack and the ability for post-mortem analysis. Besides this, high amounts of plasticity are expected in these samples that would limit the effectiveness of elastic analysis methods anyways. Appropriate energetic methods such as J-integrals should still be valid for this geometry, but more advanced Finite Element Methods should still be performed to properly analyze the fracture toughness.

3.5.2: FIB-notches

One issue that requires some attention is the use of the FIB to produce the pre-notch in these bending beam specimens. Analysis methods assume a perfectly sharp crack, which is not achievable by FIB machining. Focusing of the ion beam is imperfect and user error will also have a small impact. The result is that FIB notches typically have a finite radius of curvature of about 30nm, even when well-focused with the smallest aperture possible. The result of this radius of curvature is that the stress field emanating from the notch is reduced, as can be shown by Eq. 25a-c. This is the corollary of Eq.1a-c, but corrected for the presence of a notch with radius of curvature ρ:

$$\sigma_{xx} = \frac{K_I}{\sqrt{2\pi r}}\left(cos\frac{\theta}{2} - \frac{1}{2}sin\theta sin\frac{3\theta}{2} - \frac{\rho}{2r}cos\frac{3\theta}{2}\right) \tag{25a}$$

$$\sigma_{yy} = \frac{K_I}{\sqrt{2\pi r}}\left(cos\frac{\theta}{2} + \frac{1}{2}sin\theta sin\frac{3\theta}{2} + \frac{\rho}{2r}cos\frac{3\theta}{2}\right) \tag{25b}$$

$$\sigma_{xy} = \frac{K_I}{\sqrt{2\pi r}}\left(\frac{1}{2}sin\theta cos\frac{3\theta}{2} - \frac{\rho}{2r}sin\frac{3\theta}{2}\right) \tag{25c}$$

It can be seen from Eq. 25c that the larger the radius of curvature of the notch, the more the shear stress is reduced, which may have a significant effect on dislocation processes. Another way of viewing the problem was developed by Drory et al. [43] and is presented as Eq. 26:

$$K_{Ic}' = \left(1 + \frac{\rho}{2x}\right) K_{Ic} \tag{26}$$

where the effective stress intensity factor K_{Ic}' is presented as a reduction of the ideal K_{Ic}. The ratio of the radius of curvature to somewhat ambiguous length scale factor, x determines the magnitude of this effect. This was later refined by Pugno et al. [42, 44], who introduced an asymptotic correction, which is presented as Eq. 25:

$$K_{Ic}' = \sqrt{1 + \frac{\rho}{2d_0}} K_{Ic} \tag{25}$$

where d_0 is given by Eq. 26:

$$d_0 = \frac{2}{\pi} \frac{K_{Ic}^2}{\sigma_u^2} \tag{26}$$

where σ_u is the ultimate strength of the material. Taking the ultimate strength of 1 GPa measured previously from pillars of Nitronic 50 of a similar size (1.5um diameter) as shown in Fig. 18, the bulk K_{Ic} of 167 MPa-m$^{1/2}$, and a generous value for the radius of curvature of 100nm, one gets a correction factor of 1.0000028. It can be seen that this correction is of minor concern.

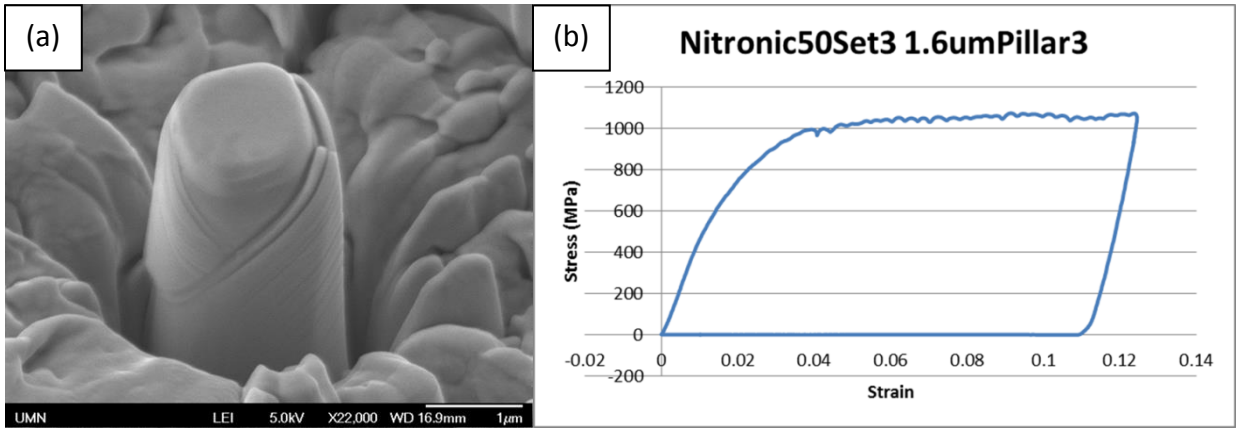

Figure 18: a) SEM micrograph of Nitronic 50 pillar post-deformation b) Corresponding strain-strain curve

3.5.3: FIB Damage

The subject of gallium damage due to FIB machining is still debated and depends on the material; some have shown little significant effect on mechanical properties while others have shown fairly large effects [45, 46]. There are some techniques to revert or minimize gallium damage [49]. Gallium damage can be reduced by stepwise decreasing the strength of the gallium beam as the final geometry of the test specimen is approached [48]. One can also utilize deposition of protected layers via a Gas injection system, which will absorb FIB damage. These layers can be then removed at the minimum FIB power later to reduce the amount of damage induced. FIB damage can also be reverted by annealing the gallium out of the test specimen. This approach was introduced by Kiener et al. [47]. For this study, stepwise reduced beam current was the only measure taken to reduce FIB damage as annealing may change the distribution of alloying agents in the specimen and protective coatings are difficult to work with at small scales.

Another possibility is to utilize a different fabrication method such as VLS growth with a template or Electron Beam lithography. As a brief comparison, FIB techniques have the advantage of increased control compared to other techniques, resulting in better final specimen geometry. For the geometry required for these specimens, these alternative methods would not be applicable.

Chapter 4: Results

4.1: 2500nm Beams

4.1.1: $0.1s^{-1}$ Strain rate

As previously mentioned, EBSD scans were taken between test cycles from the 2500nm thick beams by taking the sample out of the in-situ testing SEM and inserting it into the EBSD equipped SEM. This had twofold disadvantages, firstly that the alignment of the indenter with its previous indentation was not perfect and that the sample was contaminated by the exposure to air. The first issue will manifest itself in the load-displacement data for all the 2500nm beams as a reduced elastic loading slope. This is due to a scraping contact between the indenter and the previously existing impression. For this reason, alignment of the data from the multiple tests was not straightforward. The contamination had the effect of obscuring the SEM and EBSD data obtained, which increases with the number of test cycles.

The IPF maps showing grain orientations for 2500nm beam 1 are shown in Fig. 19 and the IQ maps with grain boundaries is shown in Fig. 20. Fig. 21 shows the maps of the local misorientation compared to the average grain orientation. For all the EBSD figures presented, the cycle number is increasing from left to right.

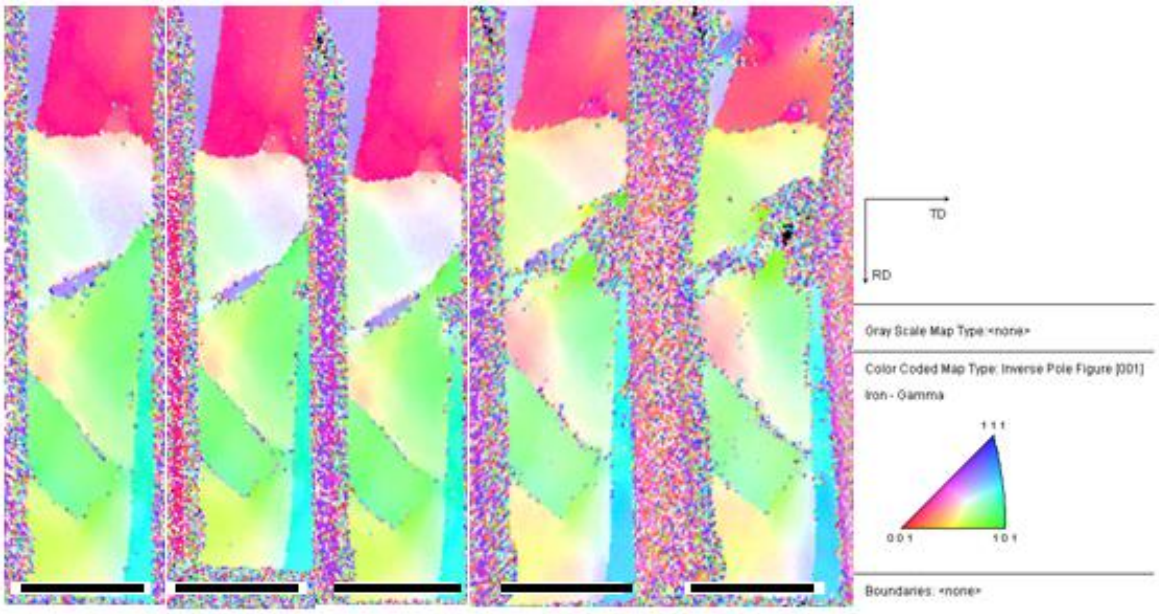

Figure 19: IPF Maps of 2500nm beam 1 after each testing cycle, scale bar 5µm

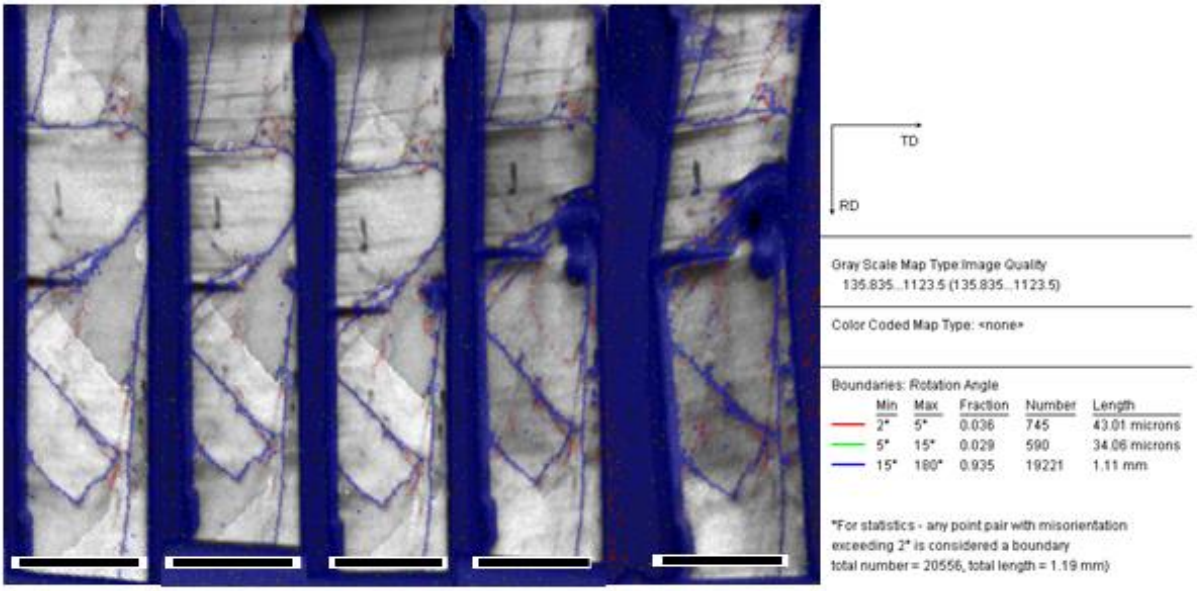

Figure 20: IQ Maps with highlighted boundaries of 2500nm beam 1 after each testing cycle, scale bar 5µm

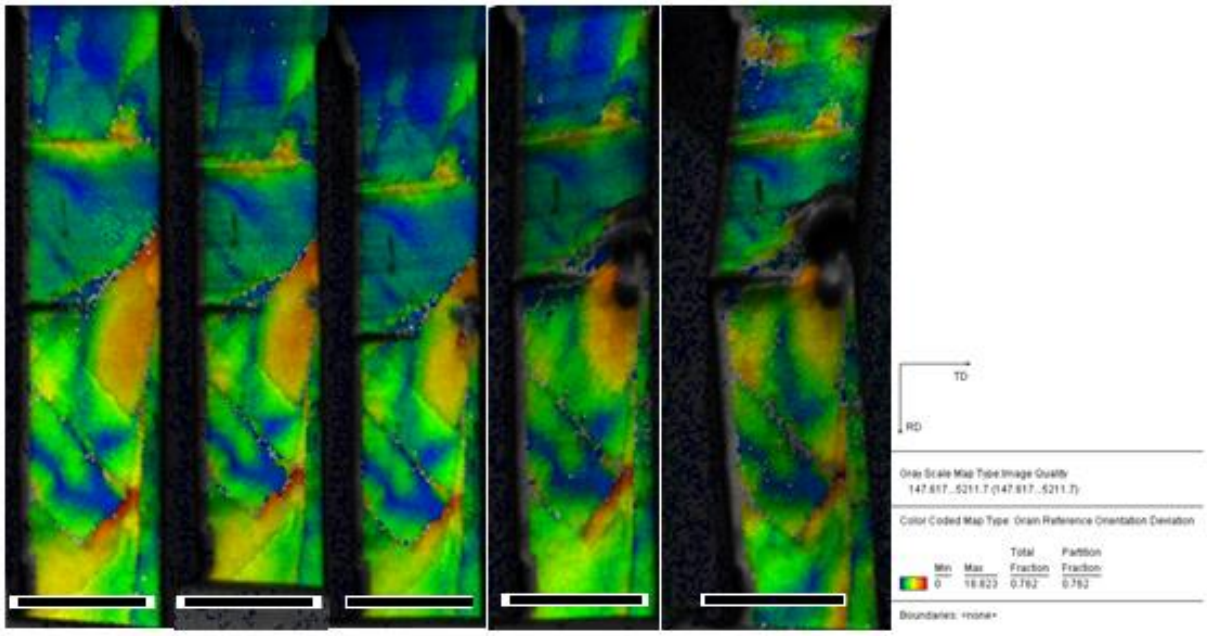

Figure 21: Local misorientation relative to the grain average for 2500nm beam 1 after each testing cycle, scale bar 5μm

As can be seen in Fig. 19-21, as deformation increases from left to right, some concurrent changes in the grain orientations also arise. This is particularly notable in scans 4&5, as the beam has undergone significant plastic deformation at this point. The pre-notch is on the left-hand side; opposite to this there is a growing region that produces no EBSD signal which corresponds to the residual impression left behind by the indenter. In the load-displacement curve presented in Fig. 22, the corresponding 4th and 5th tests show some evidence of curling over, which is indicative of plasticity, which is reflected appropriately in the EBSD data. In Fig. 19, some significant reorientation occurs in the center of the beam around the crack, as well as near the ends where the beam is fixed, especially in scans 4&5. These are the locations of highest stress, as previously discussed in the background section. An additional curious feature is revealed in Fig. 20; it can be seen that some minor boundaries two in the lower portion of the beam can be seen to disappear in the fourth frame. Fig. 21 illustrates strong local reorientation as well, decreasing in misorientation with increasing deformation.

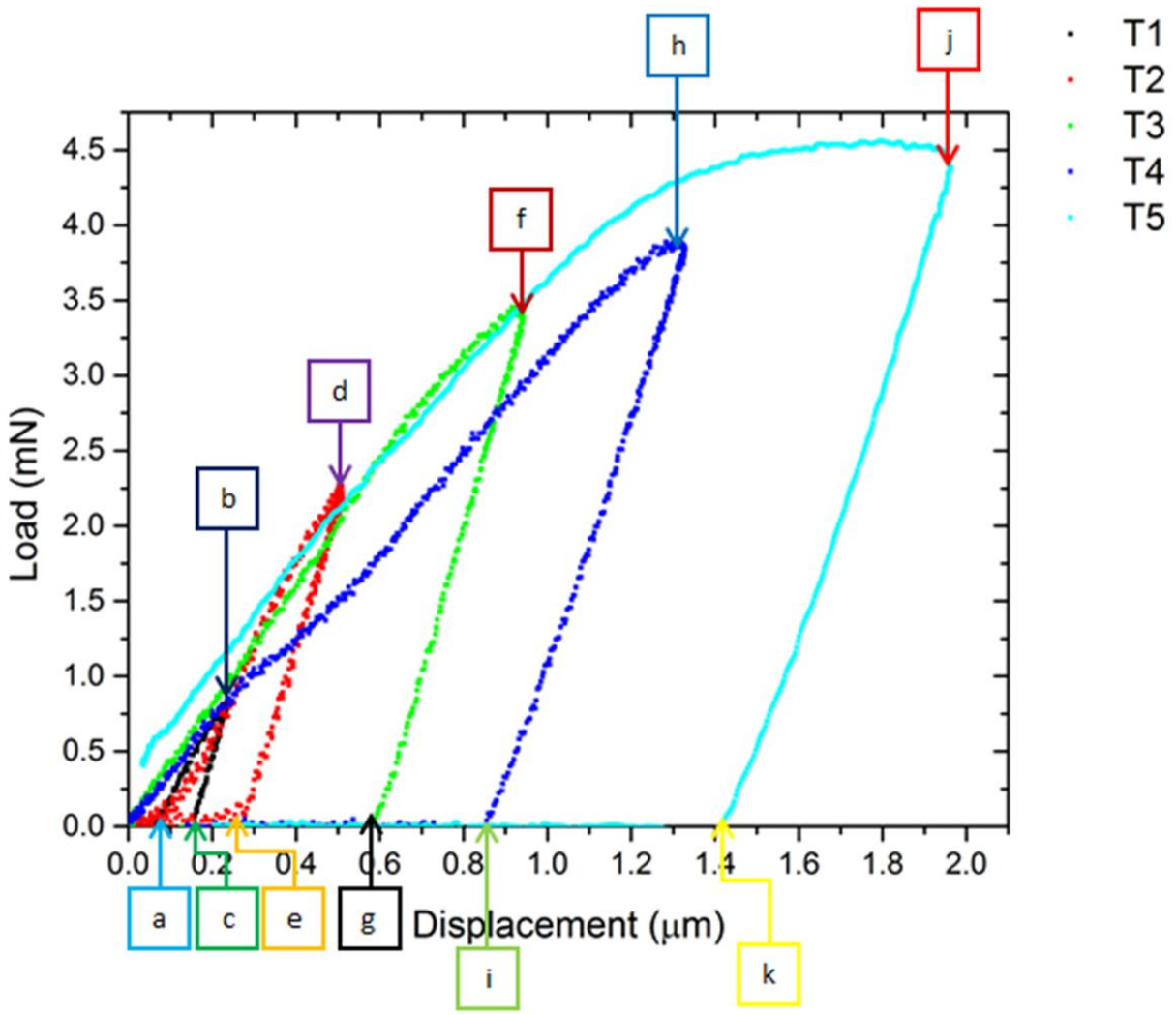

Figure 22: Load-displacement curve for 2500nm beam 1, with letters designating locations of screenshots from the corresponding video

Fig. 23 presents frames from the video recorded during the multiple tests, with letters in the upper left corresponding to the points indicated in Fig. 22. It can be seen from these frames, as suggested by the EBSD data in Fig. 19-21, that the deformation of the beams is highly plastic, as the crack does not advance significantly, but opens dramatically. A large piece of contaminantion appears during the test due to taking the specimen being taken out of vacuum. Though the indenter obscures the field of vision, it should also be noted that the impression left from the indenter is steadily growing throughout the test.

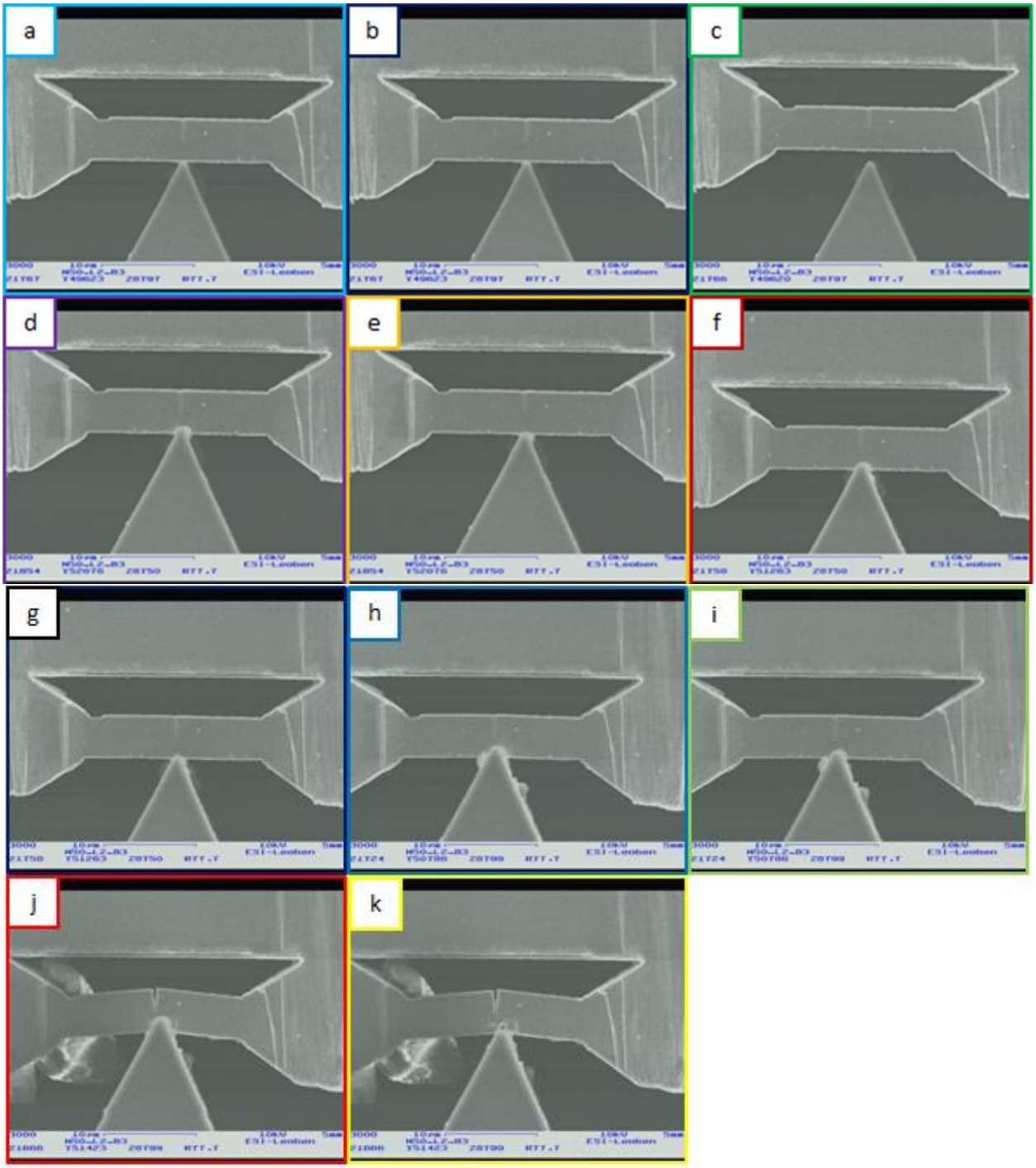

Figure 23: Selected frames from test video for 2500nm beam 1, taken from corresponding locations in the load-displacement data

4.1.2: $0.02s^{-1}$ Strain Rate

The deformation of 2500nm beam 2 was performed at a five times slower strain rate than the previous. Figure 24 shows the EBSD data gathered from the beam. One will notice that there is only an initial scan here, not one for each test as shown in other 2500nm beams. The beam was initially fabricated and scanned with EBSD to produce Fig. 24. It was then discovered that a remote part of the lamellae was partially obscuring the beam. This is not obvious from the EBSD due to the high tilt of 70° it was performed at. Last minute FIB work was done to remove the obscuring portion, but afterwards the EBSD signal was reduced greatly, below the threshold for proper identification. It is likely that redeposition of material from the FIB is to blame.

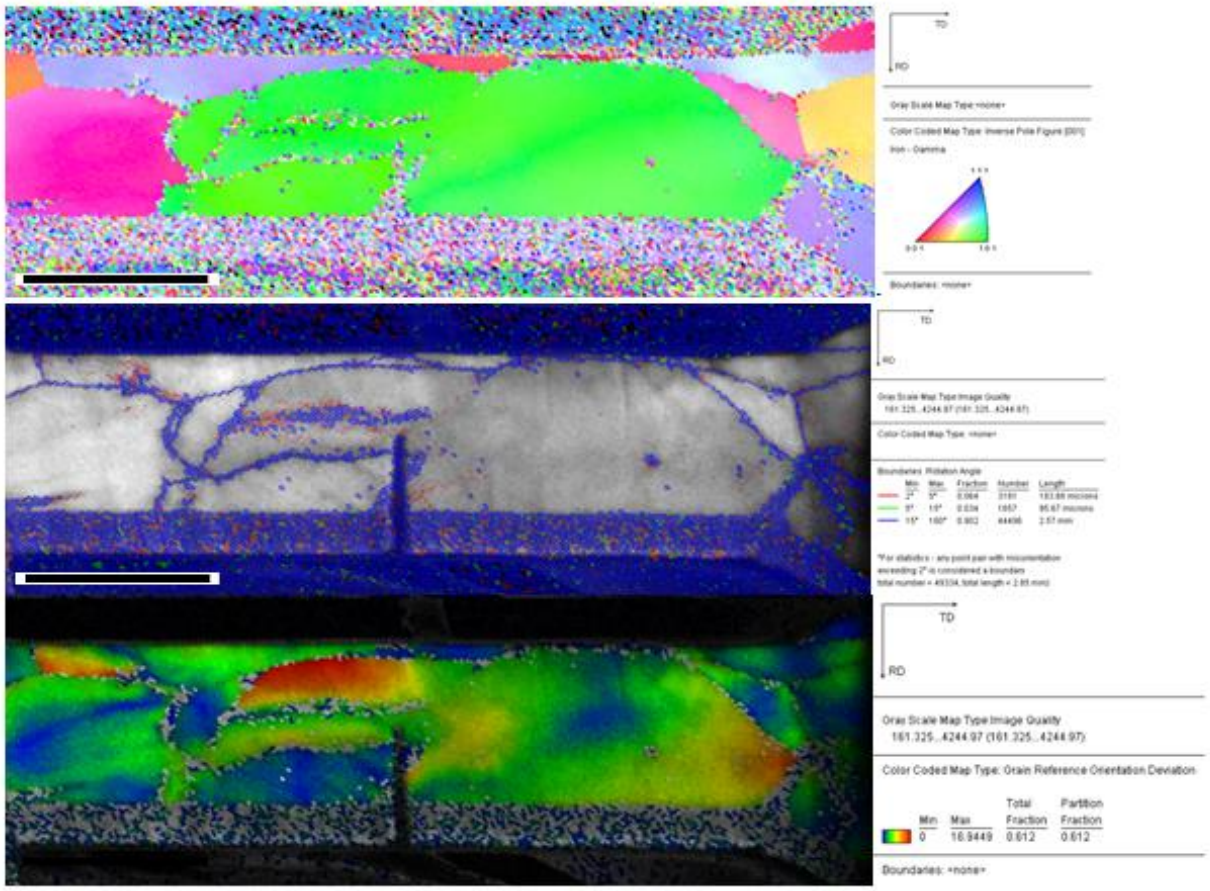

Figure 24: IPF map, IQ map with boundaries, and local misorientation relative to grain average map for 2500nm beam 2, scale bar 5µm

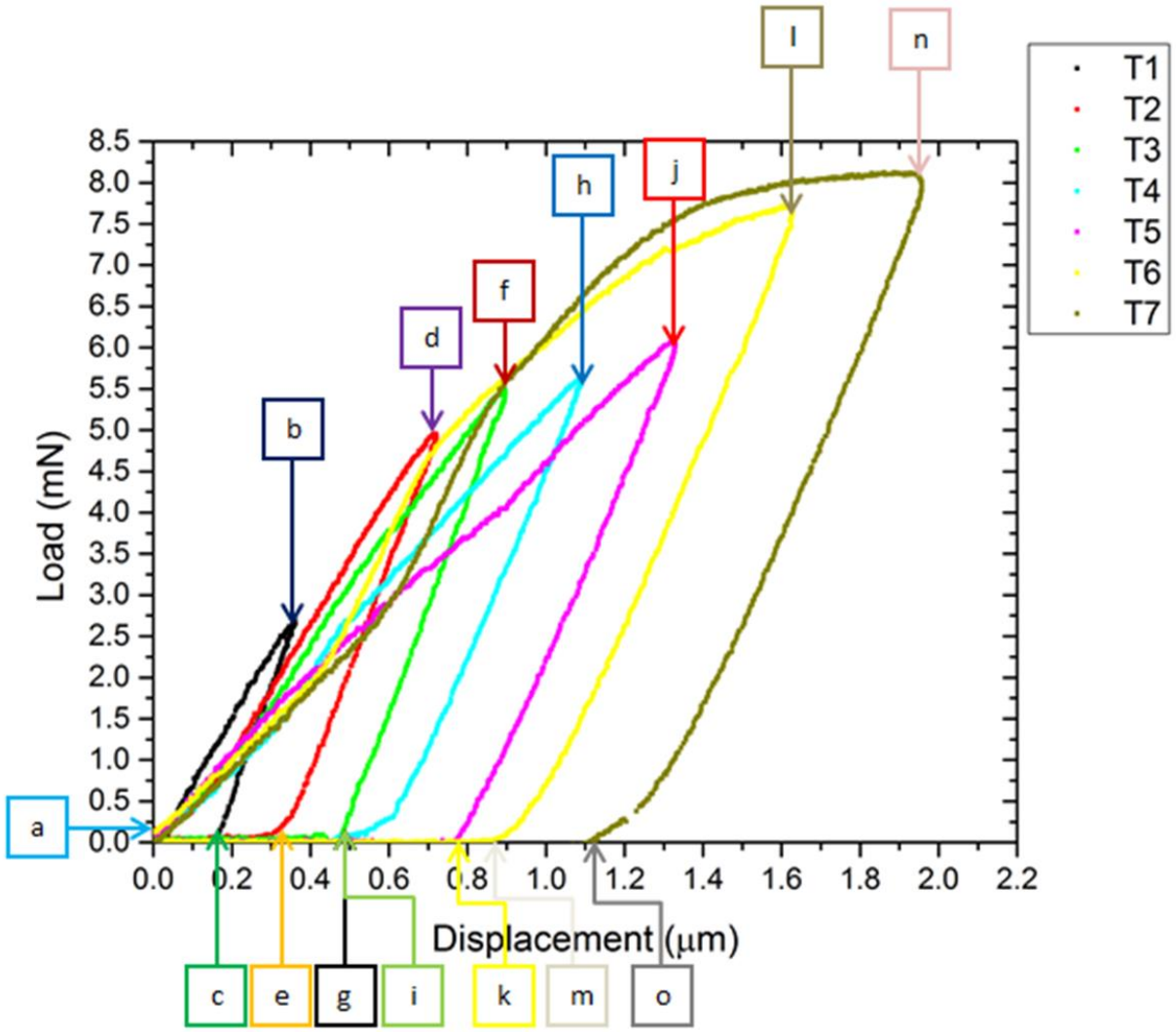

Figure 25: Load-displacement curve for 2500nm beam 2, with letters designating locations of screenshots from the corresponding video

Figure 25 shows the load-displacement data for this beam. As this was not scanned with the EBSD, it was decided to do smaller changes in displacement between the different tests, instead. It can be seen that the data is qualitatively quite similar to Fig. 22, though the force magnitude is much greater. This can be attributed to the larger thickness of the beam compared to the first beam presented; the beam in Fig. 25 is the proper 2500nm, while the first beam is roughly 1500nm, due to mis-cutting caused by drift. It can be seen that the load curls over into the plastic regime in the last test.

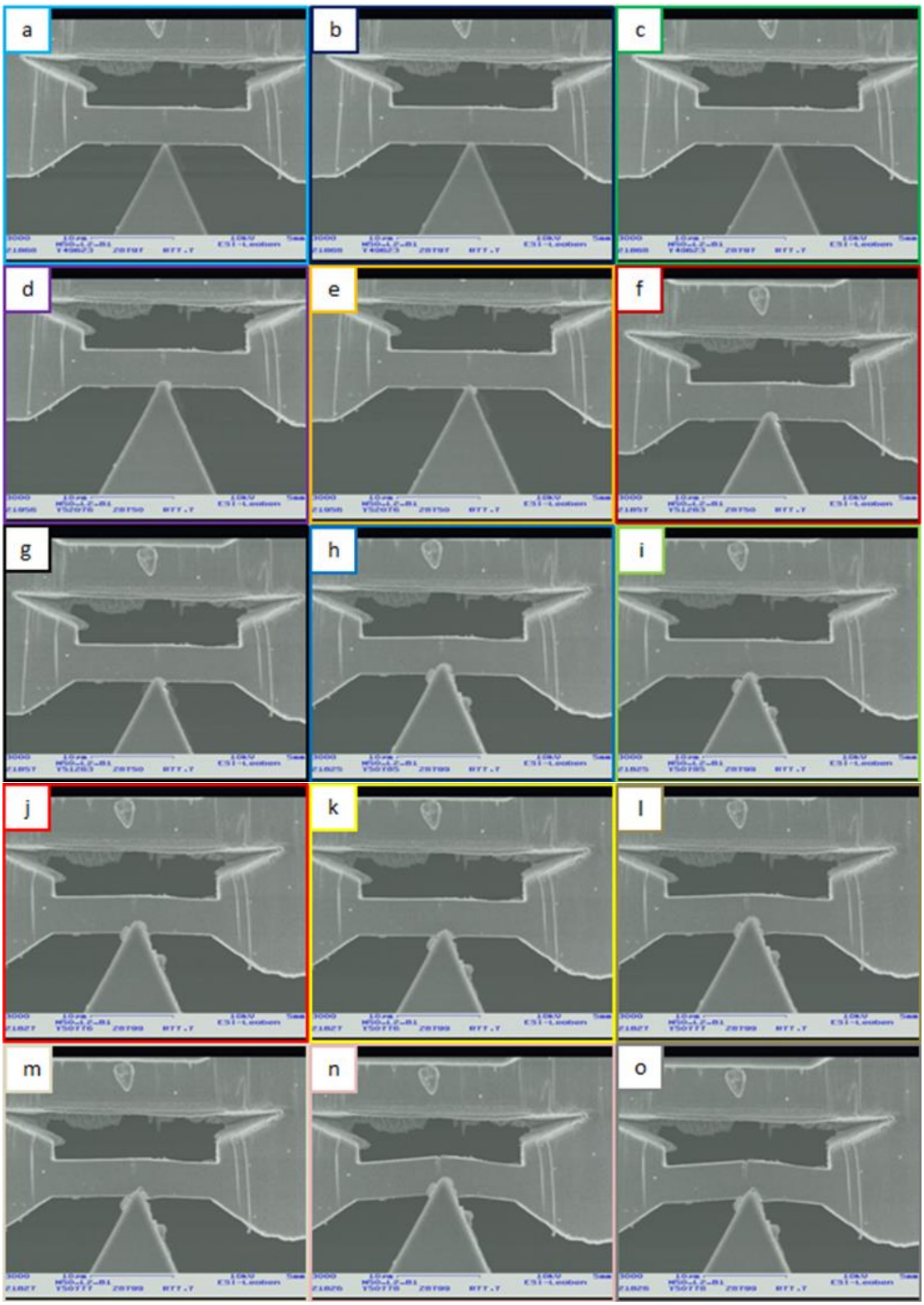

Figure 26: Selected frames from test video for 2500nm beam 2, taken from corresponding locations in the load-displacement data

Figure 26 shows the frames from the test video for 2500nm beam 2. The same qualitative behavior as in the previous test is observed, with highly plastic deformation. The crack starts opening in the last test as the load-displacement curve curls over into the plastic regime.

4.1.3: $0.01s^{-1}$ Strain Rate

For 2500nm beam 3, the strain rate was further decreased by a factor of two compared to the previous test. Fig. 27 shows the IPF map, where it can be seen that this beam was strongly affected by contamination buildup during testing, as signal is progressively lost from regions of the beam. Not much orientation change can be seen in Fig. 27.

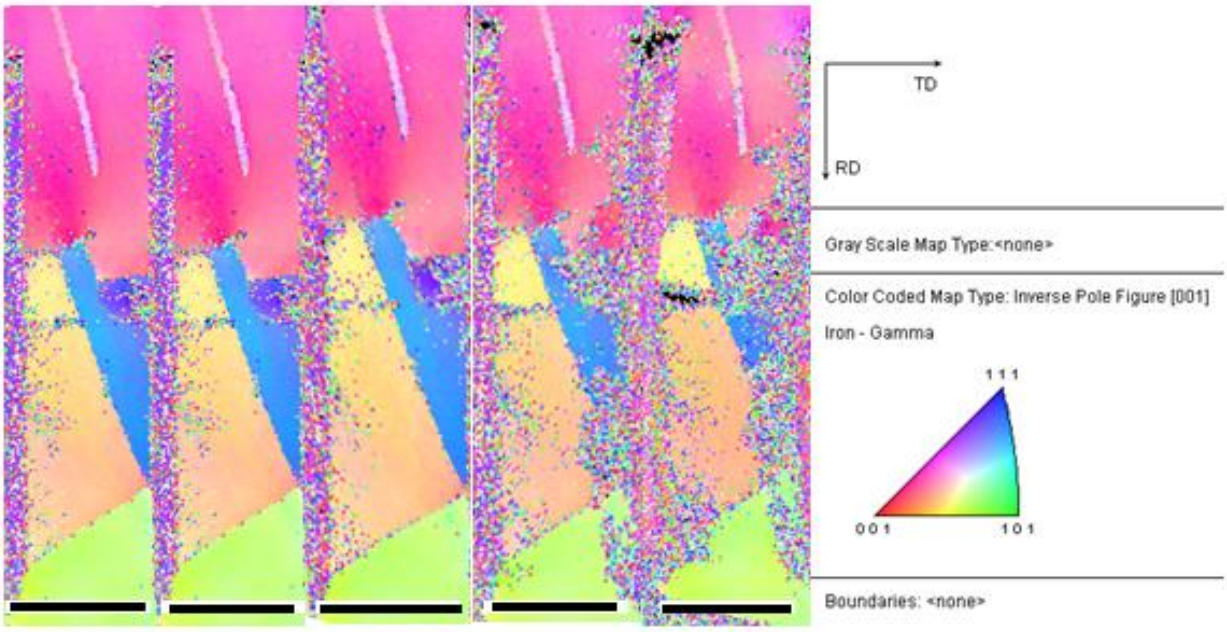

Figure 27: IPF Maps of 2500nm beam 3 after each testing cycle, scale bar 5μm

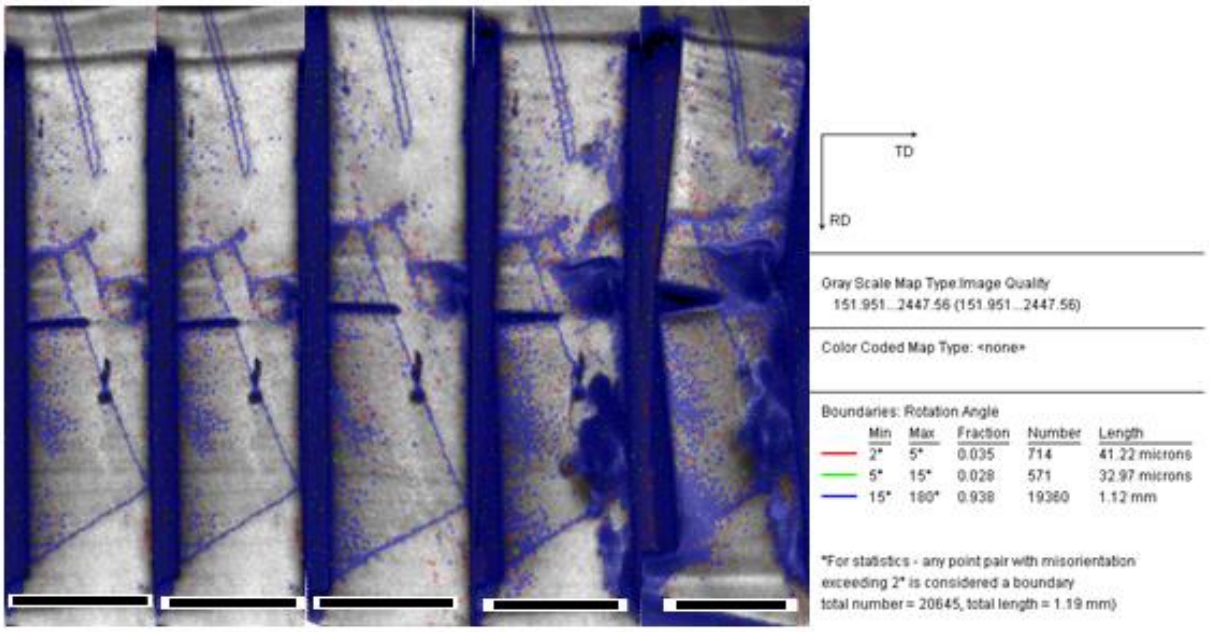

Figure 28: IQ Maps with highlighted boundaries of 2500nm beam 3 after each testing cycle, scale bar 5μm

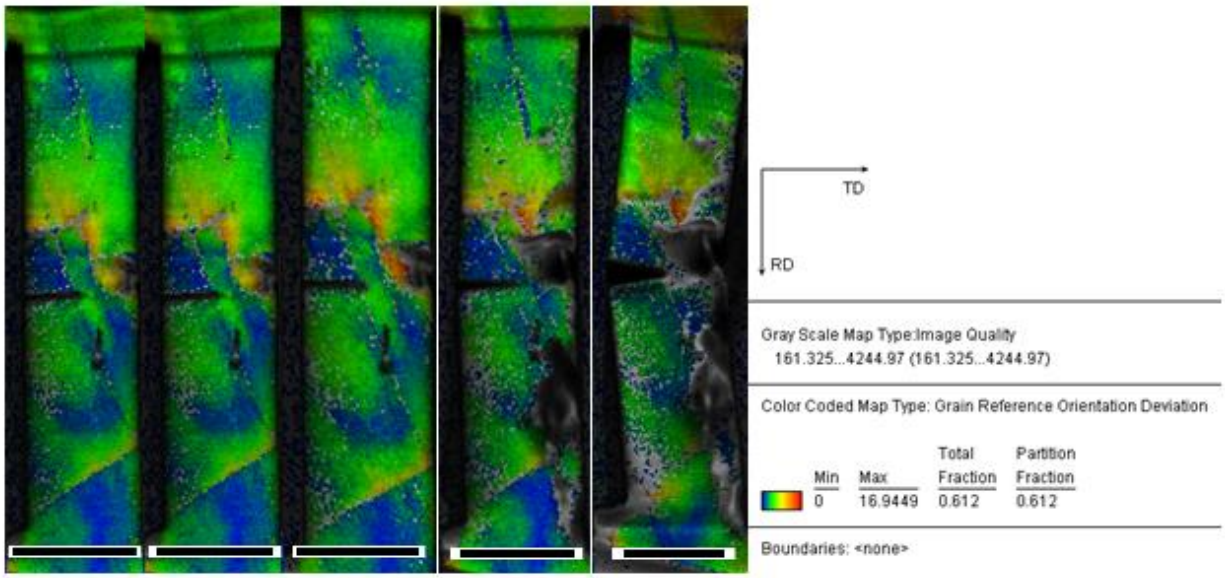

Figure 29: Local misorientation relative to the grain average for 2500nm beam 3 after each testing cycle

As before, Fig. 28 shows the IQ map with grain boundaries marked. It can be seen that the crack is intersecting a grain boundary running through the center of the beam. Fig. 29 shows the local misorientation, which undergoes smaller changes as testing progresses compared to 2500nm beam 1, but the reorienting grains may be lost with the data obscured by contamination.

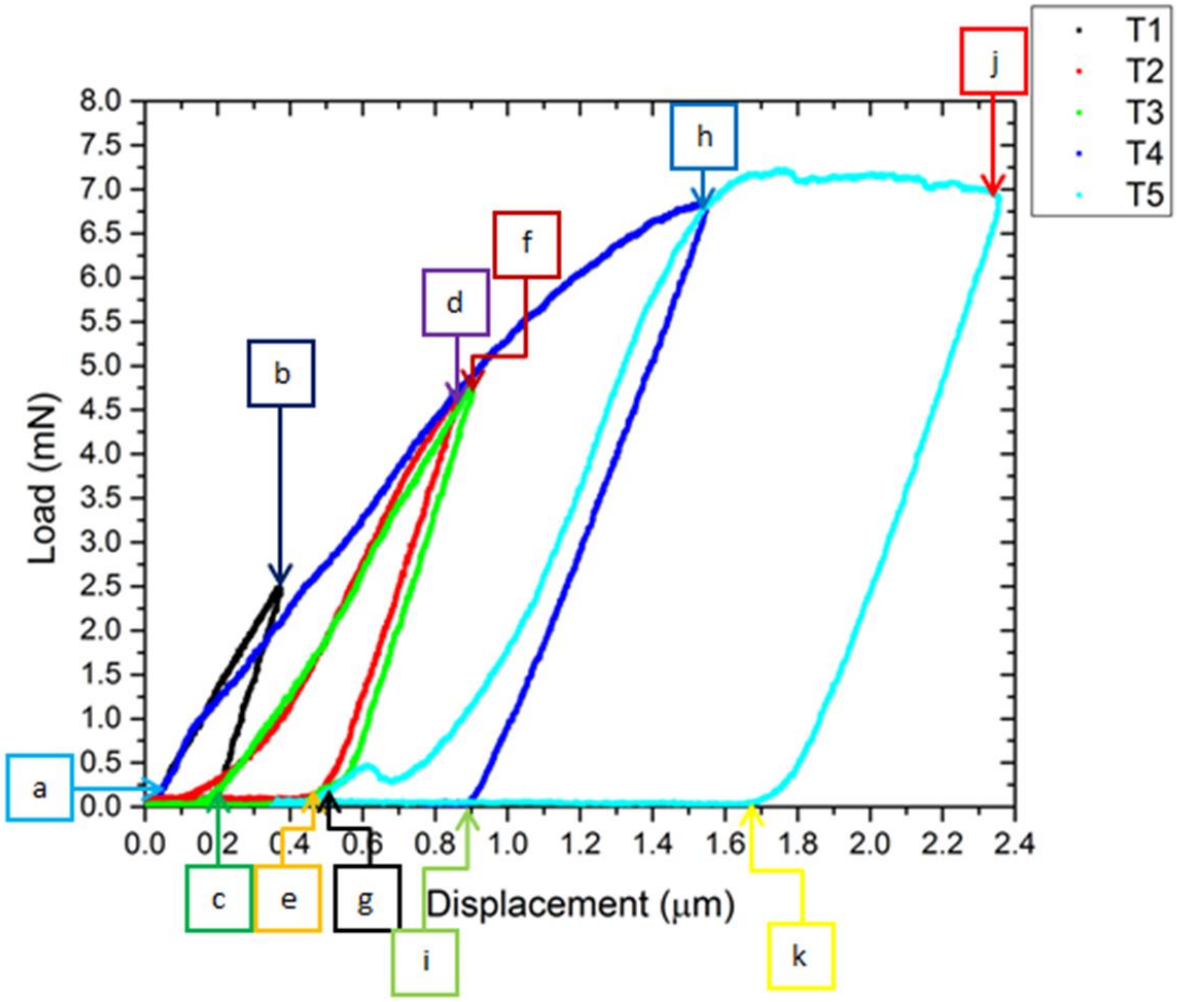

Figure 30: Load-displacement curve for 2500nm beam 3, with letters designating locations of screenshots from the corresponding video

Figure 30 shows the load-displacement data for 2500nm beam 3. It can be seen that the behavior is similar to the previous tests, with the load curling over during the last test cycle. This corresponds to the crack opening strongly, as shown in the corresponding video stills presented in Fig. 31. During the flattened portion, distinctive bumps can be seen in Fig. 30, which may correspond to formation of slip steps. The explanation is that plasticity occurs in discrete bursts of dislocations that move too rapidly for the indenter system to track. The feeback system then overcompensates and has to back out again, resulting in bumps in the load-displacement data.

One should note that the last two frames of Fig. 31 are at a different magnification that the rest; this is due to operator error, but enhance the opening of the crack.

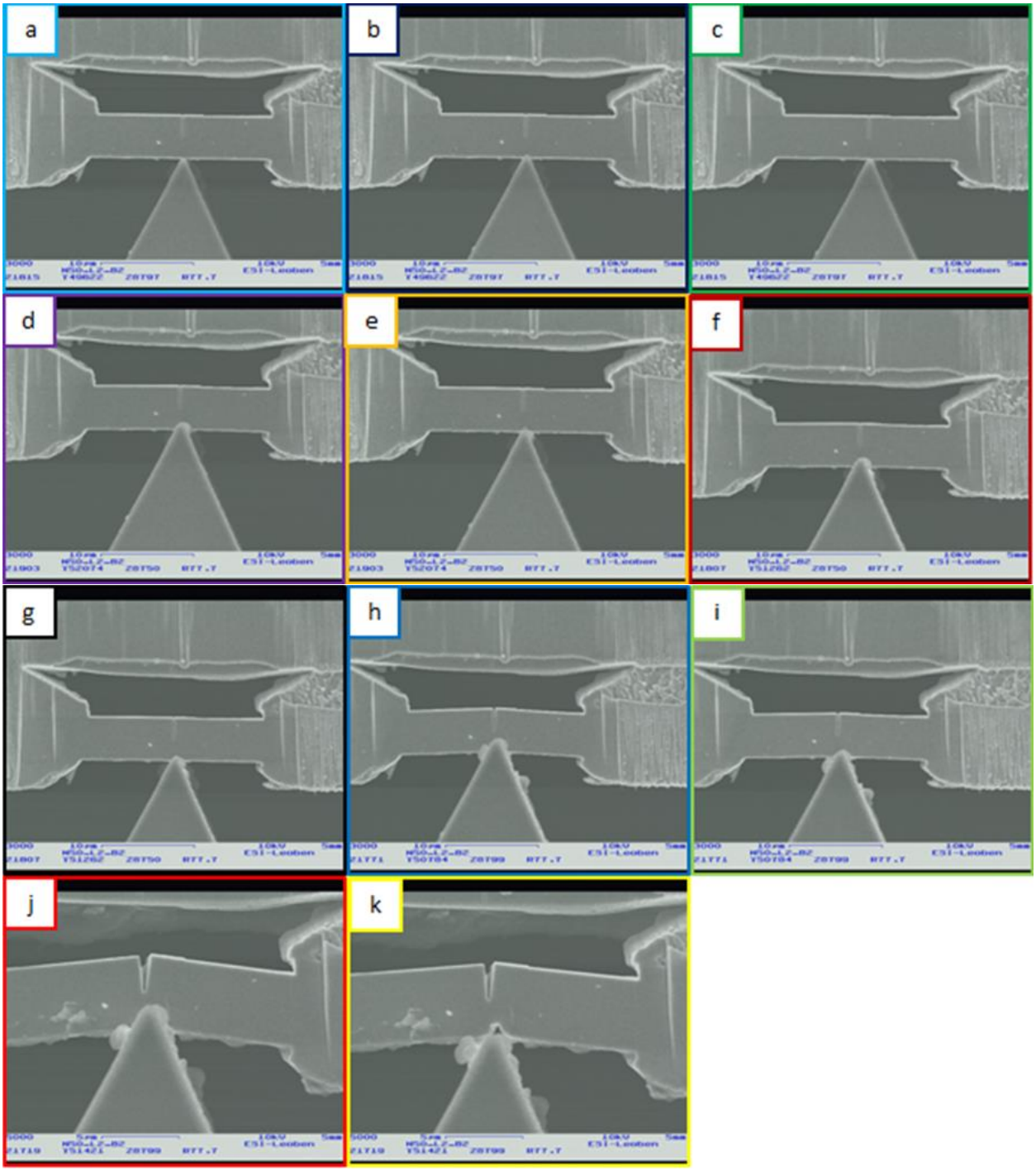

Figure 31: Selected frames from test video for 2500nm beam 3, taken from corresponding locations in the load-displacement data

4.1.4: $0.004s^{-1}$ Strain Rate

2500nm beam 4 was tested at one fourth the strain rate of 2500nm beam 3. The IPF maps are shown in Fig. 32. It can be seen that the crack and impression both lie within the same large grain that makes up most of the beam. Fig. 33 shows the IQ maps with boundaries Fig 34 shows the local misorientation. In Fig. 32-34, no large changes can be seen in the as deformation commences.

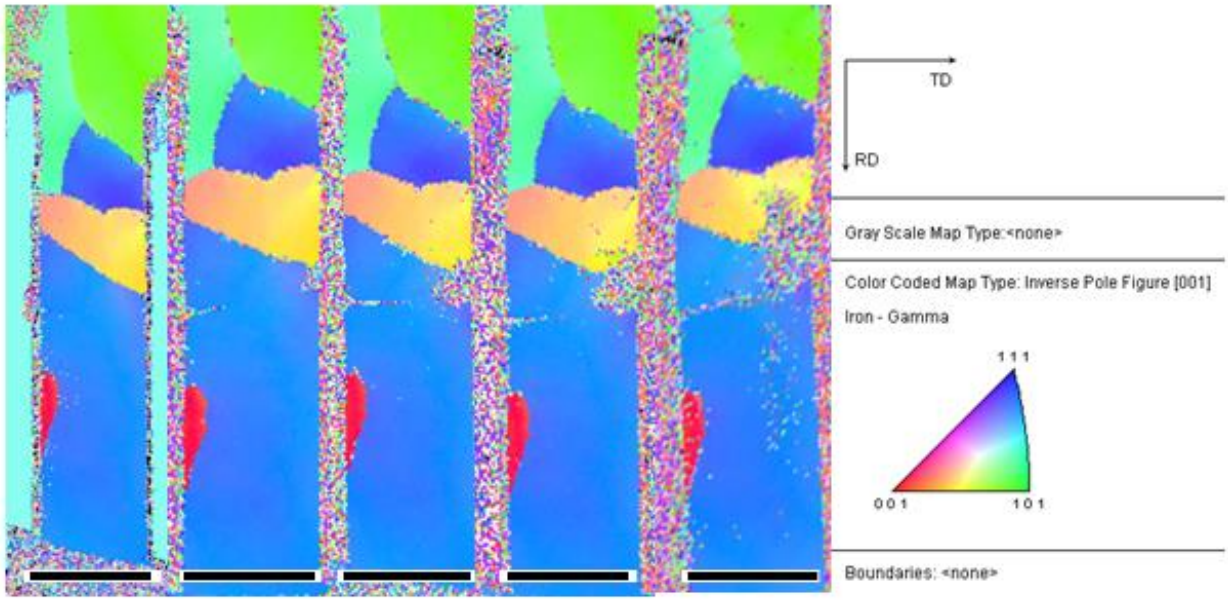

Figure 32: IPF Maps of 2500nm beam 4 after each testing cycle, scale bar 5µm

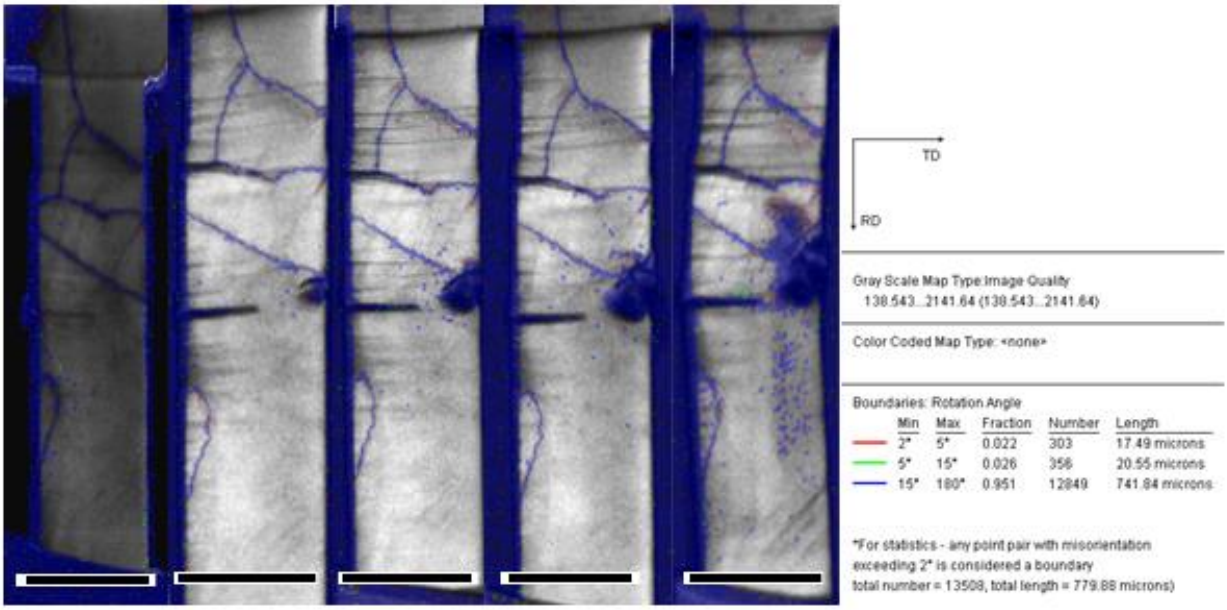

Figure 33: IQ Maps with highlighted boundaries of 2500nm beam 4 after each testing cycle, scale bar 5μm

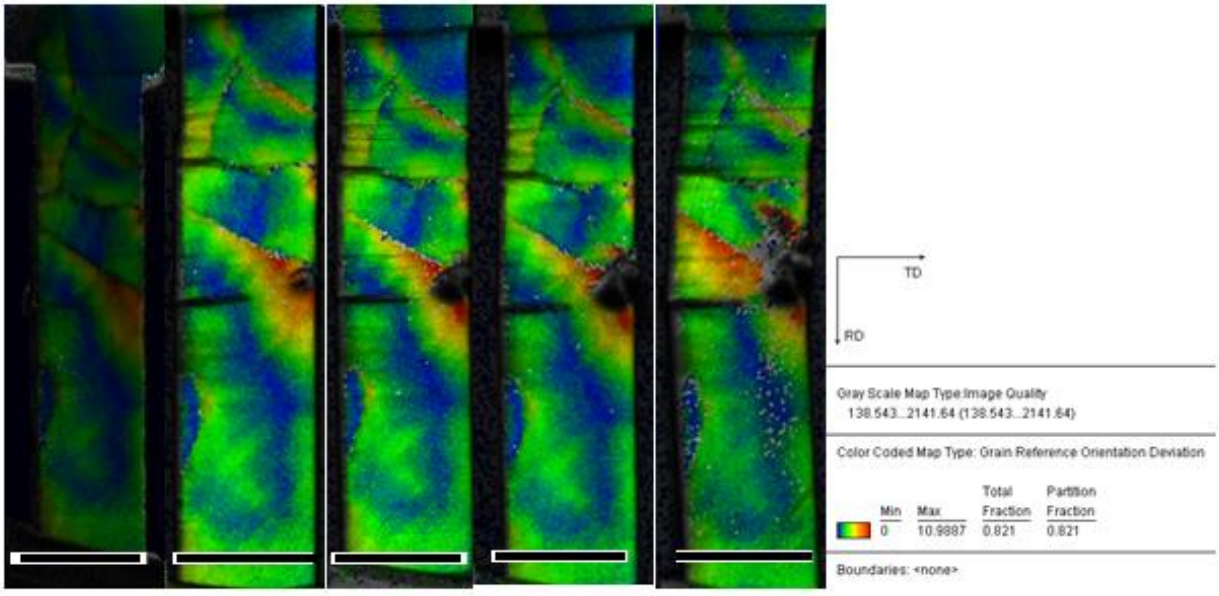

Figure 34: Local misorientation relative to the grain average for 2500nm beam 4 after each testing cycle

Fig. 35 shows the load-displacement data for 2500nm beam 4. Unfortunately, another miss-cutting error occurred here due to drift and the beam is similarly too thin, ~1500nm. This is reflected in the lower values of the load compared to the previous test. Much less total displacement is used in this test before the load curls over into the plastic regime, but no strong

indicators of plasticity are shown in the EBSD data. Fig. 36 shows the corresponding stills from the video for 2500nm beam 4 shows typical behavior compared to the rest of the beams, with the crack opening in coincidence with the curling over of the load. The slow strain rate may have had some effect as to why there are no strong indications of plasticity in the EBSD.

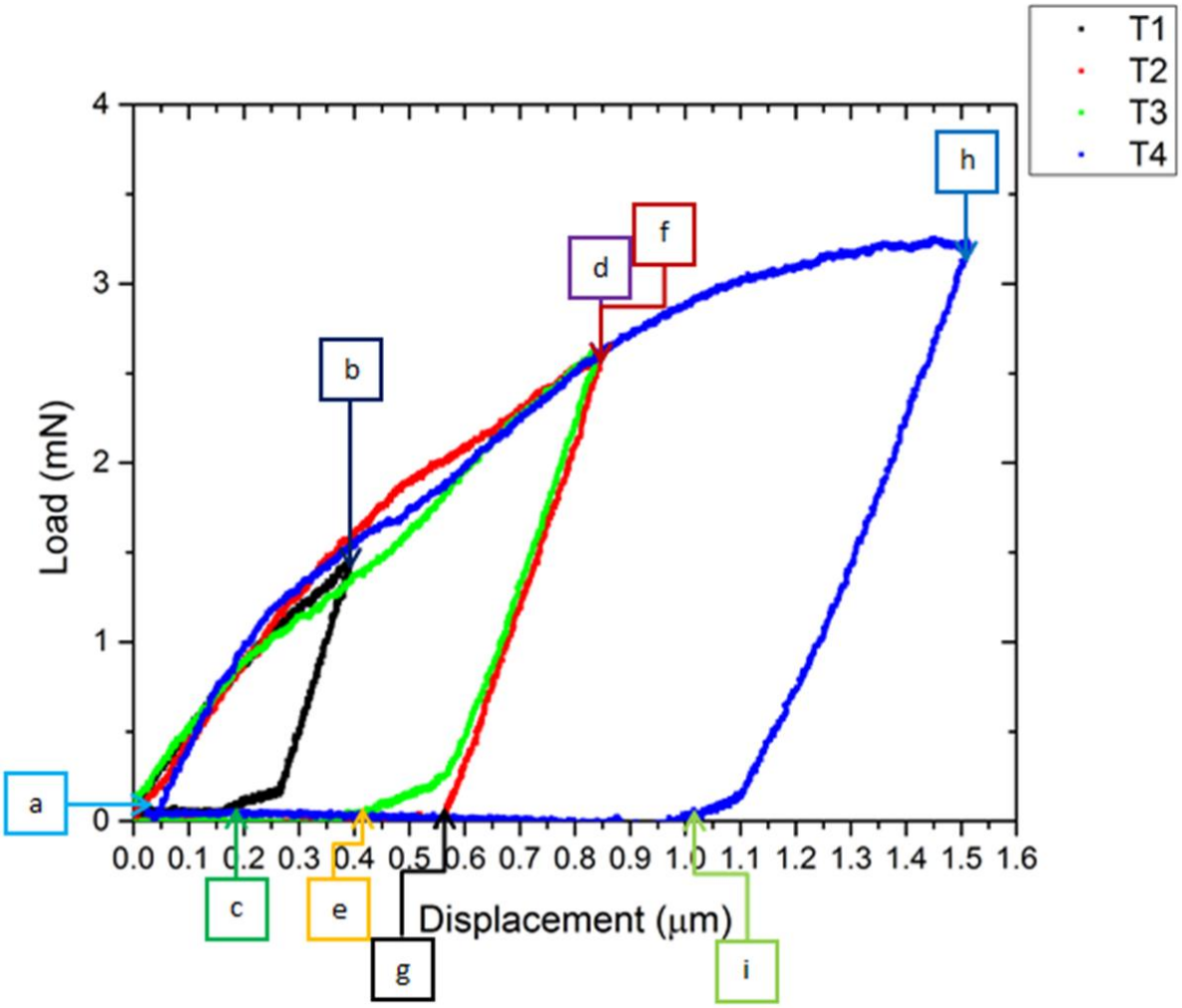

Figure 35: Load-displacement curve for 2500nm beam 4, with letters designating locations of screenshots from the corresponding vide

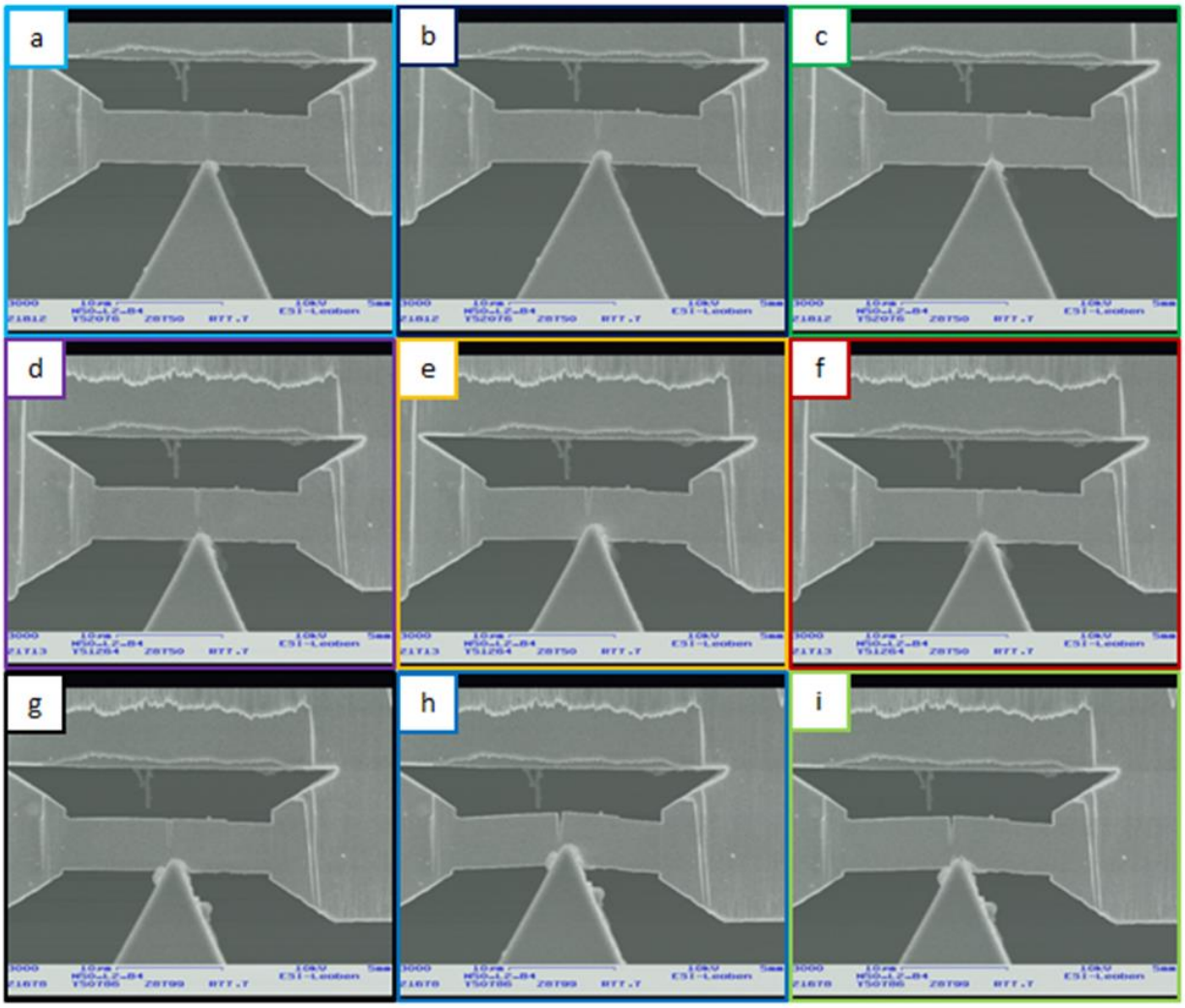

Figure 36: Selected frames from test video for 2500nm beam 4, taken from corresponding locations in the load-displacement data

4.1.5: Post-mortem imaging of 2500nm beams

High resolution SEM imaging was performed post mortem on these specimens, using an accelerating voltage of 10keV. Evidence of local slip bands near expected stress concentration sites was found and is presented in Fig. 37. In particular, slip occurred heavily around the crack root, the residual impression of the indenter, and at the clamped corner on the un-notched edge.

Fig. 37d exemplifies the difficulty in precise reloading of the beam when the sample had to switch instruments after each test for the EBSD.

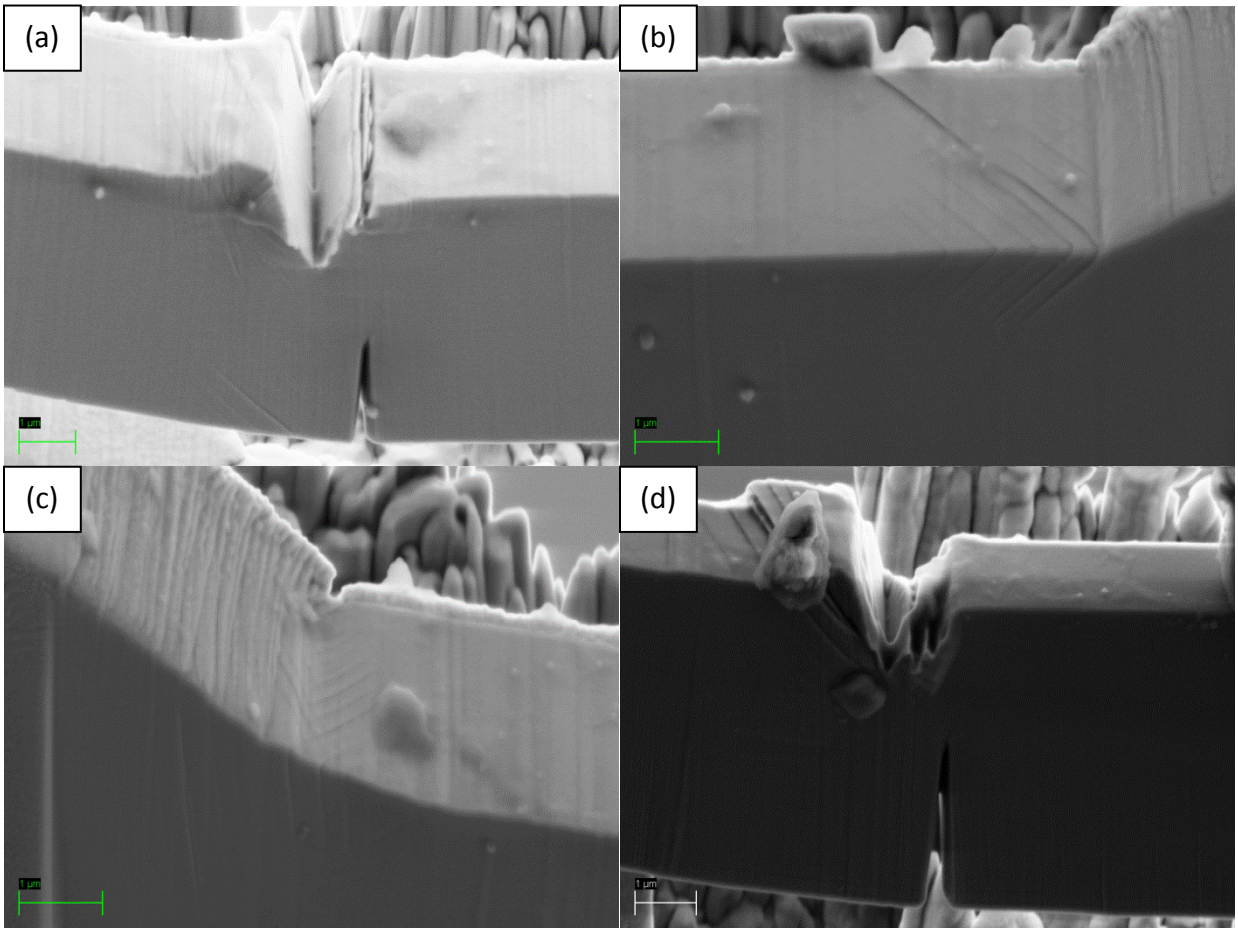

Figure 37: Post-mortem SEM imaging of various 2500nm beams, showing slip band plasticity

4.2: 500nm Beams

The greatly reduced volume of the 500nm beams means that the measured loads were fairly close to the error limit of the system and as such, the data was much more susceptible to events such as drift. Since the test specimens were much smaller, more could be fit onto the same lamellae, such that two beams were tested at each strain rate utilized for the 2500nm beams. It can be seen as strain rate is decreased, increasing artifacts are introduced into the data as a result of drift. As previously stated, EBSD data could not be collected from individual

beams as was possible with the 2500nm beams. Instead, an EBSD scan of the entire lamellae the beams were fabricated on is presented in Fig. 38, with markings to show the spacing of the beams as a visual aid. The horizontal line shows the approximate line of the neutral axis for the fabricated beams.

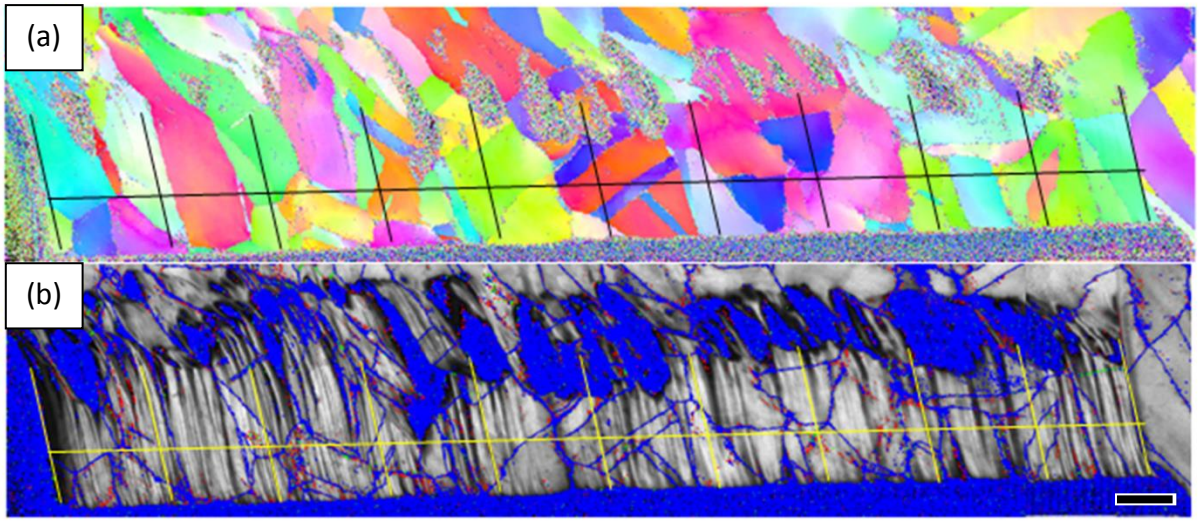

Figure 38: a) IPF Map and b) IQ Map with boundaries for the entire lamellae which the 500nm beams were fabricated on. Lines show the approximate locations of the beams made, scale bar 5um

4.2.1: $0.1s^{-1}$ Strain Rate

500nm beams 1&2 were tested at the highest strain rate of $0.1s^{-1}$. The load-displacement data for 500nm beam 1 is shown in Fig. 39 and the corresponding stills from the video in Fig. 40. It can be seen that beams underwent significant plastic deformation as the load displacement data curls over rapidly and shows load drops characteristic of plastic deformation. The crack continues to open further as the test proceeds and does not establish a stable crack front. The crack can be observed to grow through an apparent tearing mode which is also characteristic of highly ductile behavior.

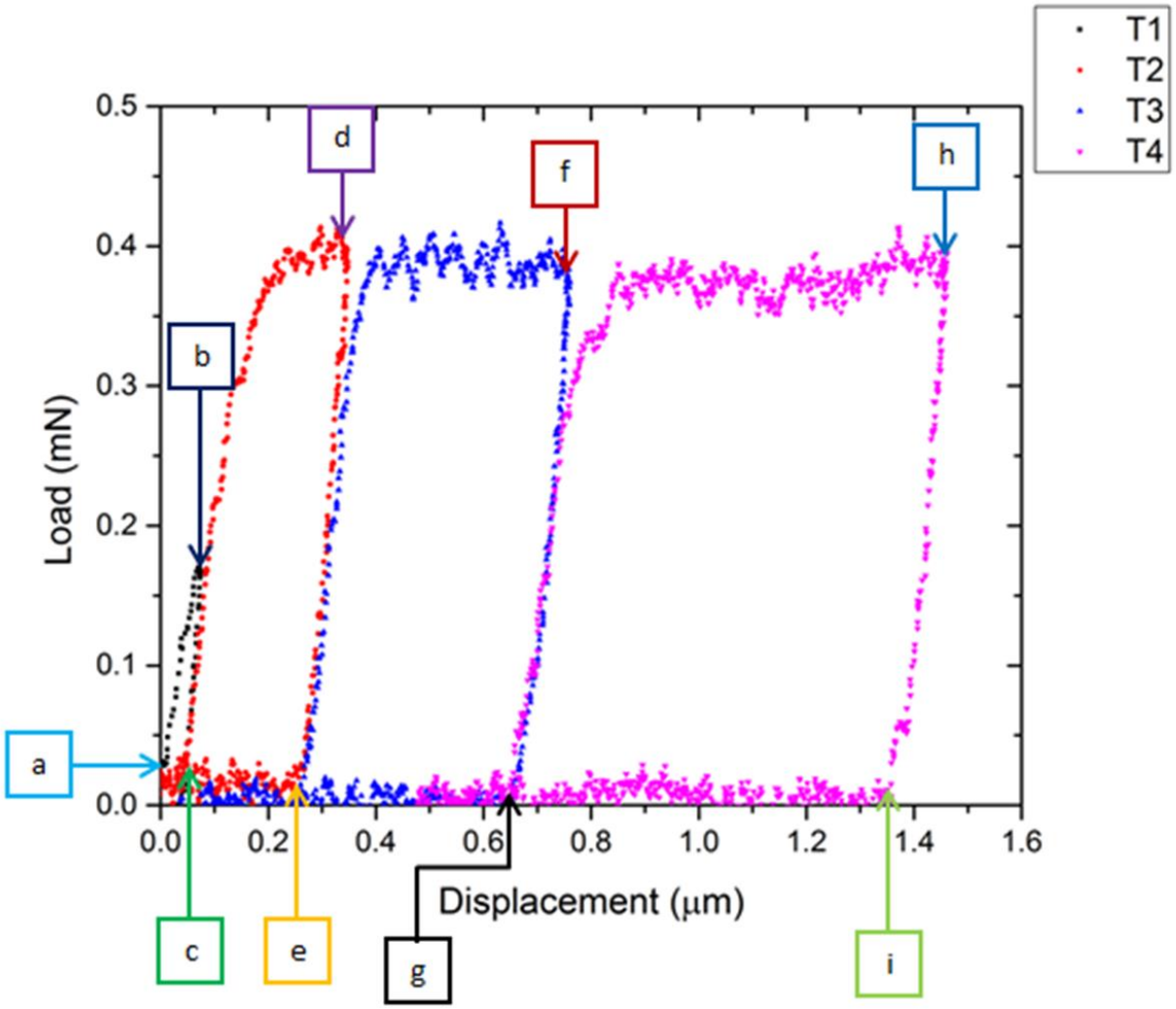

Figure 39: Load-displacement curve for 500nm beam 1, with letters designating locations of screenshots from the corresponding video

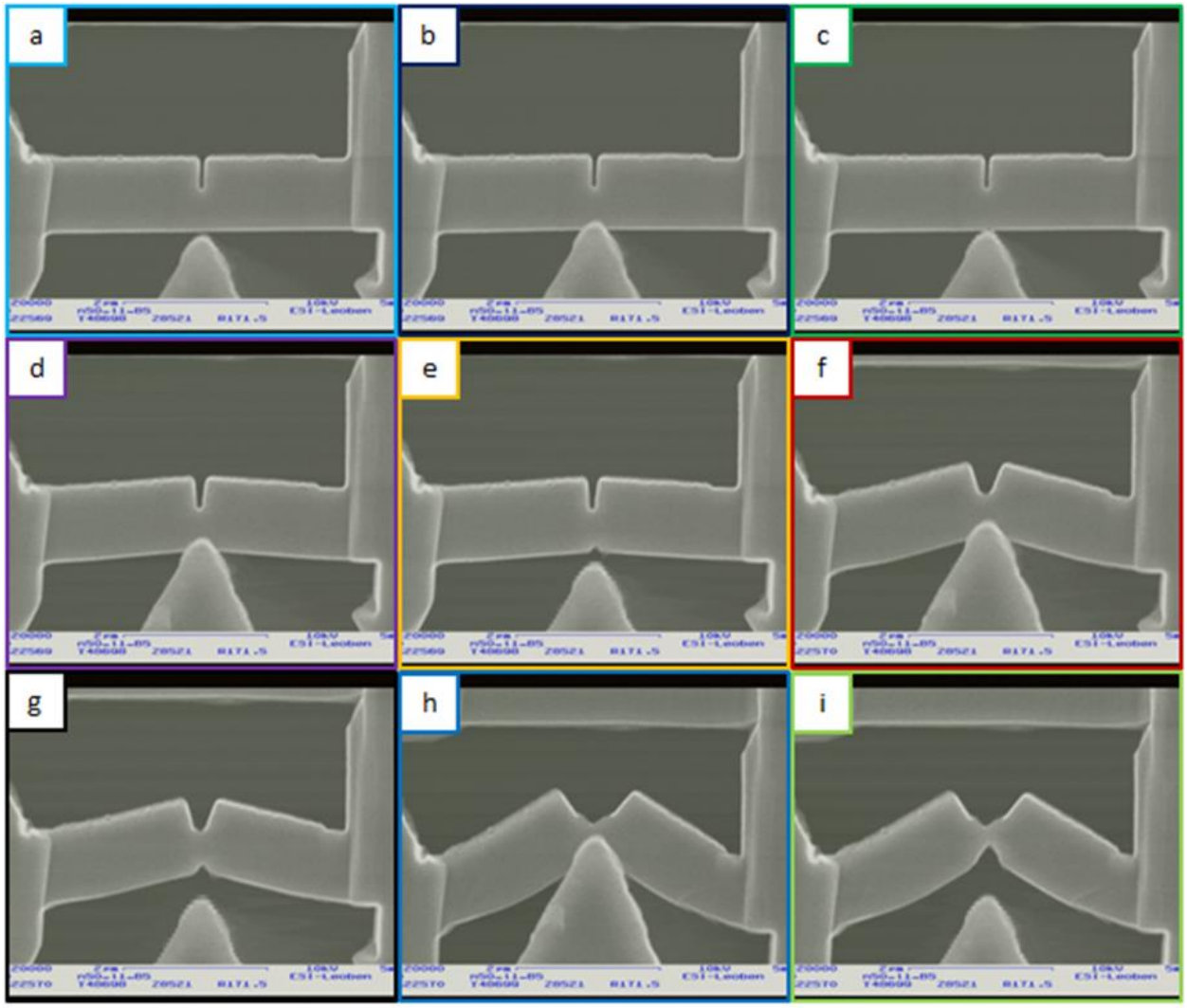

Figure 40: Selected frames from test video for 500nm beam 1, taken from corresponding locations in the load-displacement data

Figure 41 shows the load-displacement data for 500nm beam 2, and Fig. 42 shows the corresponding stills from the test video. The behavior is similar to the beam previously presented, although a finite degree of hardening can be observed in this beam. This may be due to the increased number of grain boundaries present in this beam, which can be confirmed by studying the EBSD data presented in Fig. 38. This would also explain the slightly higher load levels achieved by this beam as compared to 500nm beam 1. The SEM screenshots show nearly identical behavior to the first beam.

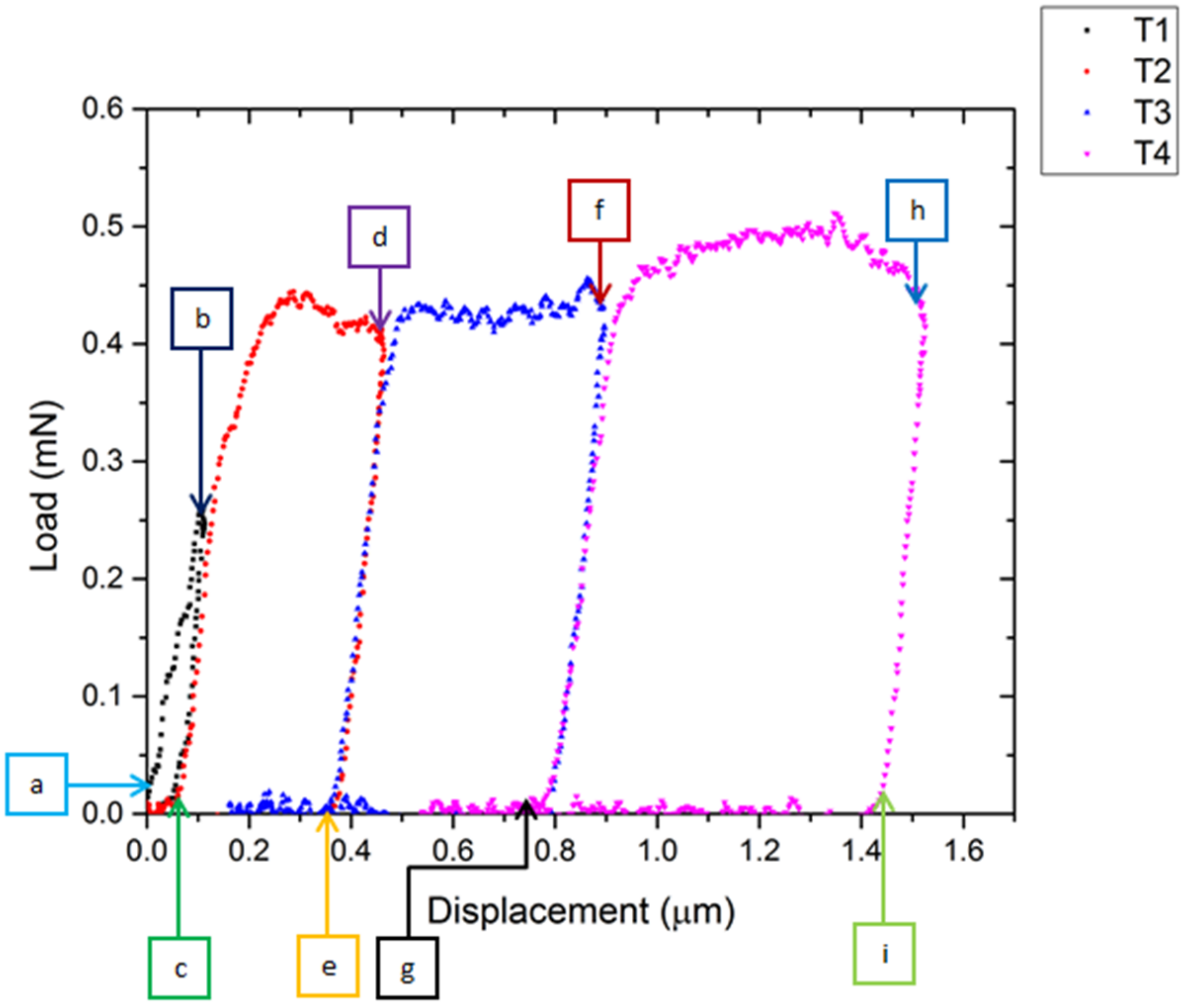

Figure 41: Load-displacement curve for 500nm beam 2, with letters designating locations of screenshots from the corresponding video

It can be observed in Fig. 41 that the load starts to decrease near the end of the last cycle. This is not necessarily unexpected, as the cross-section is constantly being reduced as the indenter pushes its impression into the beam. Another interesting feature of this test that can be observed from Fig. 42 is a small bridge of material that goes across the crack near the outer fiber. As the crack tears open, this ligament is eventually severed. This probably arose due to a slight mis-cutting of the pre-notch with the FIB. It can be seen that the crack does not achieve a stable opening displacement, as in the previous tests and continually tears open further.

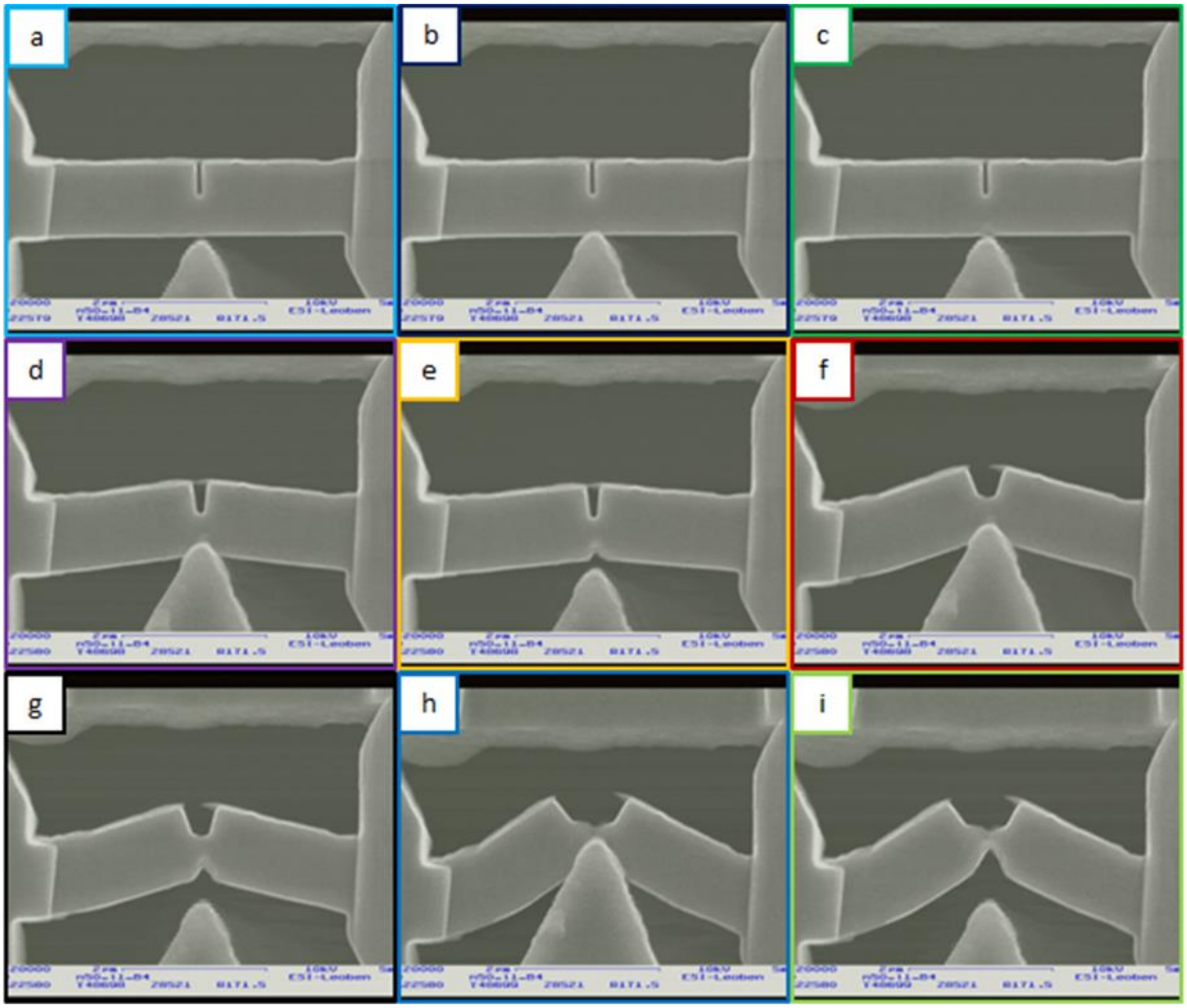

Figure 42: Selected frames from test video for 500nm beam 2, taken from corresponding locations in the load-displacement data

4.2.2: $0.02s^{-1}$ Strain Rate

500nm beams 3&4 were tested at a strain rate 5 times lower than 500nm beams 1&2. The load-displacement curve of the first of these beams is shown in Fig. 43 and the corresponding stills from the test video in Fig. 44. The results are similar to the faster strain rate; however the onset of the curl over into the plastic regime is less sharp when compared to the higher strain rate beam. This beam also sustained slightly higher loads when compared to the

faster strain rates. The last test cycle shows a drastic decrease in load as the beam completely tears apart, which can be seen in the last frames of Fig. 44.

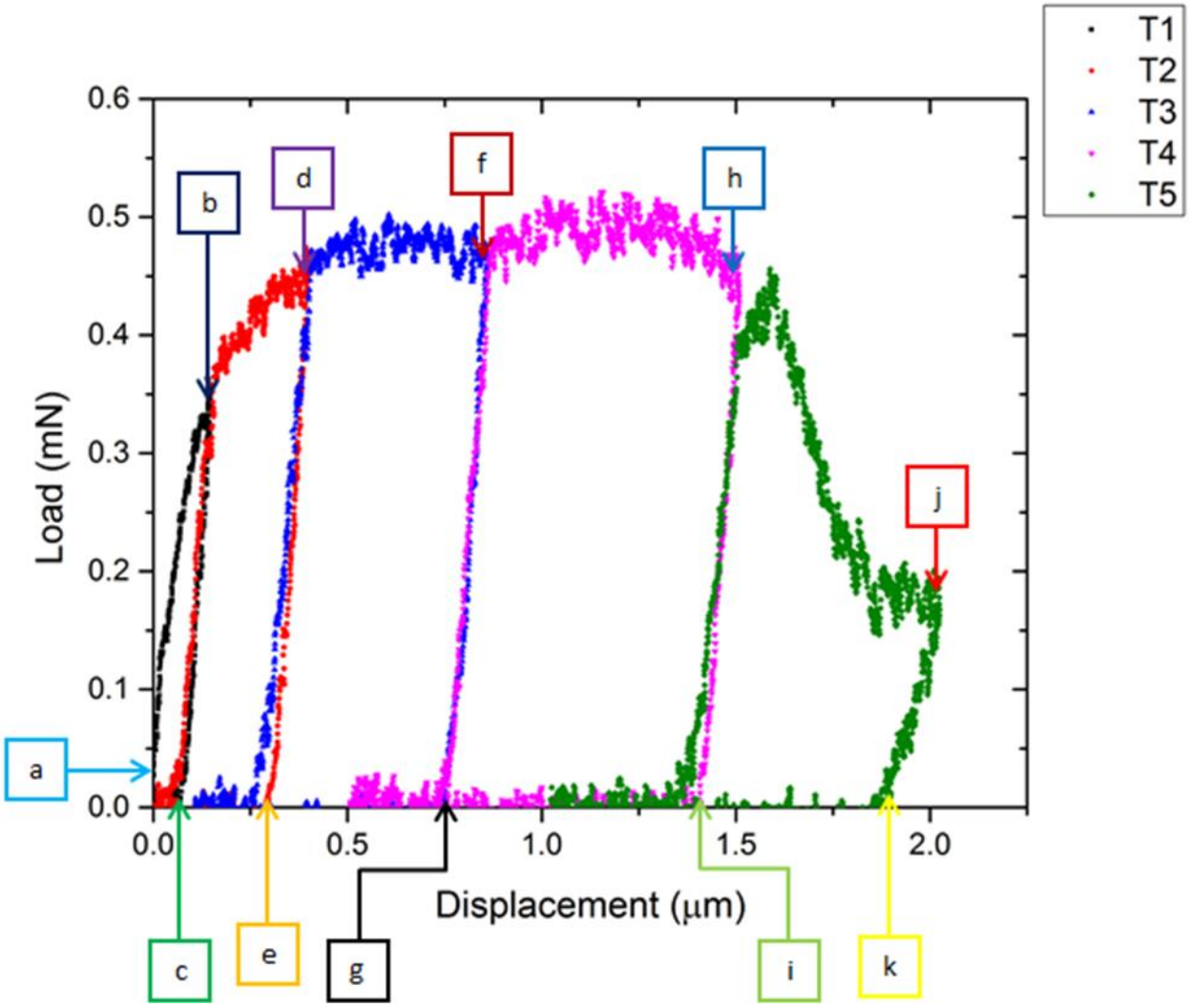

Figure 43: Load-displacement curve for 500nm beam 3, with letters designating locations of screenshots from the corresponding video

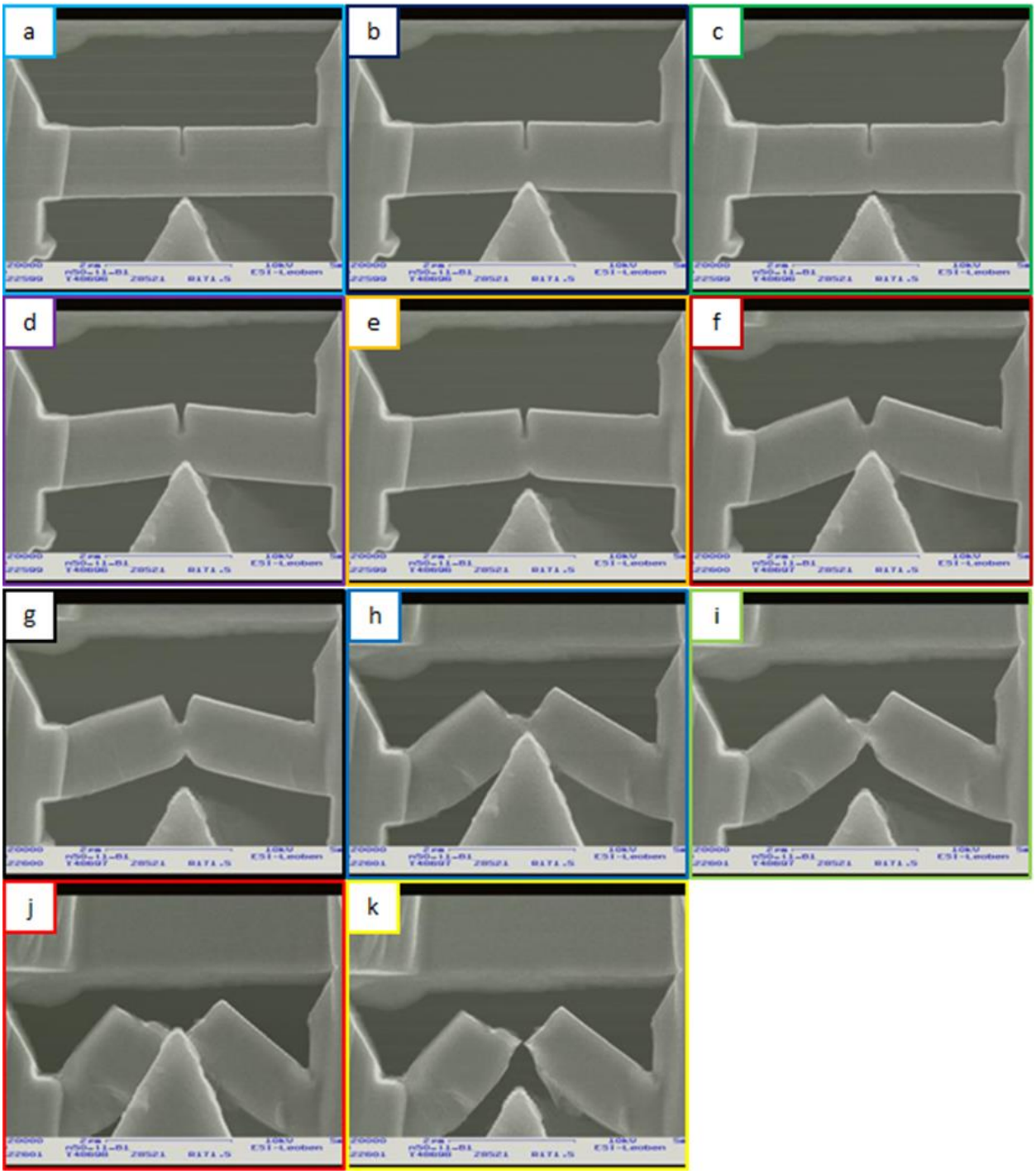

Figure 44: Selected frames from test video for 500nm beam 3, taken from corresponding locations in the load-displacement data

The load-displacement data for 500nm beam 4 tested is shown in Fig. 45 and the corresponding stills from the test video in Fig. 46. This beam also shows enhanced load levels compared to the faster strain rate, but also significant hardening in the third and fourth tests.

When the EBSD data in Fig. 36 is studied, one can see that the region this beam was fabricated in also has a high density of grain boundaries, similar to beam two at the highest strain rate. This suggests that the presence of grain boundaries enhances strain hardening in these beams as expected.

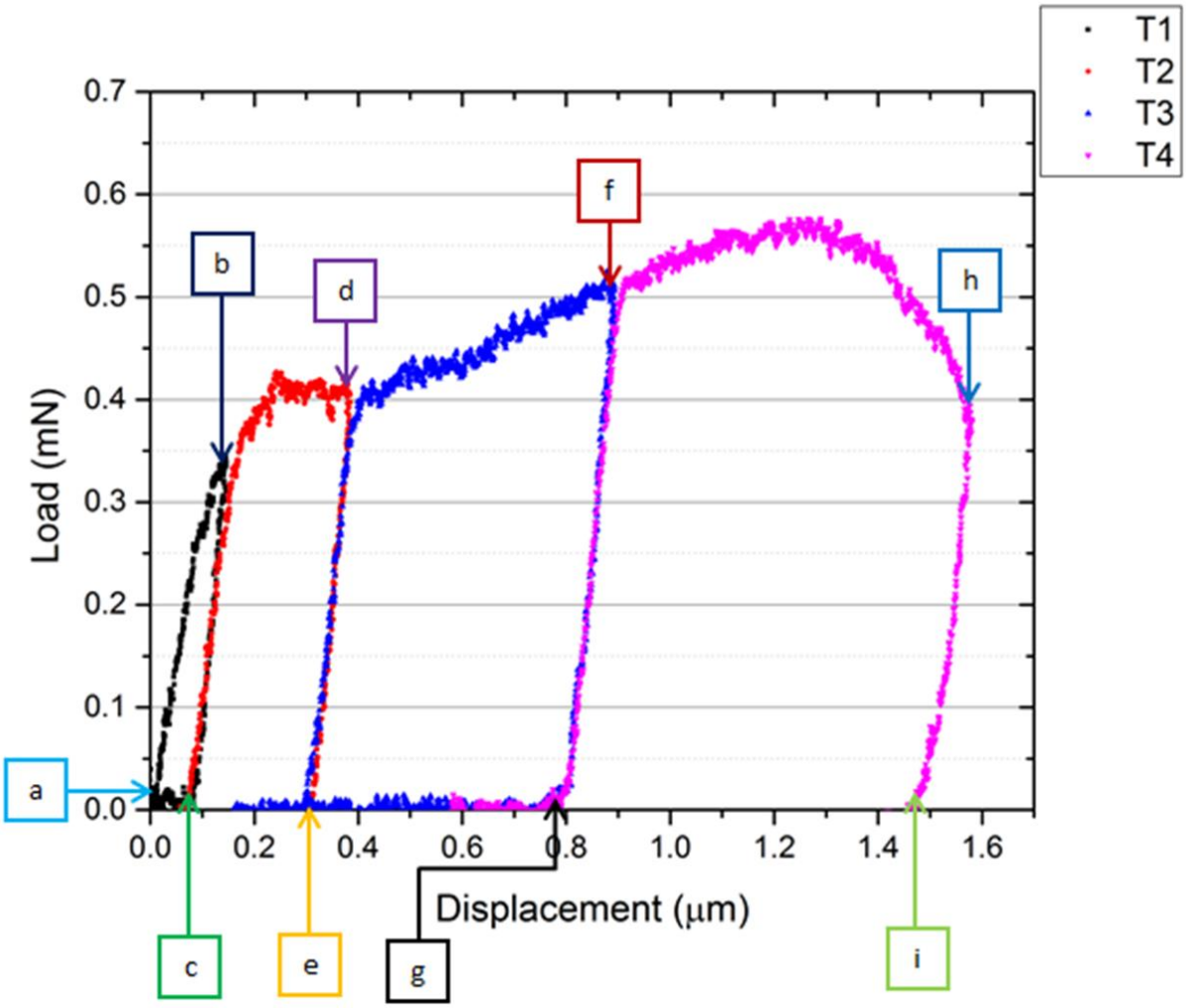

Figure 45: Load-displacement curve for 500nm beam 4, with letters designating locations of screenshots from the corresponding video

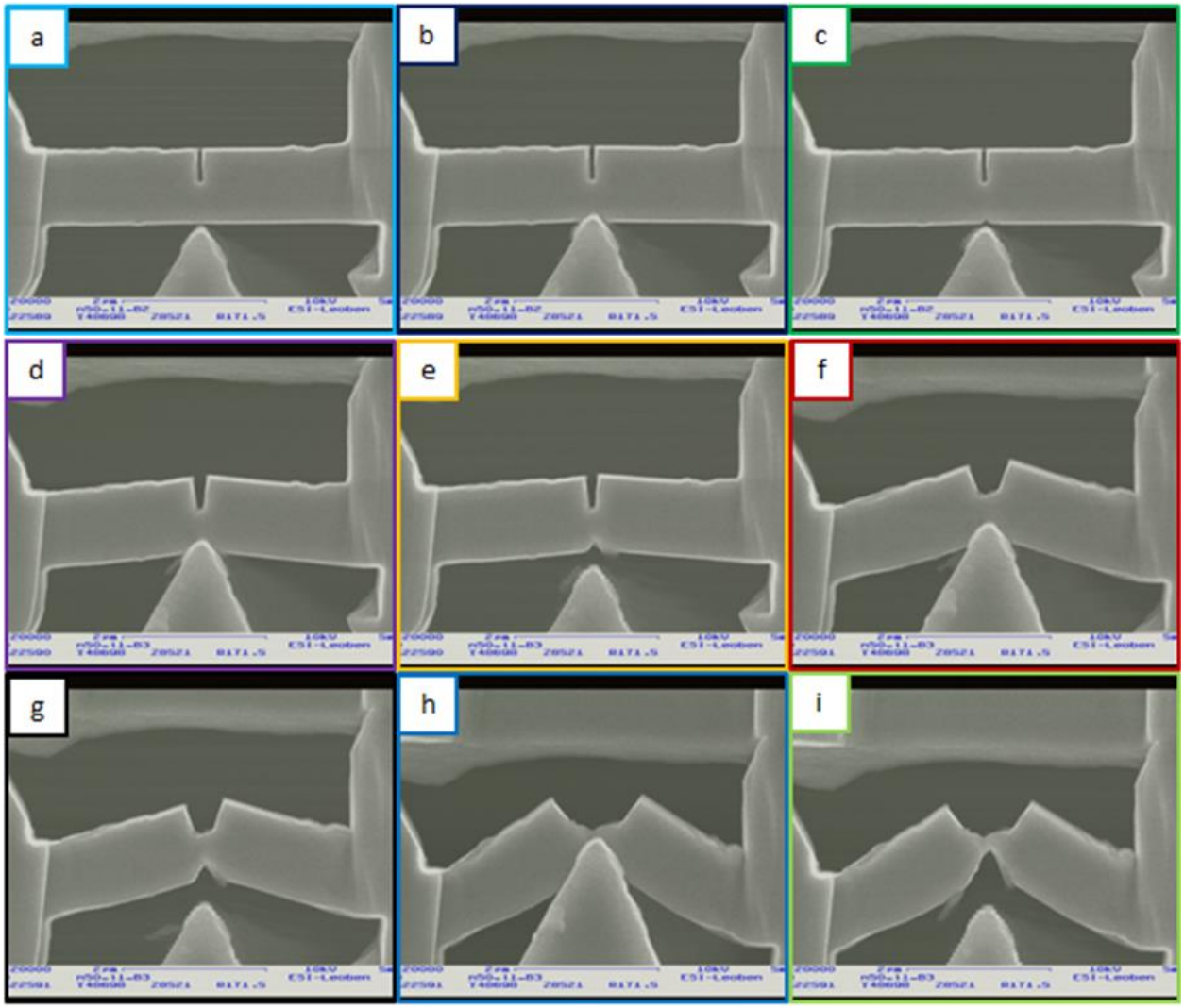

Figure 46: Selected frames from test video for 500nm beam 4, taken from corresponding locations in the load-displacement data

Figure 46 shows the same overall behavior as the other beams previously presented. It is worth noting the particularly rough appearance of this beam due to uneven FIB milling. This also supports the idea that this beam is multi-grained. This is because some of the grain orientations will be more preferentially oriented towards the beam, allowing them to be removed more quickly than the less favorable orientations, giving rise to a rough surface of the bending beam. This should not have too significant of an effect on the test data since it is present in a region that is not primarily deforming due to a low stress concentration.

4.2.3: $0.01s^{-1}$ Strain Rate

500nm beams 5&6 were tested at a strain rate one half that of 500nm beams 3&4. The load-displacement data for 500nm beam 5 is presented in Fig. 47 and the corresponding stills from the test video in Fig. 48. The load levels reached are similar in this test as compared to the 500nm beams 3&4. The load level does not rise, and it can be seen from the EBSD data in Fig. 36 that this beam was fabricated in a region with relatively few grain boundaries.

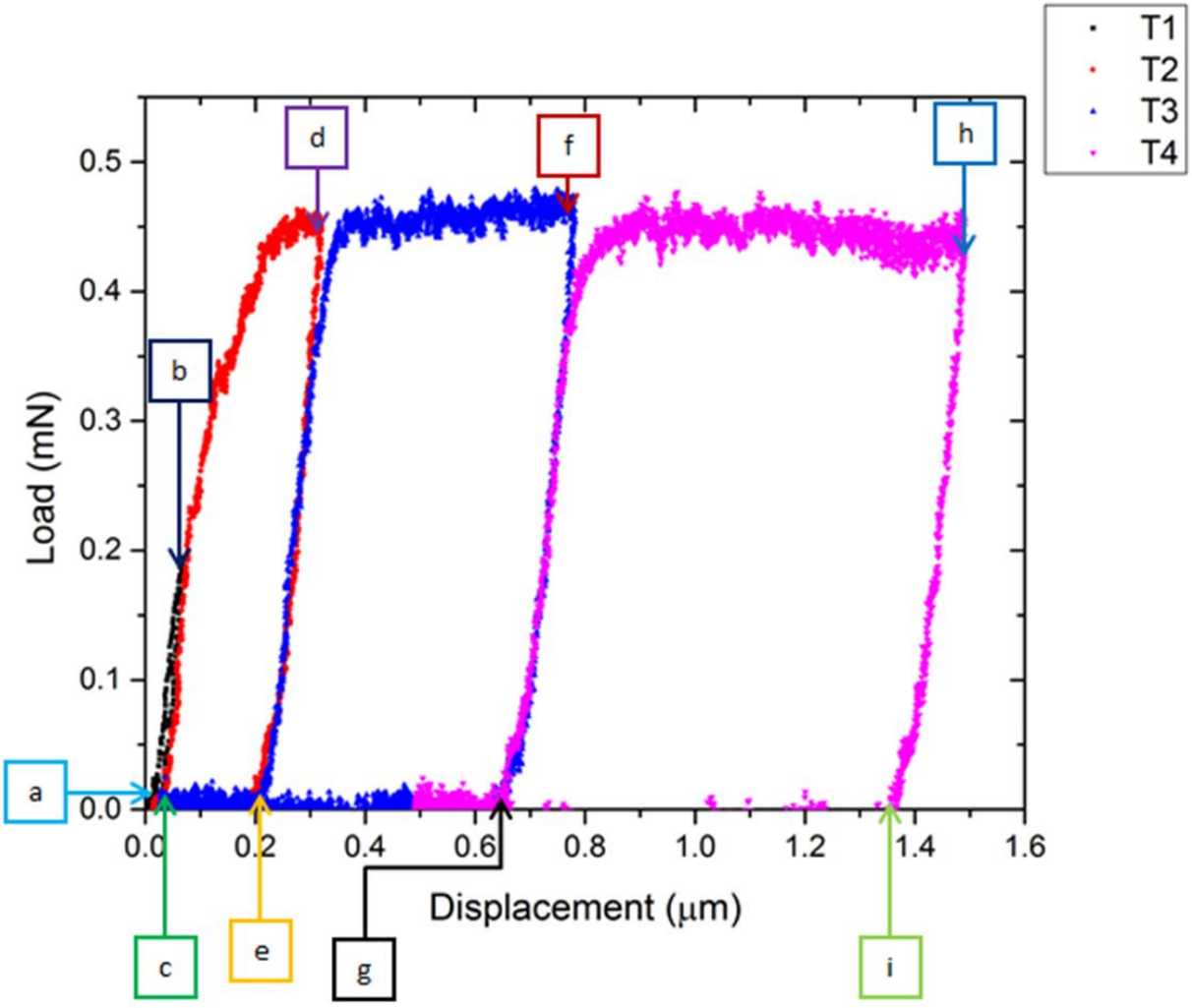

Figure 47: Load-displacement curve for 500nm beam 5, with letters designating locations of screenshots from the corresponding video

The SEM screenshots in Fig. 48 confirm highly plastic deformation. Of particular interest here is the rather poor alignment of the FIB pre-notch with regards to the center of the beam. It can be seen to be placed about 60% of the distance along the beams length from the left, rather than at the absolute center. This is attributed to the drift of the FIB, which can be very difficult to control.

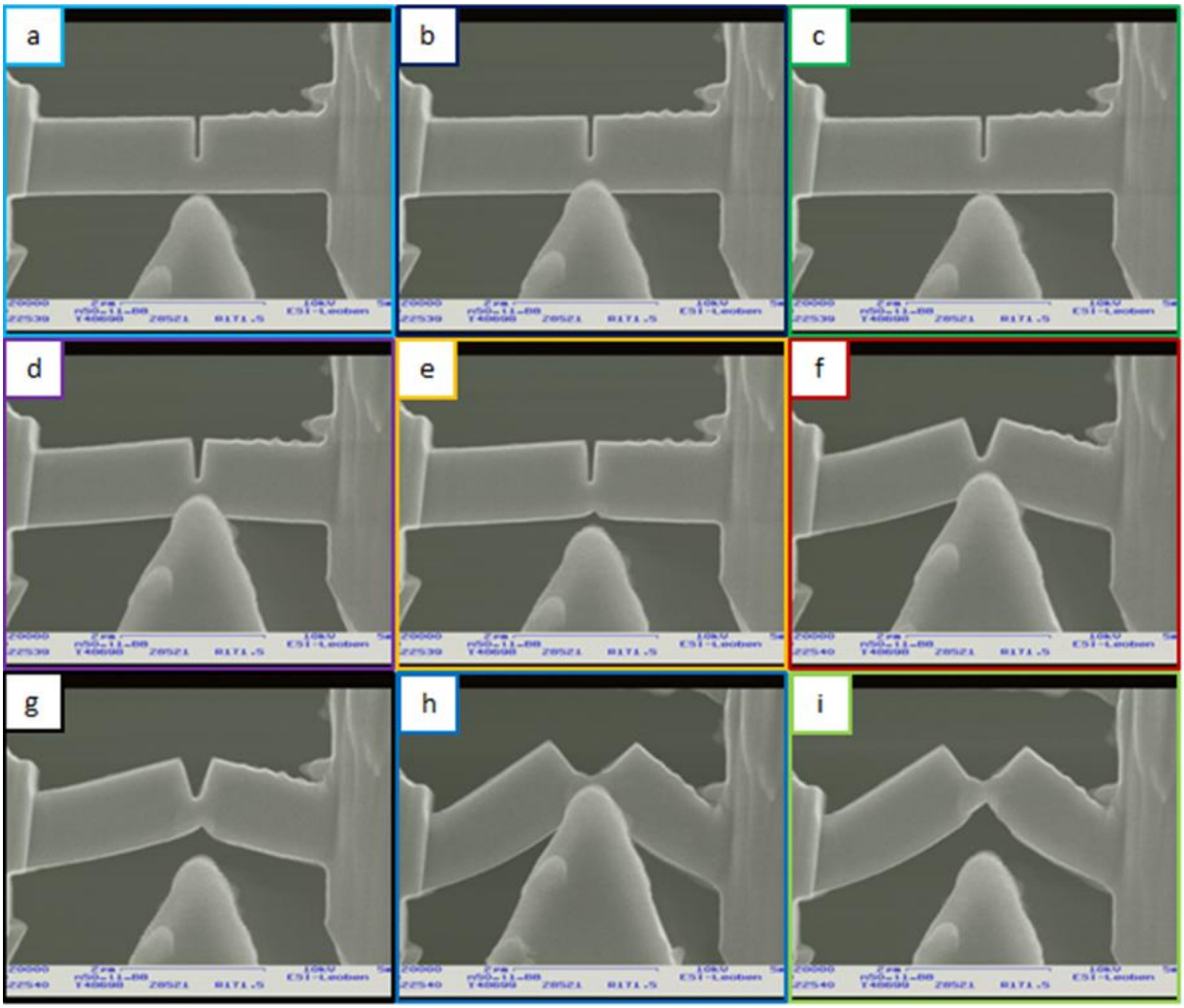

Figure 48: Selected frames from test video for 500nm beam 5, taken from corresponding locations in the load-displacement data

The load displacement data for 500nm beam 6 is shown in Fig. 49 and the corresponding stills from the test video in Fig. 50. Peculiar behavior can be observed in Fig. 49 with regards to load levels. The load levels achieved here are much less than in 500nm beam 5 initially. The

third test reloads to a level much lower than expected and then rises. Finally, in the fourth test, a load level similar to that observed in previous testing is achieved, but then quickly drops. There is no mechanistic explanation for this behavior, so instead we are forced to attribute this to drift in the detector system. At this low of a strain rate, a single test cycle takes several minutes, giving ample opportunity for drift to occur.

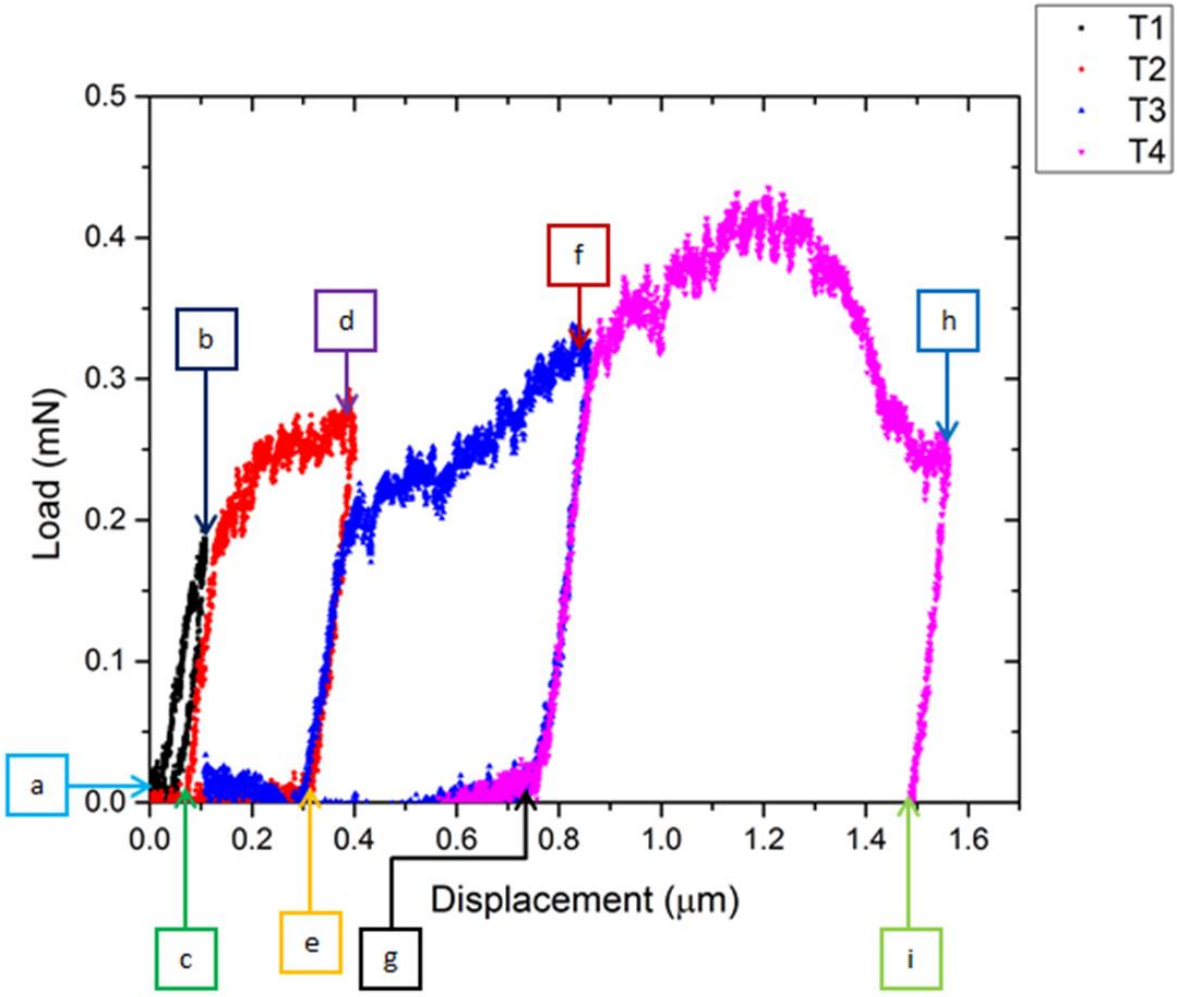

Figure 49: Load-displacement curve for 500nm beam 6, with letters designating locations of screenshots from the corresponding video

The SEM screenshots in Fig. 50 yield no surprises that would explain the odd load-displacement behavior in Fig. 49, so this supports the conclusion that it is drift in the indenter system. The behavior here is similar to the 500nm beams presented, with the opening of the crack and tearing mode of advance.

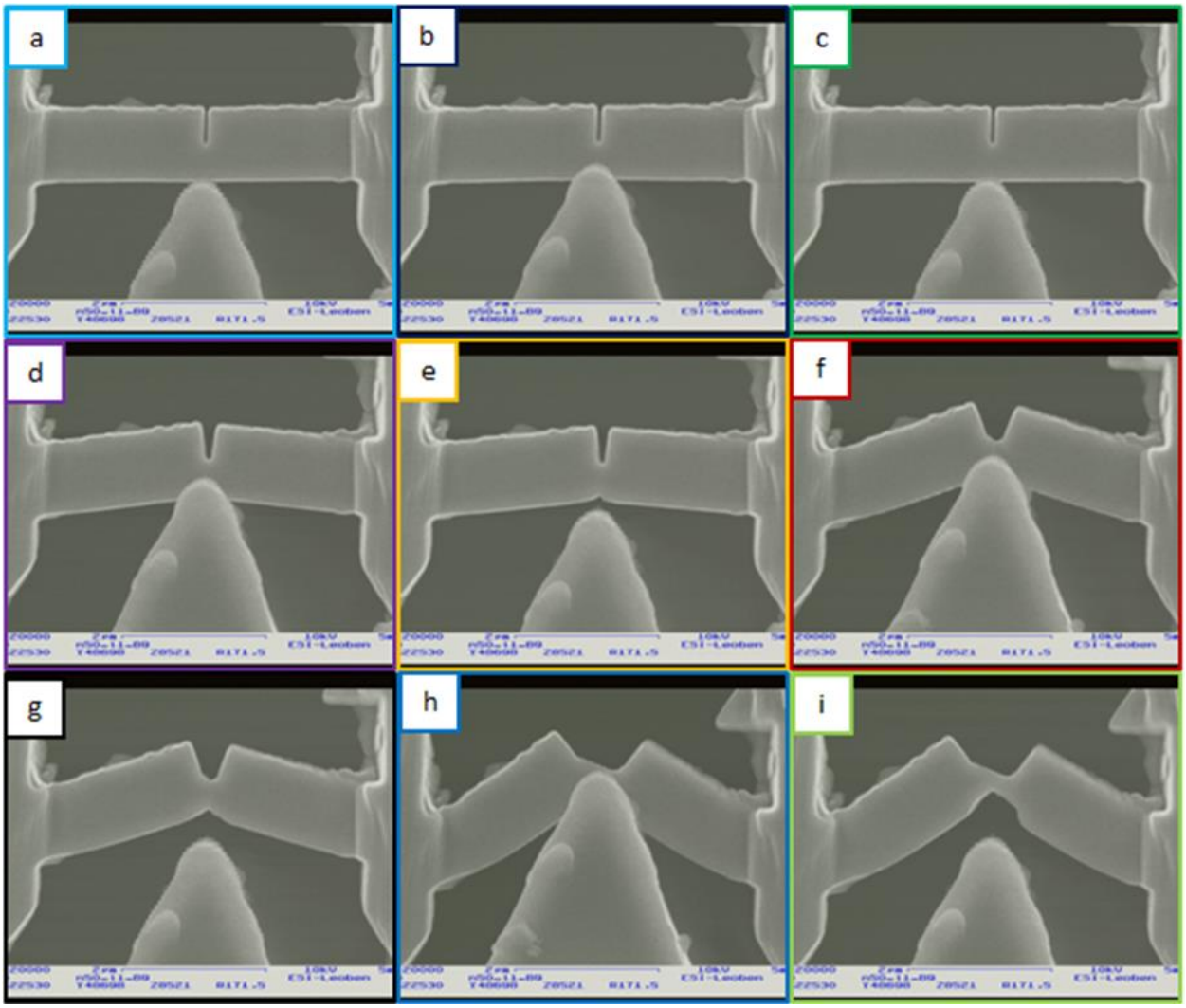

Figure 50: Selected frames from test video for 500nm beam 6, taken from corresponding locations in the load-displacement data

4.2.4: $0.004s^{-1}$ Strain Rate

500nm beams 7&8 were tested at a strain rate one fourth that of 500nm beams 5&6. The load displacement data for 500nm beam 7 is shown in Fig. 51 and the corresponding stills from

the test video in Fig. 52. It can be readily observed that Fig. 51 shows many drift artifacts similar to 500nm beam 6. The load levels achieved here are lower than is typical for 500nm beams, but this could be attributed to drift issues. In the second test, a very peculiar jog in the data can be observed, with no obvious explanation shown in Fig. 52.

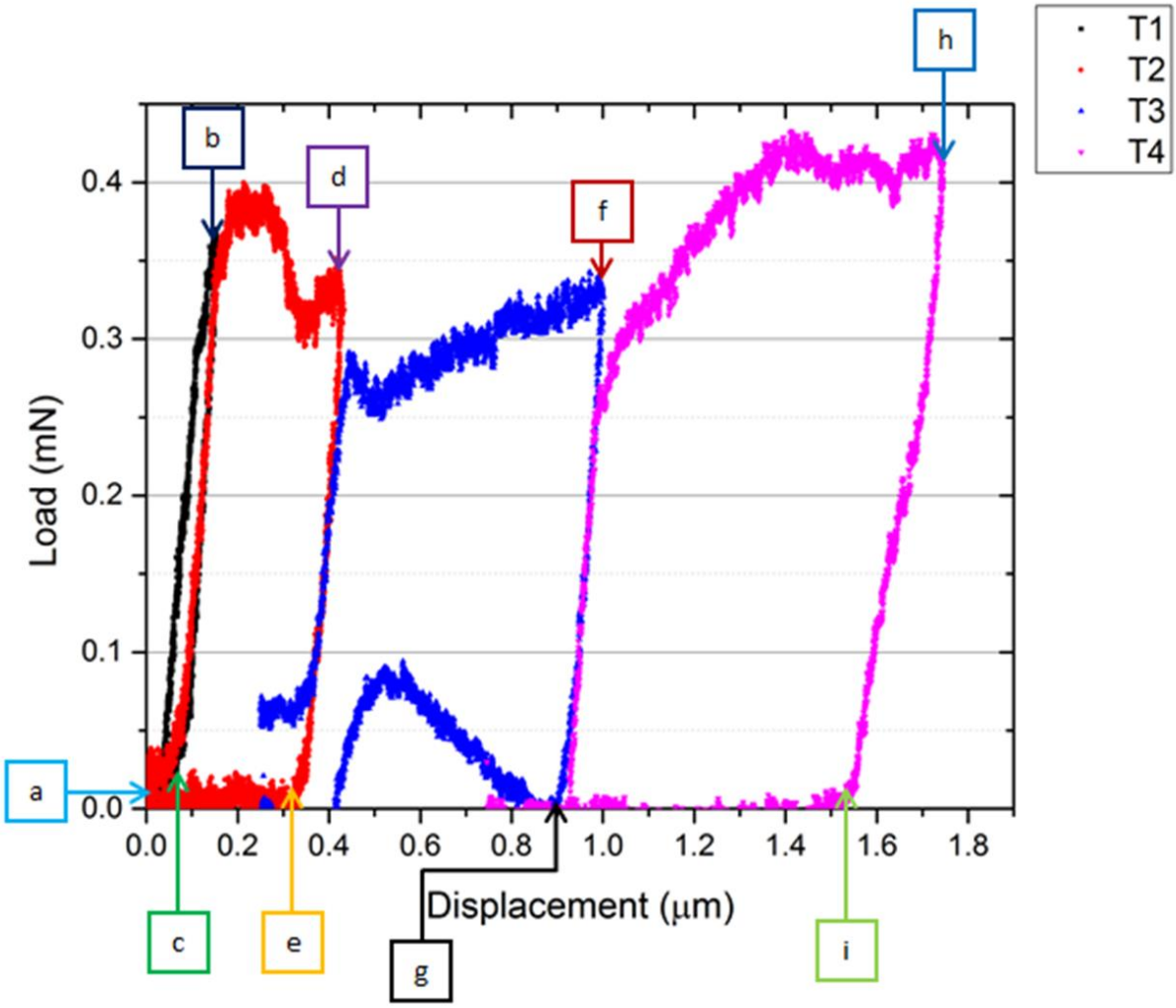

Figure 51: Load-displacement curve for 500nm beam 7, with letters designating locations of screenshots from the corresponding video

Similarly to 500nm beam 6, Fig. 52 shows no peculiar behavior to explain the artifacts in Fig. 51. Typical ductile crack opening and tearing advance can be observed. It is noteworthy that the residual impression from the indenter seems somewhat reduced here; this could be

explained by increased deformation occurring at the notch as compared to the impression left by the indenter.

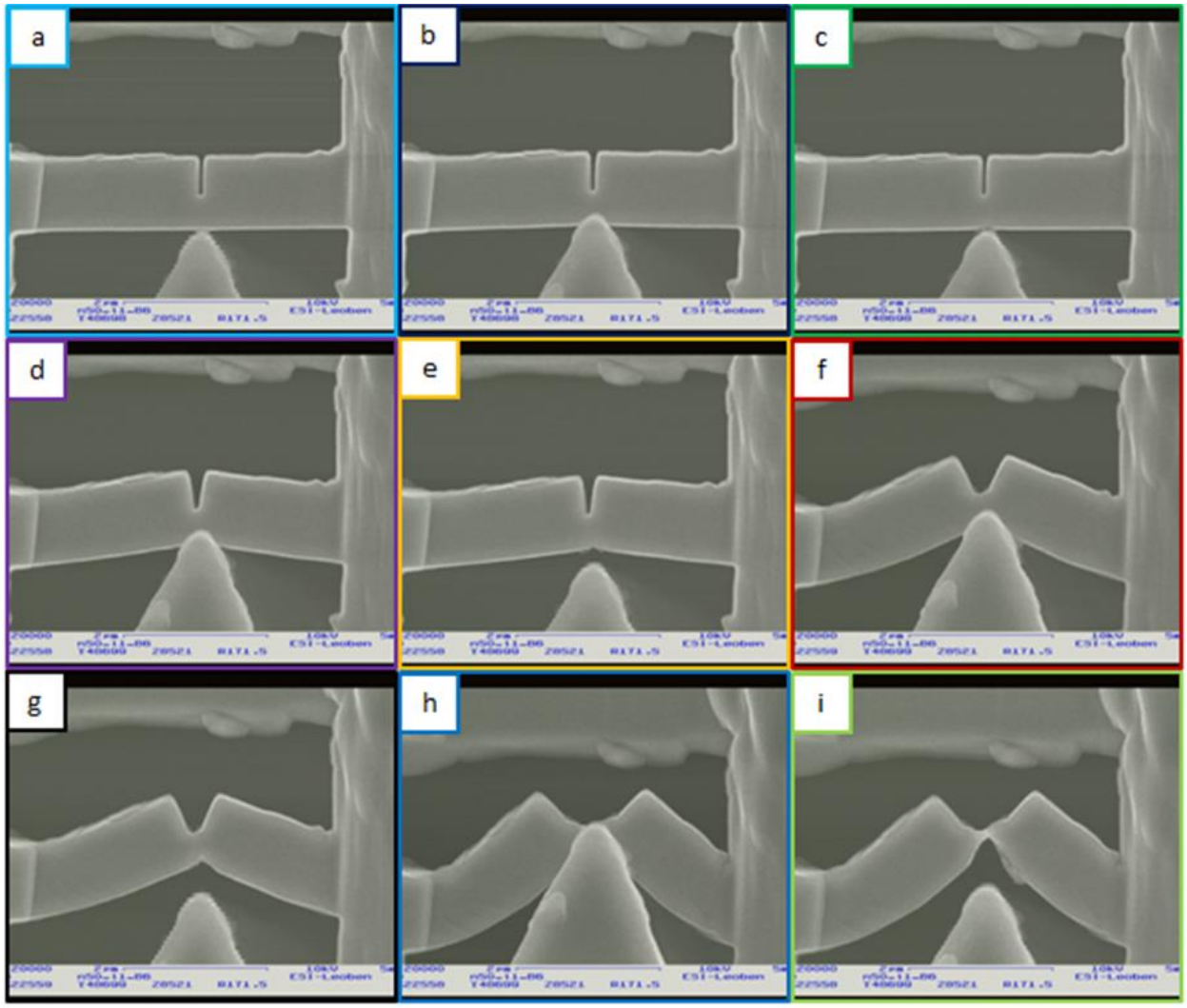

Figure 52: Selected frames from test video for 500nm beam 7, taken from corresponding locations in the load-displacement data

The load-displacement data from 500nm beam 8 is shown in Fig. 53 and the corresponding stills from the test video in Fig. 54. The data here is very similar to the first beam shown for this strain rate, the average load level is lower than was observed at the higher strain rates and there are several artifacts in the data. This helps confirm these artifacts as drift, as it can be seen they are enhanced with decreasing strain rate.

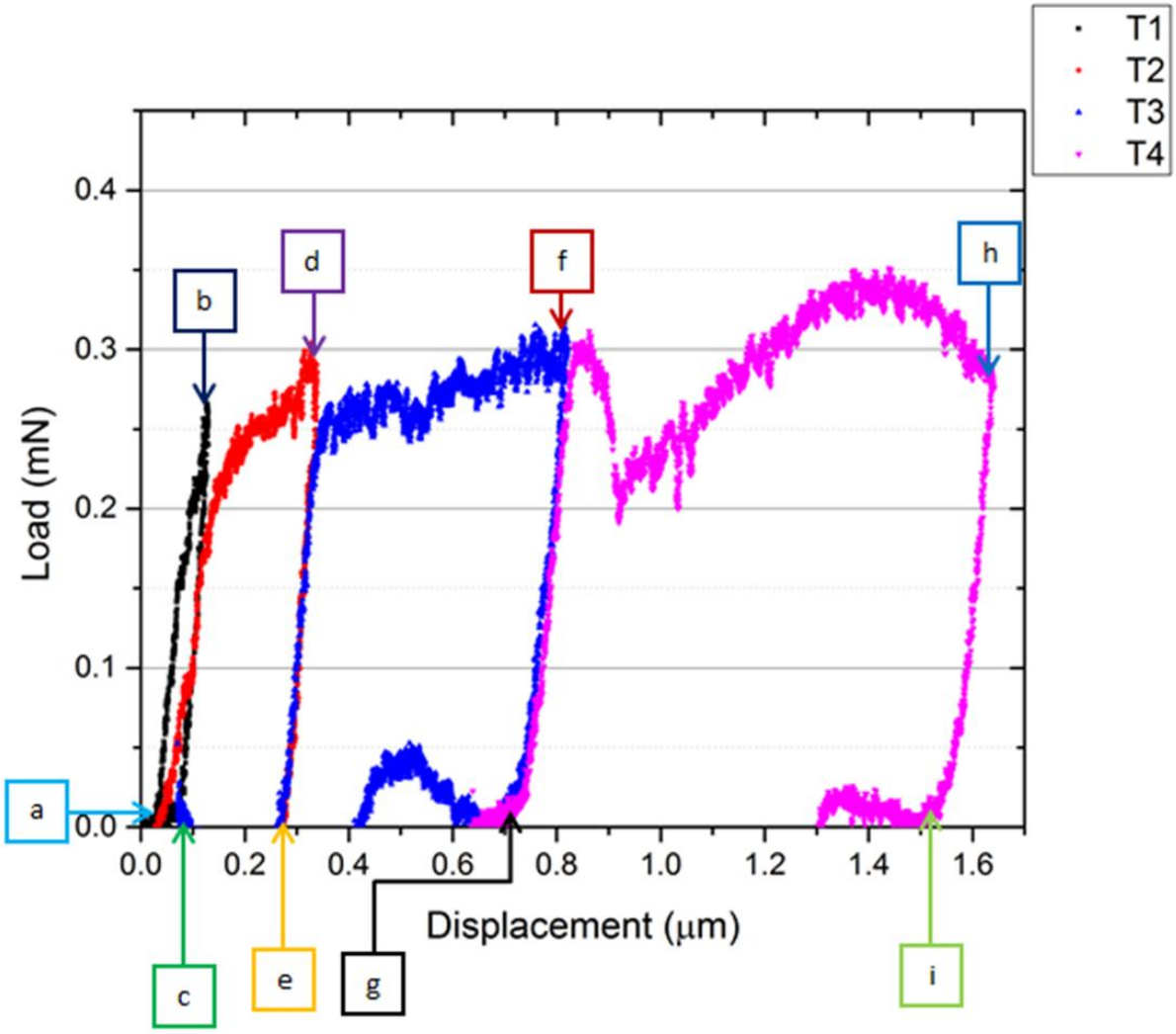

Figure 53: Load-displacement curve for 500nm beam 8, with letters designating locations of screenshots from the corresponding video

Figure 54 shows the typical ductile behavior observed for all the 500nm beams. One small curiosity is a piece of material that appears grey in frame f, which eventually tears itself loose in frame h. This is not inconsistent with the other tests, as it shows a tearing mode of ductile crack advancement, but in this case appears at the surface of the beam where it is readily observable.

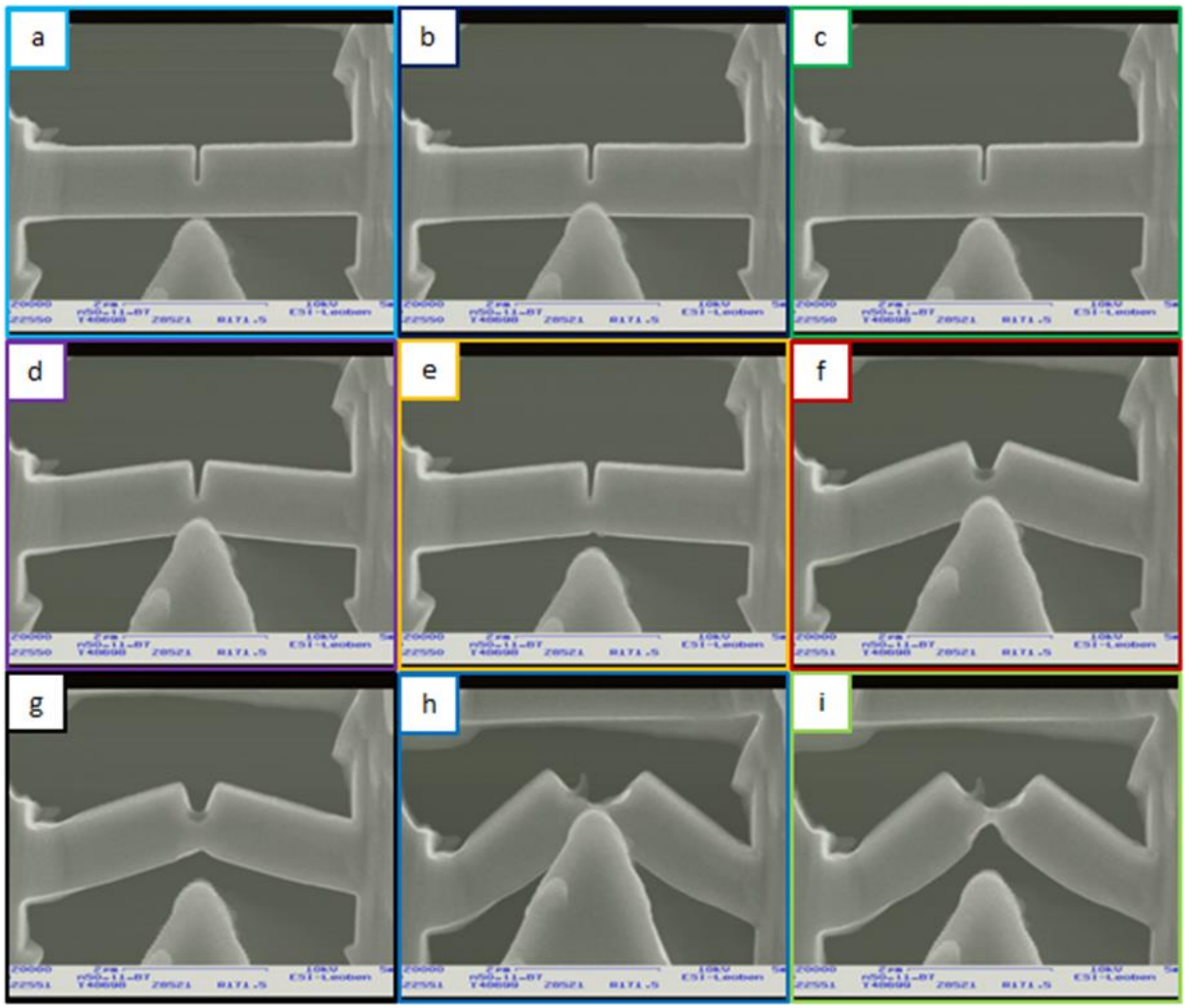

Figure 54: Selected frames from test video for 500nm beam 8, taken from corresponding locations in the load-displacement data

4.2.5: Post-mortem imaging of 500nm beams

High resolution SEM post-mortem imaging was performed on these 500nm specimens at 10keV. These images are presented in Fig. 55. The images show that these beams have undergone higher strains than the 2500nm beams and as a result large slip steps in the regions with a coinciding rotation of the overall sample. Fig. 55d shows a top view of one of the beams post indent, which reveals the twisting in the beam due to large amounts of plastic deformation.

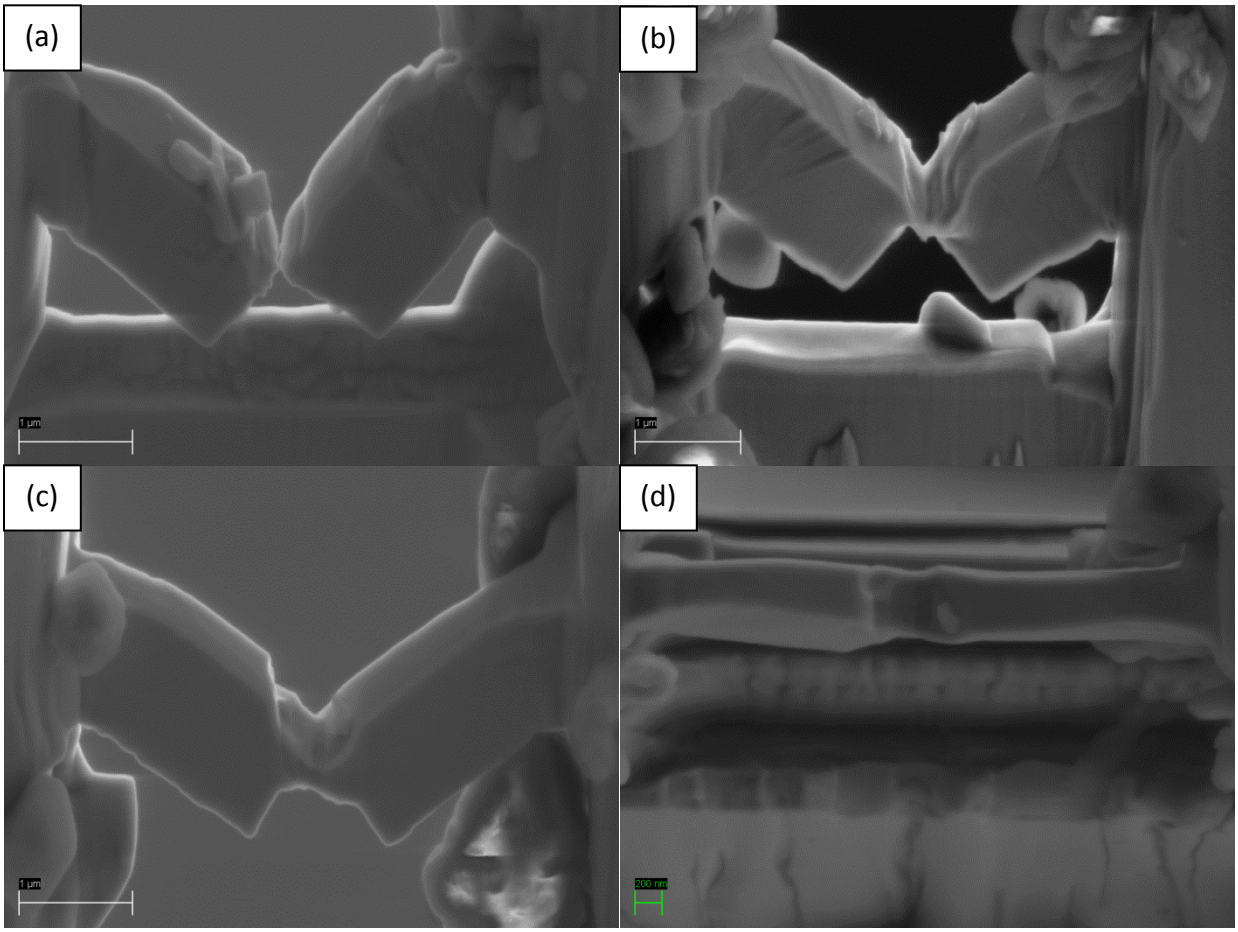

Figure 55: Post-mortem SEM imaging of various 500nm beams, showing significant plasticity and twisting along the beam axis

4.3: 100nm Beams

The smallest beams fabricated were 100nm in thickness. This is too small for the SEM to properly resolve, but is in an appropriate range to be electron transparent in the TEM. Testing was performed in-situ the TEM using the Hysitron PI-95 Picoindenter as discussed previously. Bright field imaging was used for all presented tests; the benefits of dark field imaging are many, but this was not possible as the diffraction patterns acquired from the beams showed many extra spots, similar to a nanocrystalline specimen. These 100nm beams only have two grains contained within at most, so this is puzzling. A likely explanation would be growth of some kind of layer on the surface, possibly by redeposition of FIBed material. During fabrication of the

100nm beams, an incident occurred where a 1pA aperture was inserted into the FIB as part of a desire to use low doses for final cutting. However, this aperture is mislabeled and is actually a 20nA aperture, which destroyed about half the specimens that were prepared. The re-deposition could have occurred during this step; other possibilities would be the growth of an oxide layer (unlikely as Nitronic 50 is very corrosion resistant) and heavy gallium damage such that significant amorphization of the specimens took place. This latter is also reasonable; however it would be expected to see more of this damage in the images. As can be seen in the following section, the specimens appear to be reasonably clean and have little contrast that could be attributed to crystal imperfection. A final possibility would be instrument error.

4.3.1: 1.0 strain rate

An additional added benefit to testing in the Picoindenter is the higher video framerate, which can be attributed to the intensified CCD camera the TEM is equipped with. As such, higher strain rate testing could be attempted while still acquiring a reasonable number of frames for the test video. 100nm beam 1 was the fastest test of all beams tested, at 1.0 strain rate. The load-displacement data for 100nm beam 1 shown in Fig. 56 and the corresponding stills from the video in Fig. 57. As can be seen, the electron beam notch is extremely sharp, at about a 20nm root radius of curvature. Qualitatively, the data is very similar to the larger sized beams, as the crack advances minutely through a ductile tearing mode, and the COA and CTOD are constantly increasing throughout the test such that a stable crack front is not achieved.

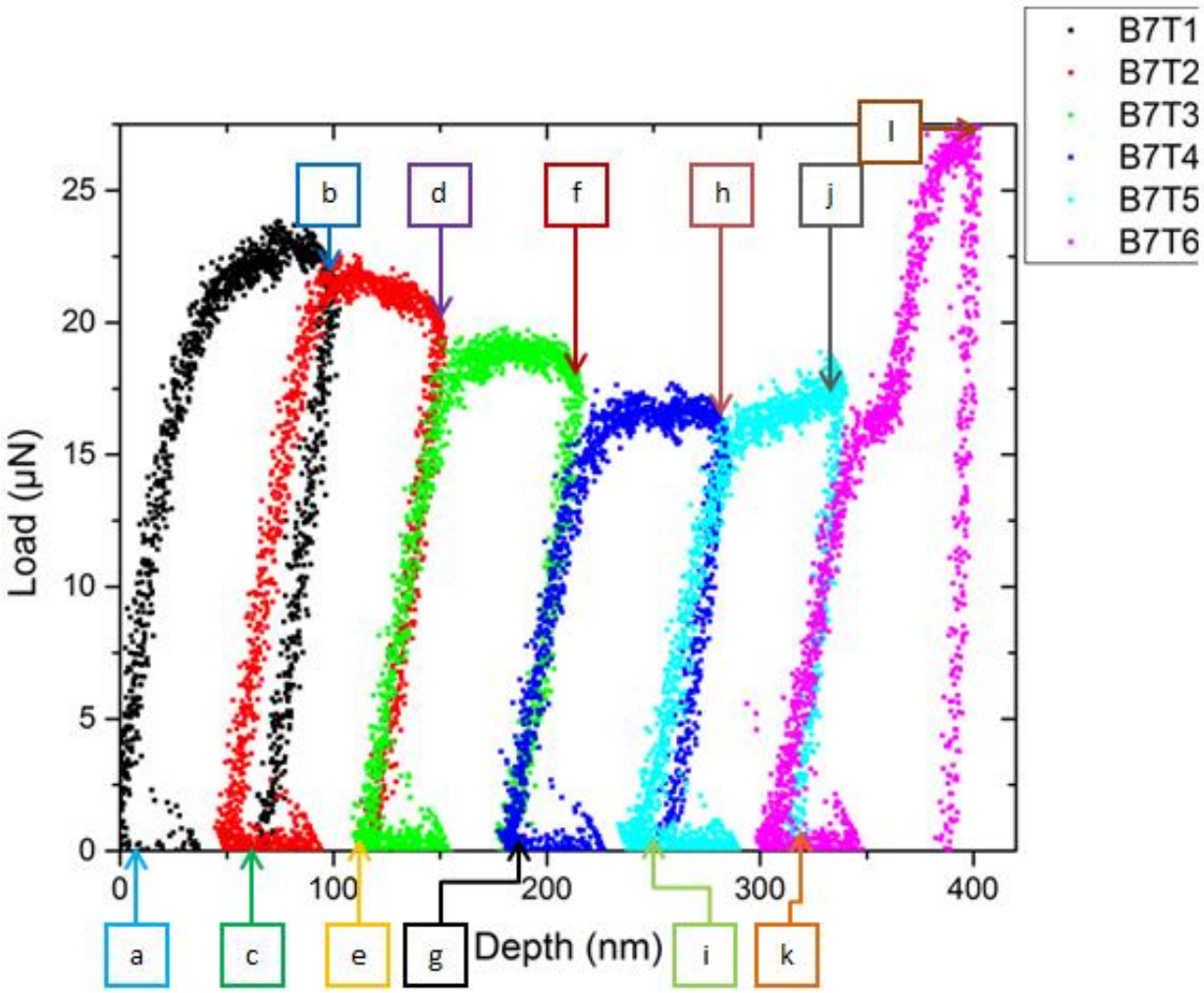

Figure 56: Load-displacement curve for 100nm beam 1, with letters designating locations of screenshots from the corresponding video

One notable difference present here and many other tests at this scale is that the load decreases stepwise in the plastic regime. This may be correlated to formation of two secondary cracks, on the opposite beam edge near the clamping points. These were not observed in the larger beams; the greatly reduced size of these tests would place them further into plane stress, but it's hard to imagine why this would have an effect since even the largest specimens were well into the plane stress regime. Another possible explanation is misalignment of the wedge indenter which occurred in all of the tests of about 10 degrees, which couldn't be avoided. It is not seen in the

images as the stage was alpha tilted to compensate for this misalignment, to enhance visibility. Also, since the scale of testing is smaller, the relative scale of tip asperities is enhanced, further complicating resulting stress states in the beam. A final possibility is a size effect involving the distance from the notch root to the neutral axis, which is greatly reduced. Since the normal stress goes to zero at the neutral axis, dislocations would be slowed in this region and would exert a back stress on the dislocation source that is much larger comparative to the larger beams tested.

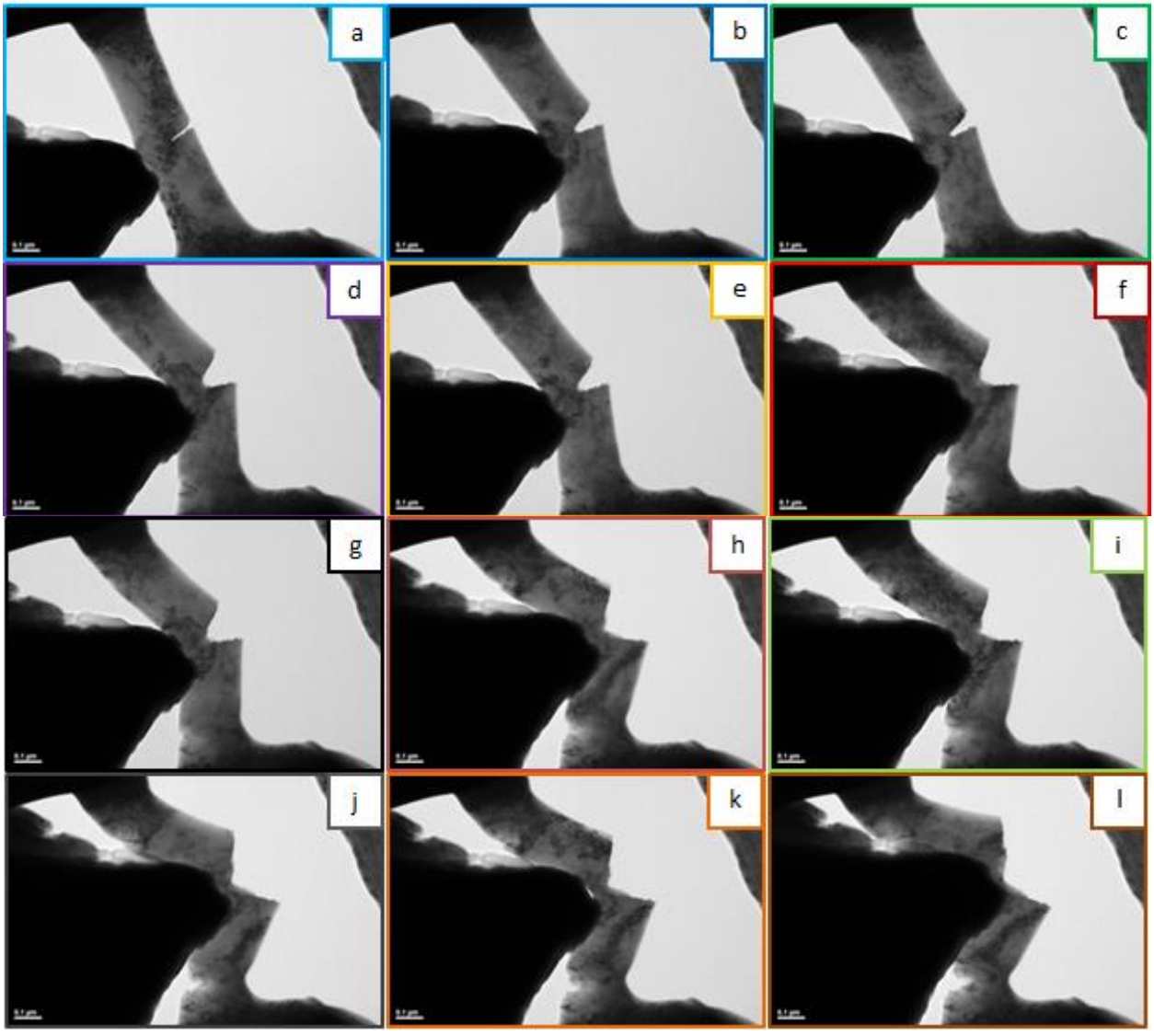

Figure 57: Selected frames from test video for 100nm beam 1, taken from corresponding locations in the load-displacement data

It can be observed that as testing proceeds, a dark contrast band expands from the central region between the tip and notch, and later near where the secondary cracking occurs. Though these could be bend or strain contours, they are not completely relieved upon unloading as can be seen. This suggests that the contrast arises from dislocation processes, which then may correlate to the plastic zone size. Although zone axis alignment and/or dark field imaging was not achieved, some aspects of the dislocations should be visible, and since the specimens would contain a high density of dislocations, it could produce an observable contrast effect.

4.3.2: 0.25 strain rate

100nm beam 2 was tested at a strain rate one quarter that of 100nm beam 1. The load-displacement data for 100nm beam 2 is shown in Fig. 58 and the corresponding stills from the video is shown in Fig. 59. As can be seen in Fig. 59, the contrast is much darker in this beam than the others tested, suggesting that it is much thicker. The loads are correspondingly much higher than the other beams. 100nm beam 2 deformed in qualitatively the same way as the previous, though it can be seen that there is some amount of load increase in the post-yield data before gradually decreasing. Upon load decrease, it can be seen that there is a series of load-drops, which correspond to the formation of a large slip step on the right side of the beam as seen in Fig. 59. This therefore is consistent with the idea that some type of size effect inhibiting deformation at the central region of the beam between the indenter and the notch root then causes subsequent deformation to occur in the secondary stress concentration sites arising from the clamping constraint of the beam.

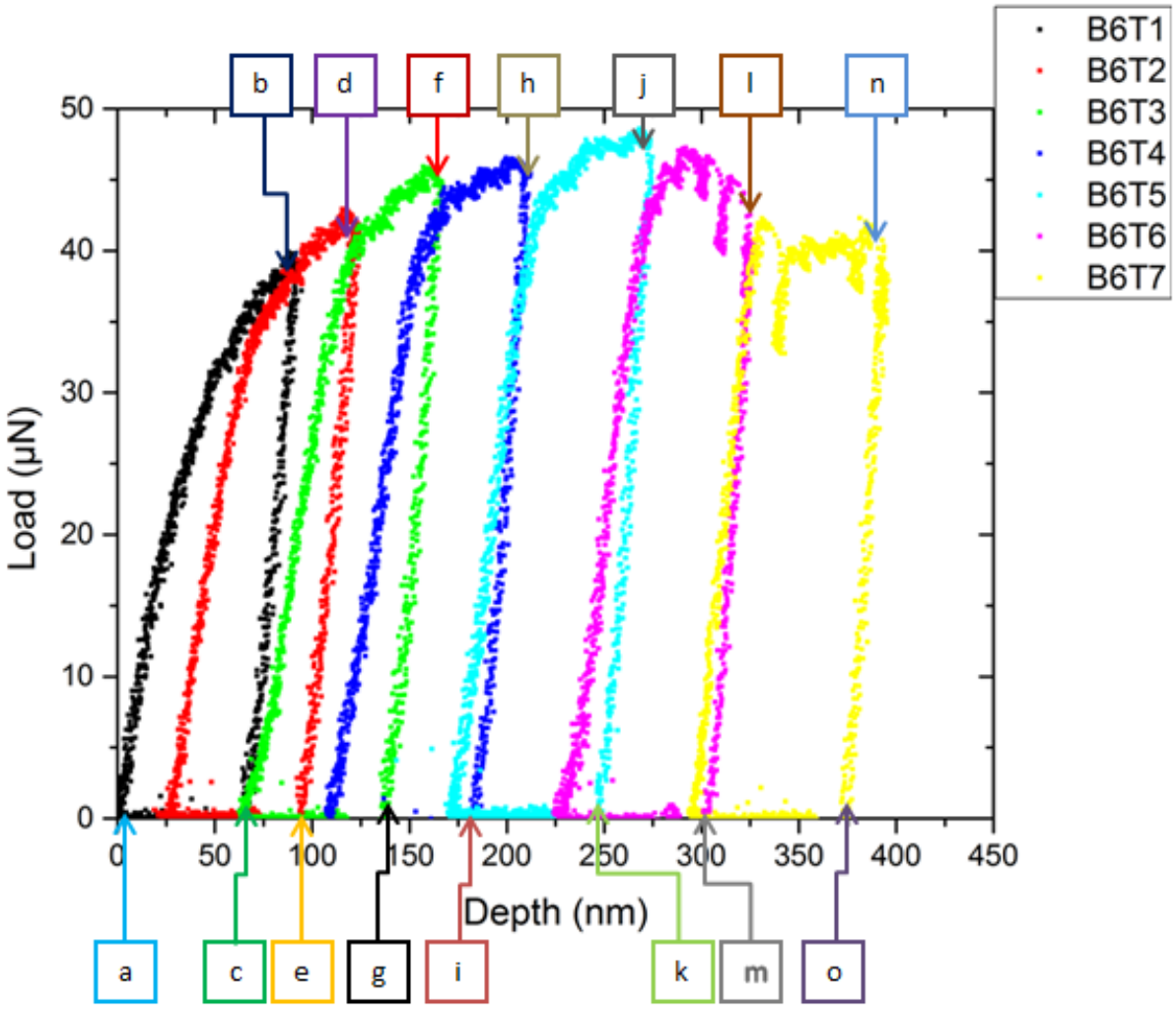

Figure 58: Load-displacement curve for 100nm beam 2, with letters designating locations of screenshots from the corresponding video

Contrast bands showing the plastic zones are not visible in this beam, but are likely obscured by the dark thickness contrast present. Determination of thickness of these 100nm beams was actually more accurate than the larger 500nm and 2500nm specimens due to a special technique for measuring thickness. This was done by gathering an electron energy loss spectrum (EELS) and comparing the intensity of the zero-loss peak to the plasmon peak, assuming a Z of 26. This beam was confirmed to be 160nm thick, while the other 100nm beams were much

closer to 100nm. Nevertheless, the beam deforms in the predicted highly ductile manner, with a particularly pronounced tearing at the root that develops later into the testing cycle.

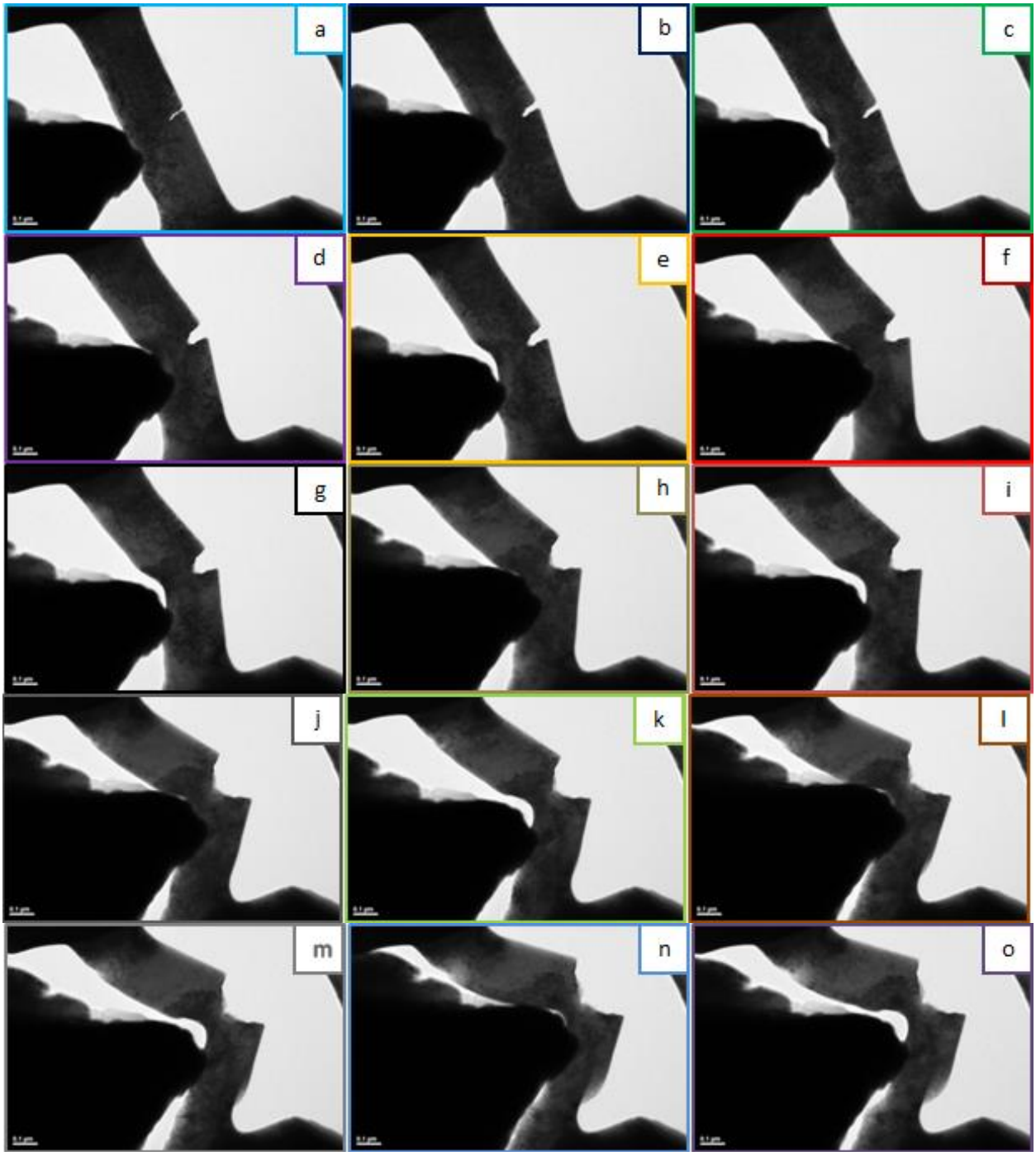

Figure 59: Selected frames from test video for 100nm beam 2, taken from corresponding locations in the load-displacement data

4.3.3: 0.1 strain rate

100nm beam 3 was deformed at a strain rate 40% slower than 100nm beam 2. The load-displacement data for 100nm beam 3 is shown in Fig. 60 and the corresponding stills from the video are shown in Fig. 61. Load levels are much lower than the previous two beams, but it can be observed in Fig. 61 that the width of the beam is less than it should be. The typical highly plastic behavior is observed here, but the decrease in the load does not occur until the last cycle, where it actually appears that the beam is fully fractured upon unloading.

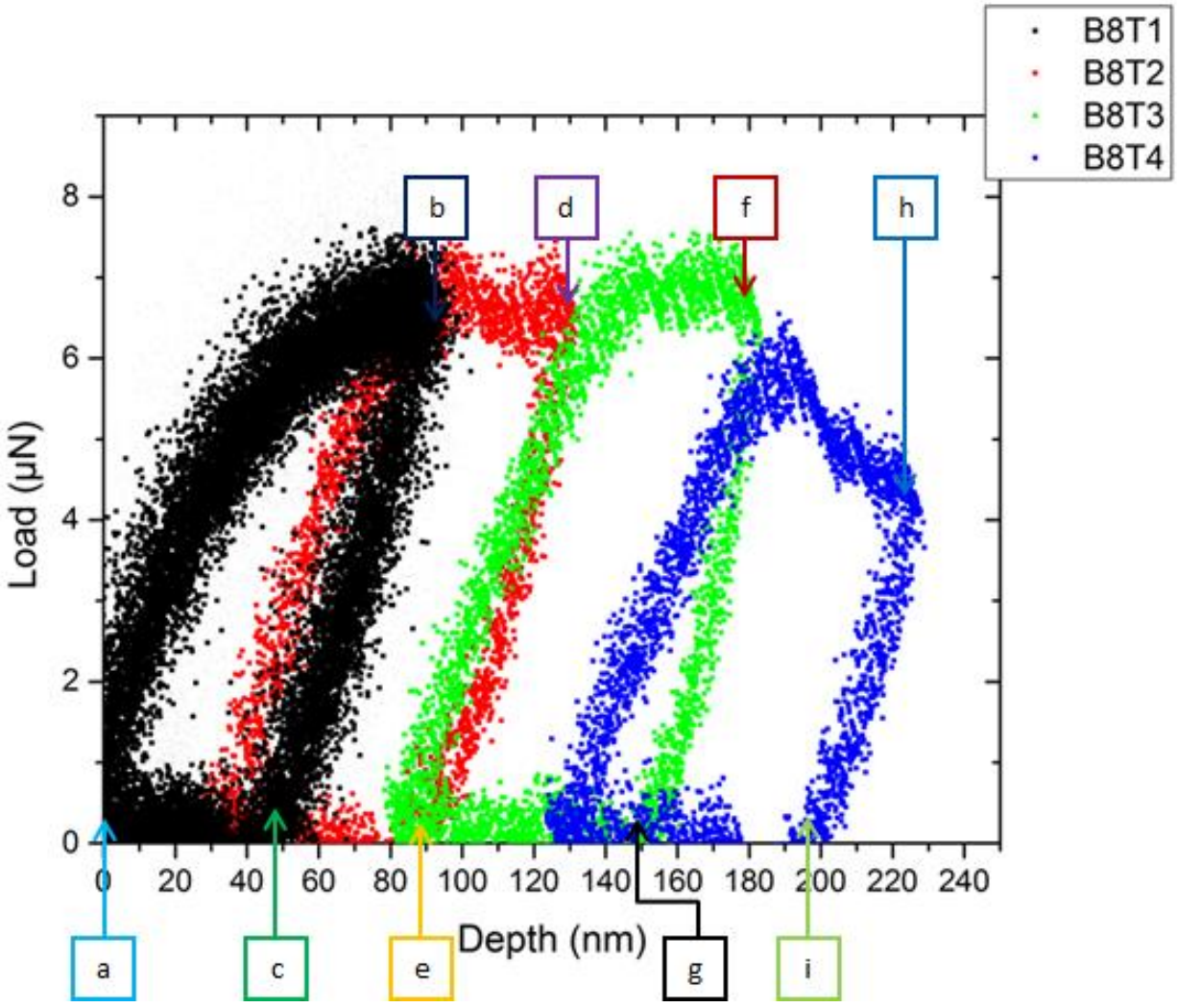

Figure 60: Load-displacement curve for 100nm beam 3, with letters designating locations of screenshots from the corresponding video

Though it is not as pronounced as in some of the other beams at this scale, contrast effects can be observed in the highly plastically deformed regions of this beam as well, though in the central region between the indenter and the notch, the contrast actually brightens. The contrast does not necessarily have to get darker to be attributed to defects, so this may be correlated to dislocation processes similarly to the other 100nm beams. As can be seen in Fig. 61, this beam has an overall contrast similar to the 1.0 strain rate beam. Secondary cracks also form in the expected stress concentration due to the clamping constraint during the last test cycle.

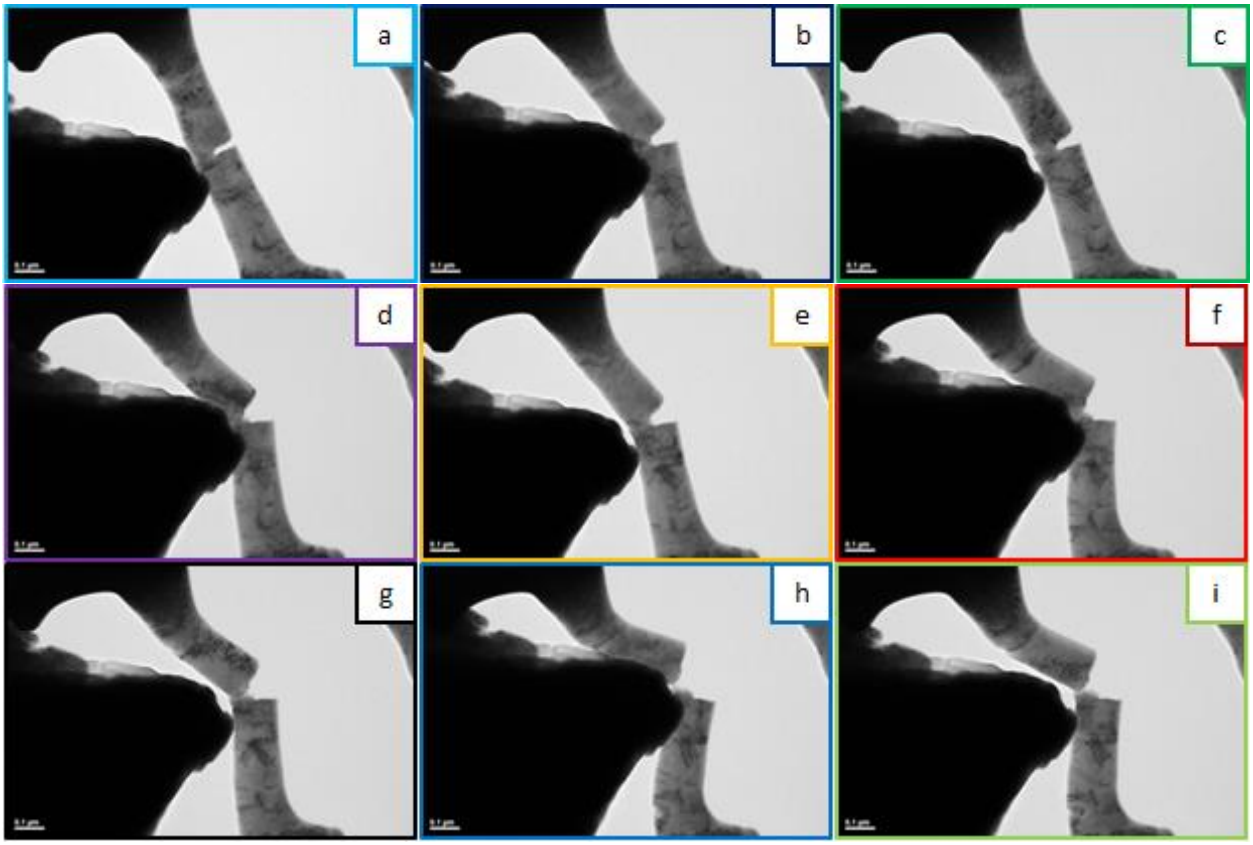

Figure 61: Selected frames from test video for 100nm beam 3, taken from corresponding locations in the load-displacement data

4.3.4: 0.025 strain rate

100nm beam 4 was tested at a strain rate one quarter that of 100nm beam 3. The load displacement data for 100nm beam 4 is shown in Fig. 62 and the corresponding stills from the video are shown in Fig. 63. It can be seen that the initial achieved load level is comparable to 100nm beam 1, which has a very similar geometry to this beam. However, the stepwise decrease in the load with each test cycle is much more dramatic.

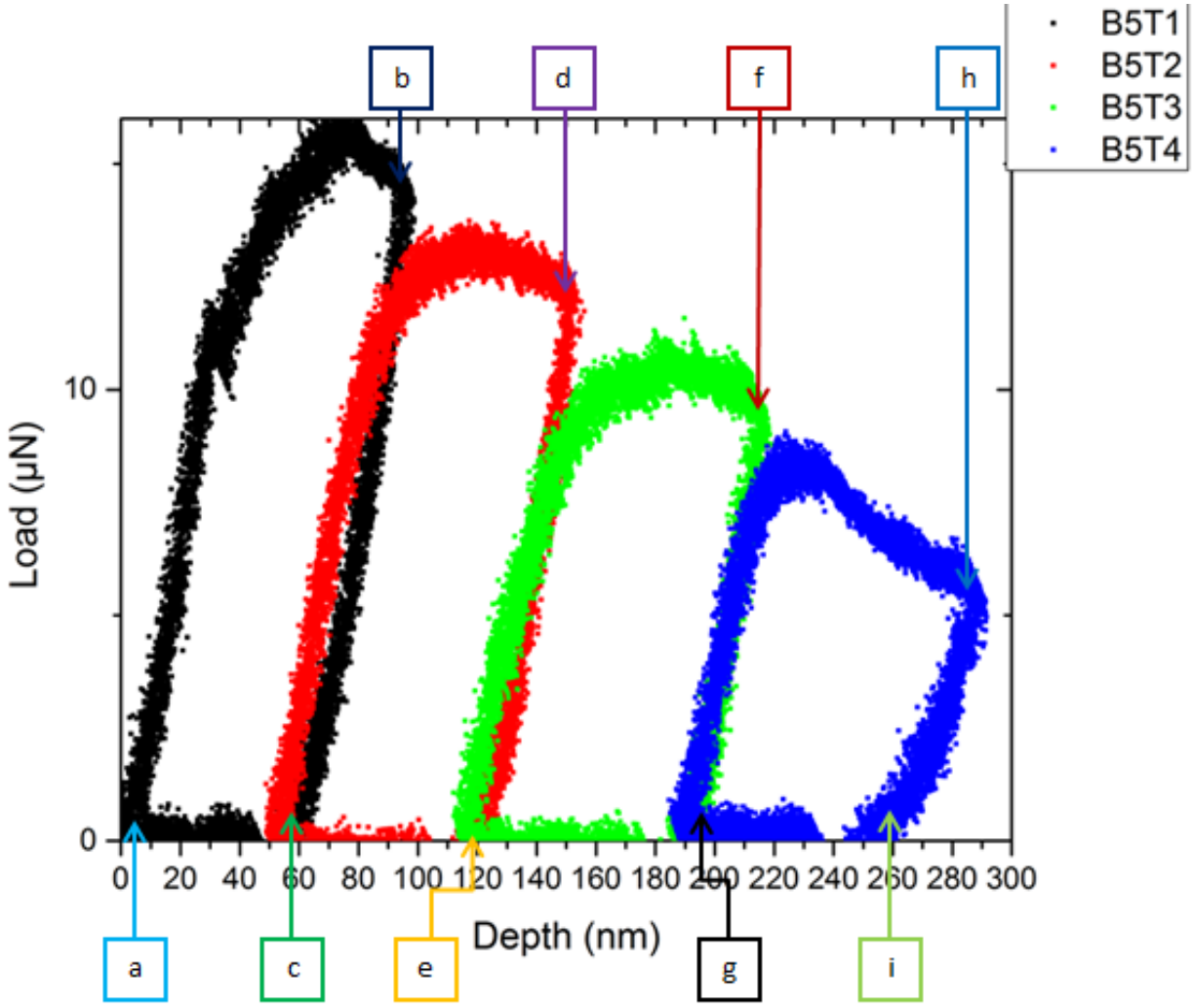

Figure 62: Load-displacement curve for 100nm beam 4, with letters designating locations of screenshots from the corresponding video

It can be seen in Fig. 63 that the secondary cracking at the sides of the beam begins very early in the test. The crack flanks open unequally in this test, which is very pronounced in the intermediate loadings, due to slightly inaccurate notch placement. Other than this, the test is comparable to the other beams, with a strong contrast effect present in the plastic zones. In this case, there are strong dark contrast changes in the secondary cracks but bright contrast changes at the base of the notch. The beam approaches a fully fractured state in the final loading and shows a typical drop in the load at this point.

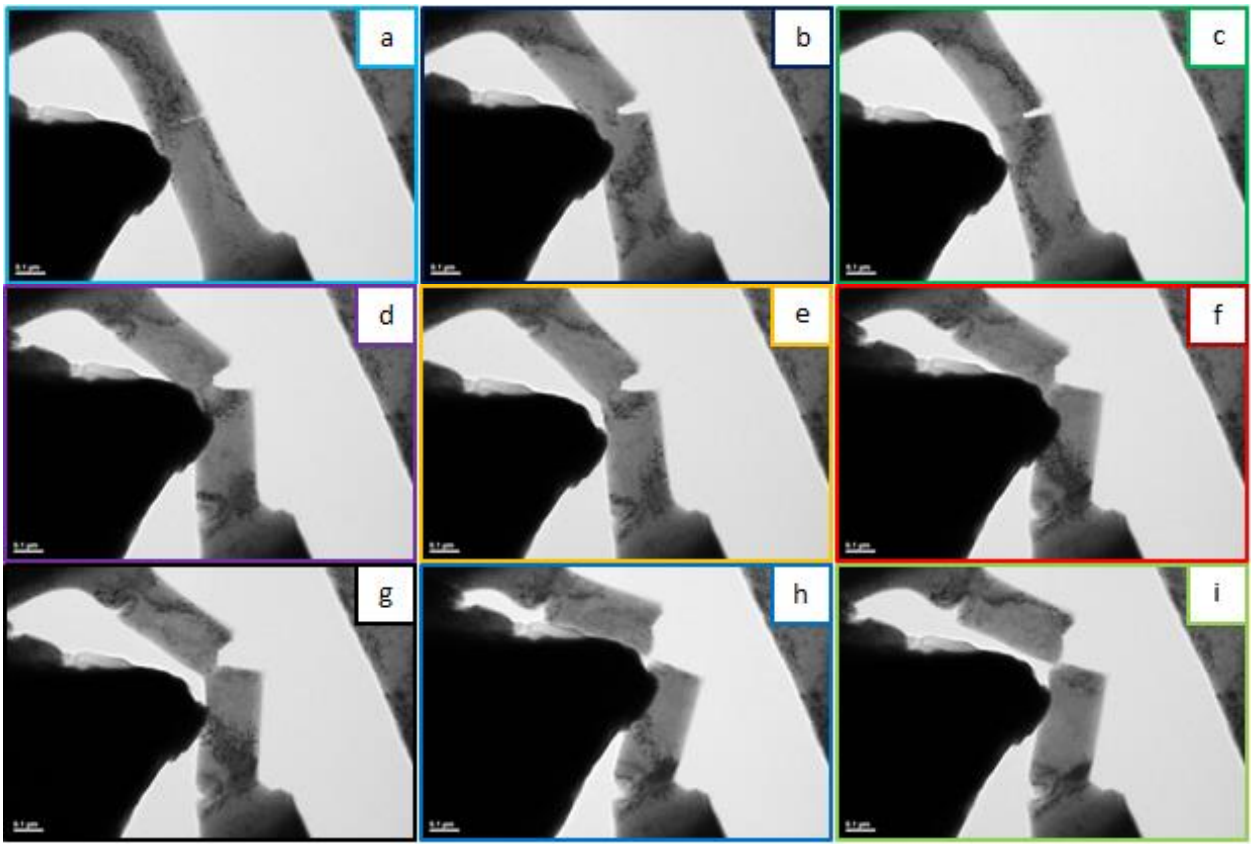

Figure 63: Selected frames from test video for 100nm beam 4, taken from corresponding locations in the load-displacement data

4.3.5: 0.005 Strain Rate

100nm beam 5 was tested at a strain rate one fifth that of 100nm beam 4. The load-displacement data for 100nm beam 5 is shown in Fig. 64 and the corresponding stills from the test video are shown in Fig. 65. The load levels are very comparable to 100nm beams 1 and 4, which is expected as the specimen geometry is similar.

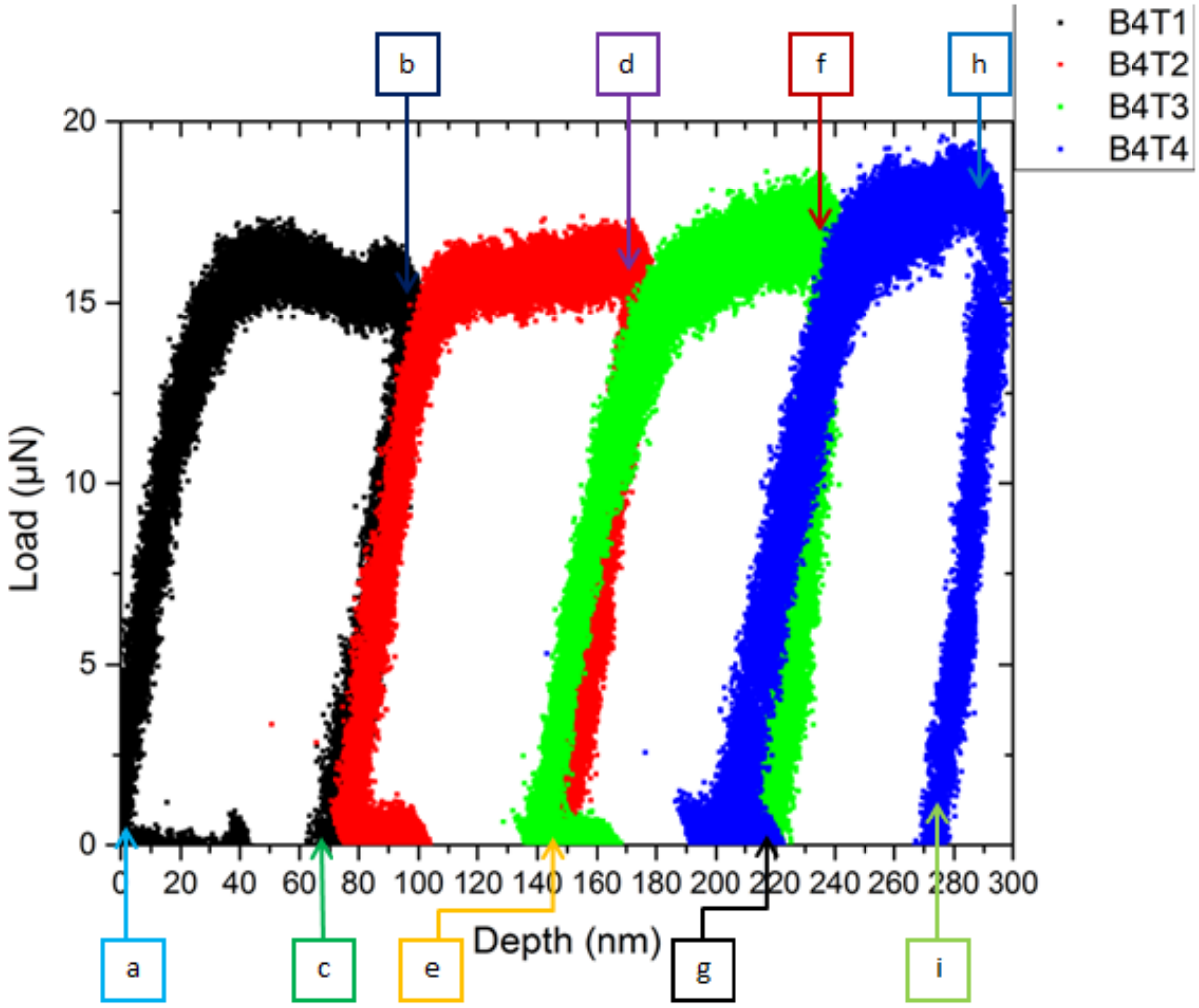

Figure 64: Load-displacement curve for 100nm beam 5, with letters designating locations of screenshots from the corresponding video

Strong contrast effects can also be observed here at the root of the notch. There is no dramatic load drop in this data, and the secondary cracking does not occur. In the last cycle, it can be observed that a large scale slip step is formed on the right side of the beam. Load drops corresponding to this are not easily observed in the load-displacement data. This is likely due to the relatively higher data rate, since this strain rate is the slowest of all beams tested, which masks the load drops in the data.

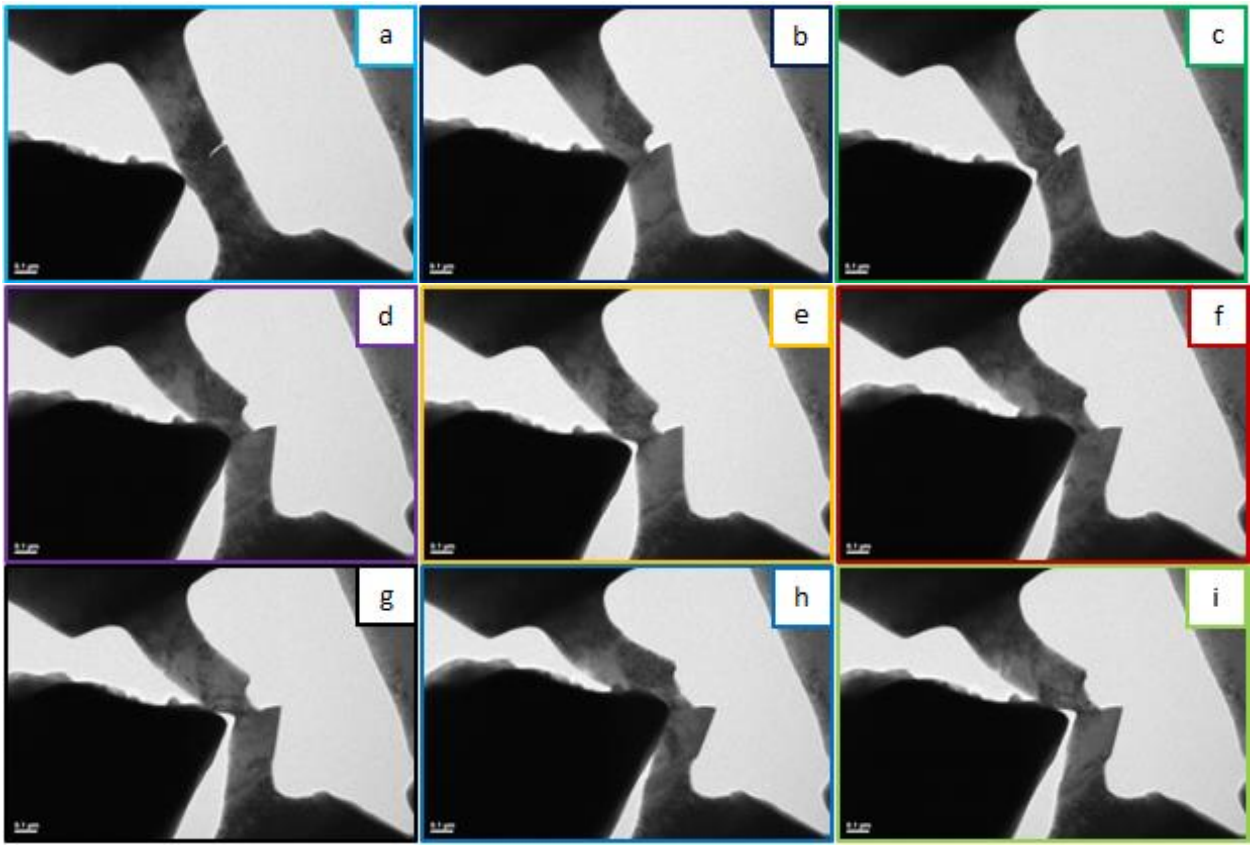

Figure 65: Selected frames from test video for 100nm beam 5, taken from corresponding locations in the load-displacement data

Chapter 5: Analysis and Discussion

5.1: Fracture toughness determinations

Measurements needed for fracture toughness calculations were taken from the video stills presented in the previous section as shown in Fig. 66. For the thickness determinations, the 500nm and 2500nm beams were determined via the FIB, while the 100nm beams were determined by EELS, by comparing the Zero-loss peak intensity to the plasmon peak intensity, assuming an average Z of 26.

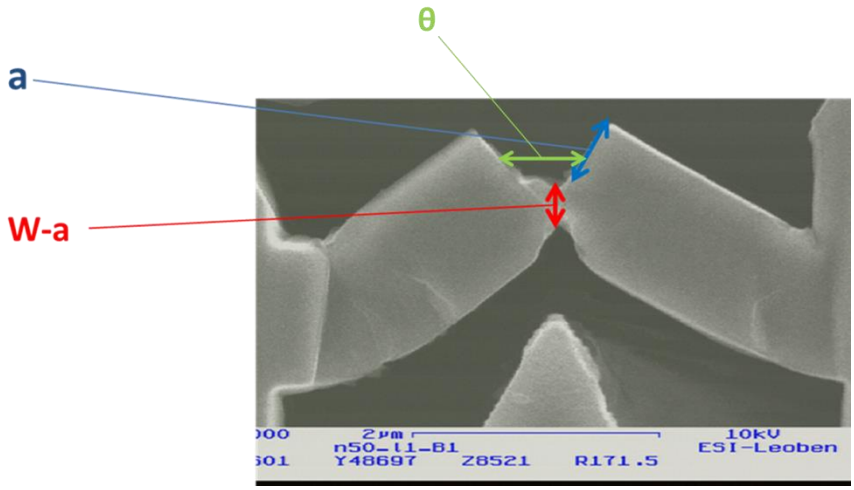

Figure 66: SEM micrograph showing how measurements were made from the video for K_I analysis

A variety of methods can be employed to analyze this data, as briefly overviewed in the background sections of this report. The ASTM E 399 standard is:

$$K_I = \frac{PL}{BW^{3/2}}Y \tag{24a}$$

$$Y = \frac{3(a/W)^{1/2}\left[1.99 - a/W(1-a/W)\left(2.14 - \frac{3.93a}{W} + 2.79\left(\frac{a}{W}\right)^2\right)\right]}{(1+2a/W)(1-a/W)^{3/2}}. \tag{24b}$$

However, we don't expect this to apply to this data due to the clamped ends of the beam, which means that elastically this method overestimates the stess intensity at the crack tip. Conversely, since this analysis is purely elastic, it should underestimate the true fracture toughness of these beams. A more refined approach for elastic fracture toughness given by Bakker can also be employed, presented as Eq. 29 [73]:

$$K_I = \sigma_b \frac{f_K(\alpha)}{(1-\alpha)^{3/2}} \sqrt{\pi a} \tag{29}$$

Where f_k is a geometric function shown as Eq. 30:

$$f_k(\alpha) = \frac{1.0731 - \alpha(1-\alpha)\left(1.1980 - 5.1240\alpha + 7.3327\alpha^{\frac{3}{2}} - 3.1403\alpha^2\right)}{1 + 1.8706\alpha} \tag{30}$$

where $\alpha = a/W$. Another issue with these elastic approaches is that the indenter punches into the sample, thereby reducing the section in the center of the beam. This is accounted for simply by measuring the impression post-compression and utilizing the reduced central ligament in these equations.

We should also consider a *J*-integral approach to account for the observed ductility in the sample. These approaches should be more accurate regarding the clamped ends, as they simply rely upon measuring the strain energy put into the sample. The approach works the best if the deformation is located in the central region. In all performed testing, we do observe that this is the case but sometimes observe the beams deform at the ends too, thanks to the clamping constraints. As such, this approach is not flawless. The first method one would employ is a simple *J*-integral of load vs. axial displacement, which is determined by Eq. 31 [74]:

$$J = \frac{2}{B(W-a)} \int_0^{\delta} P \, d\delta \tag{31}$$

Which simplifies to Eq. 32:

$$J = \frac{2P\delta}{B(W-a)} \tag{32}$$

Secondly, we can consider a *J*-integral utilizing the bending moment in the beam, presented as Eq. 33a&b, such that:

$$J = \frac{2}{B(W-a)} \int_0^{\theta} M \, d\theta \tag{33a}$$

$$J = \frac{2}{B(W-a)} \int_0^{\theta} \frac{PL}{2} d\theta \tag{33b}$$

which simplifies to Eq. 34:

$$J = \frac{PL\theta}{Bb}. \tag{34}$$

Lastly, a more involved *P*-δ *J*-integral presented by Hutchinson and Suo gives Eq. 35 [75]:

$$J = \left(\frac{1+\beta}{1+\beta^2}\right)\frac{2A_{total}}{B(W-a)} \tag{35}$$

where β is a geometric factor (originally presented as α, but changed here to prevent confusion) as shown in Eq. 36:

$$\beta = 2\sqrt{\left(\frac{a}{W-a}\right)^2 + \left(\frac{a}{W-a}\right) + 1/2} - 2\left(\frac{a}{W-a} - \frac{1}{2}\right). \tag{36}$$

For each size of beam, a representative sample was chosen and all analysis methods outlined here were performed for comparison. Fig 67 shows these results for 2500nm beam 1. Interestingly, the ASTM E 399 method calculations show the highest *K* values, while the Bakker elastic method gives the lowest values. One might attribute this to the inherent overestimation of the E 399 method due the clamping constraints, added to the fact that these samples were not deformed to a high strain like the other beam sizes, thereby limited the amount of plasticity that occurred relatively. The Bakker method is lower than the *J*-integral methods as expected as it

uses an independent calculation of the bending stress, which has been appropriately modified to account for the clamped ends. The three types of *J*-integrals agree very well, which can be expected. Additionally, all methods show a linear increase in *K* value with *a/W*, which is much different than typical 3 point bending samples. This demonstrates the inherent stability of this testing scheme.

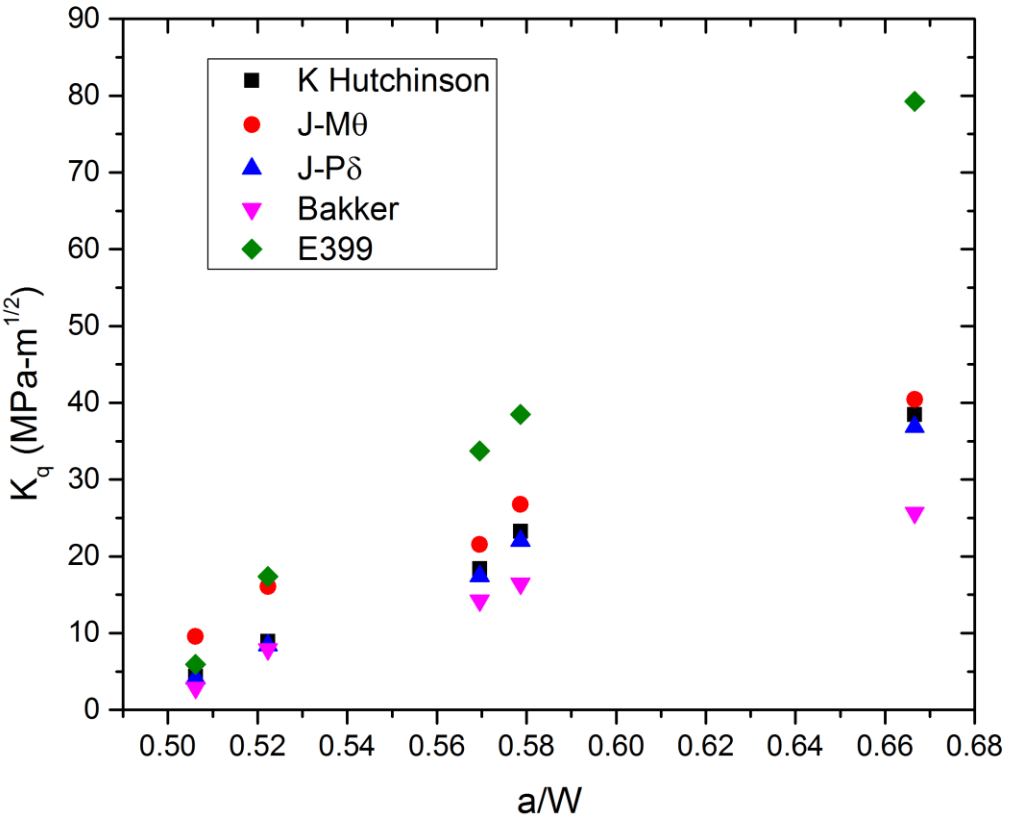

Figure 67: Comparison of K_q vs. a/W for several analysis methods for 2500nm beam 1

Fig. 68 shows the comparison of different analysis methods for 500nm beams 3 and 4. It can be observed that here the Bakker and E 399 methods align closely and give the smallest values of *K* as expected. The *J*-integral methods are almost a factor of two higher, with the *P-δ* and Hutchinson methods closely aligned. This also makes sense as they use the same general

approach; though the Hutchinson method has a small correction factor. The *M-θ J*-integral gives the highest values in this case. The essential difference in methodology is that the *P-δ* method utilizes the deformation along the axis of the indenter, which was determined from the load-displacement data, and the *M-θ* method utilizes the measured angular deflection of the beam from the video. Utilizing the load-displacement data does make the analysis more susceptible to drift and compliance issues, so perhaps the *M-θ* method is superior. The data all shows the same linear trend in *K* with *a/W* as in the 2500nm beams.

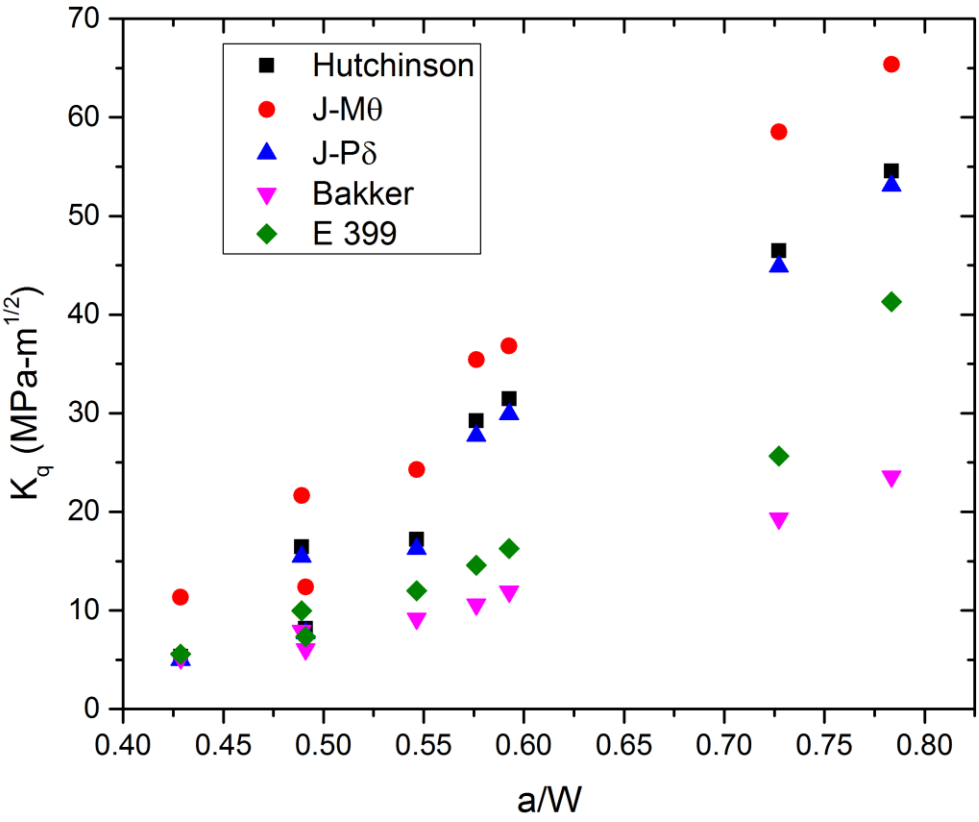

Figure 68: Comparison of K_q vs. a/W for several analysis methods for 500nm beams 3&4

Fig. 69 shows the comparison of the different analysis methods for 100nm beam 1. It can be seen that the same trends for the 500nm beams are present here. There is an even more

dramatic increase of the *M-θ* values over the *P-δ* values, which is unexpected as the indenter system is much more sensitive in this case, which should lessen drift effects. On the other hand, the much more powerful electron beam utilized in 100nm samples would represent a much higher local heating than the previous testing setup. It should also be noted that the same linear trend of *K* vs. *a/W* is observed for all methods at this size range as well.

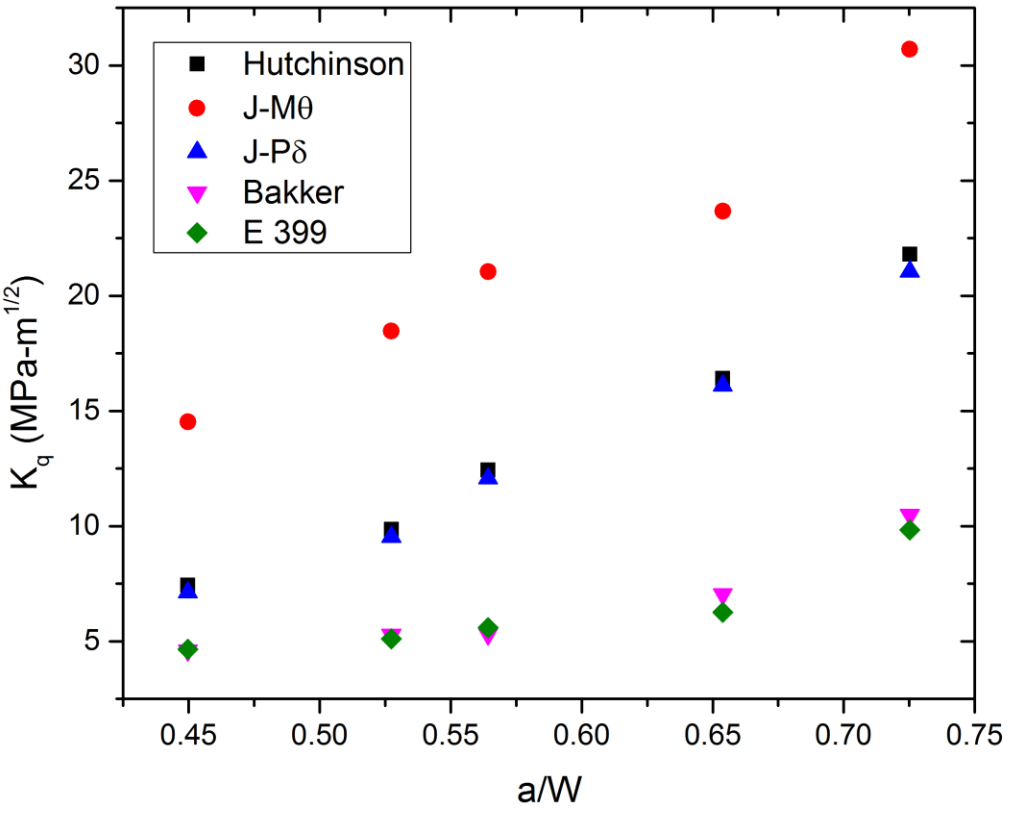

Figure 69: Comparison of K_q vs. a/W for several analysis methods for 100nm beam 1

5.2: Strain rate effect

In Fig.70, the calculated *K* values are presented vs. crack length *a* for all 2500nm beams, solely using the Hutchinson method for sake of comparison. Although the value of *K* at a given *a/W* doesn't have a strong strain rate dependence, there is a small trend of reduced K with

reduced strain rate. This is unexpected, as lower strain rates should allow for increased plasticity and thereby higher *K* values to achieve the same *a/W*. However, the trend being discussed is very weak, as the highest strain rate is lower than the second highest and this effect may merely be microstructure and error related. What is certain is that the strain rate effect, if present, is very weak for this strain rate range of only 1.5 orders of magnitude, which is comparatively is small to ranges over which they are typically observed. However, this was the maximum reasonable strain rate range of the testing equipment employed.

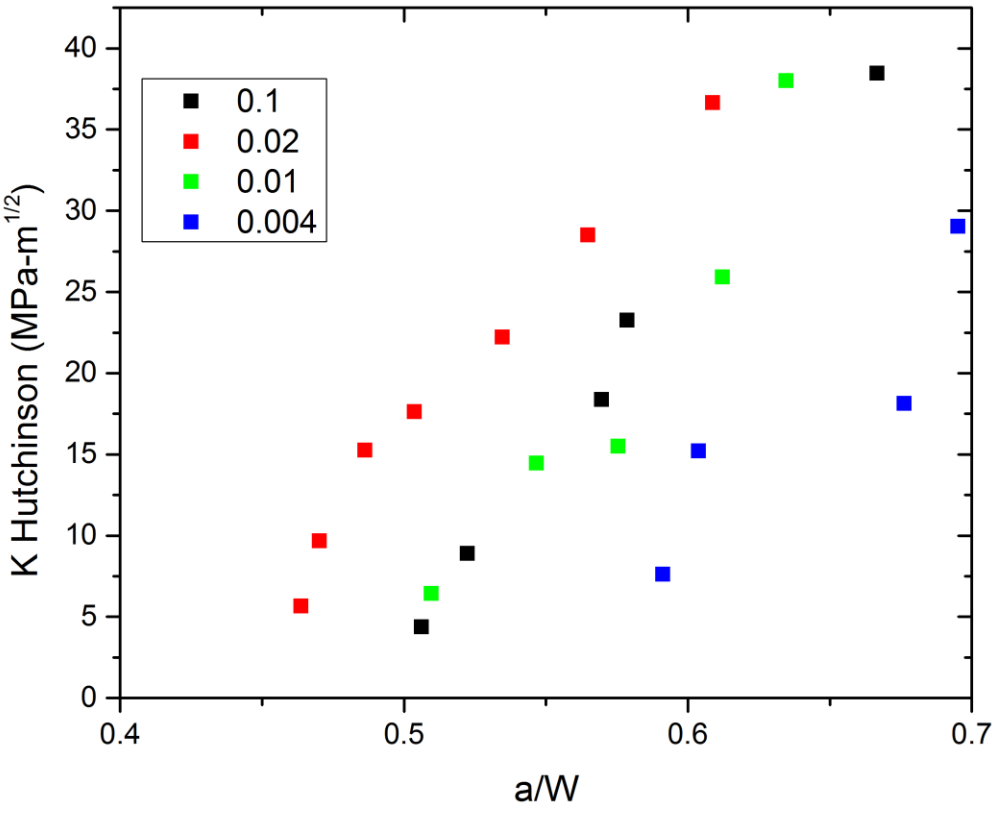

Figure 70: K_q versus a/W for the 2500nm beams

Figure 71 shows the calculated *K* values using the Hutchinson method versus *a/W* for all 500nm beams. It should be noted again that any strain rate effect is very weak, but the same

trend of increasing *K* with increasing strain rate is observed. This time, the second lowest strain rate is higher than the lowest strain rate, which suggests a rather weak correlation.

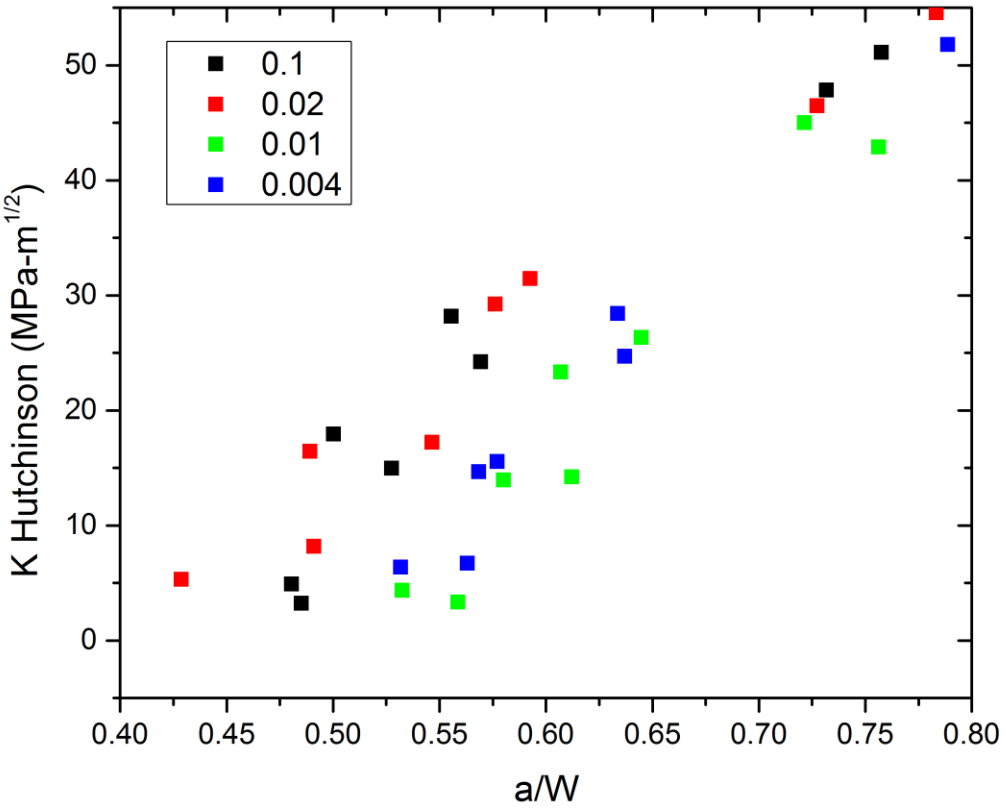

Figure 71: K_q versus a/W for the 500nm beams

Fig. 72 shows the calculated *K* values from the Hutchinson method versus *a/W* for the 100nm beams. In this case, almost no correlation between *K* at a given *a/W* and strain rate can be determined. It should also be noted that the strain rate range was even higher in this case, thanks to the enhanced sensitivity of the indenter equipment and increased speed of the video capture device used. For these beams, the strain rate ranged over 2.5 orders of magnitude. This serves to fully cast into doubt the existence of any significant strain rate effect, and that the different observed in *K* vs. *a/W* for these samples is more dependent on structural variations or

error. This is still valuable information, as it suggests future testing can be carried out at any desired strain rate to maximize video frames and minimize drift.

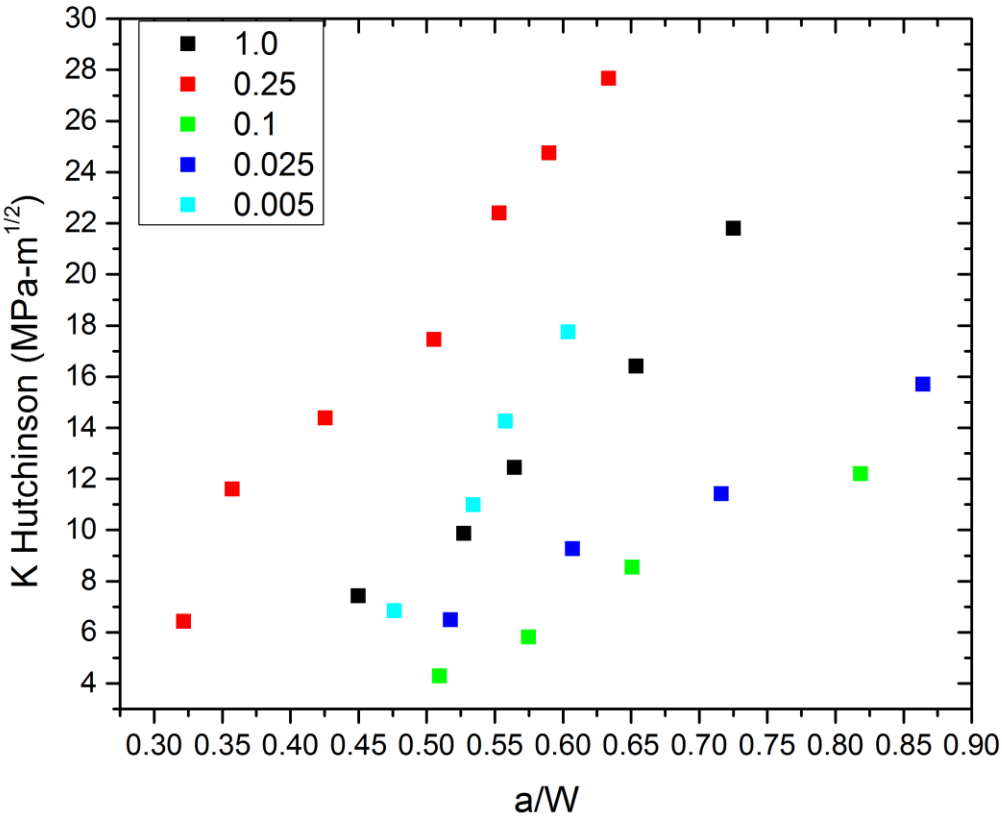

Figure 72: K_q versus a/W for the 100nm beams

5.3: Scale effect

Fig. 73 shows all *K* vs. *a/W* values for each size of beam tested. The included solid lines are power fit lines, though these were nearly linear in all cases. It can be observed that the 500nm and 2500nm fit lines align almost perfectly, while the 100nm line deviates significantly. The log-log scale accentuates this fact, but it can be seen in the other figures presented in this section that the difference in *K* values is significant nonetheless. The general observed size effects suggest that smaller is tougher, but we observe a strong opposing trend in this case. This is peculiar and more data should be gathered to come up with a definitive explanation.

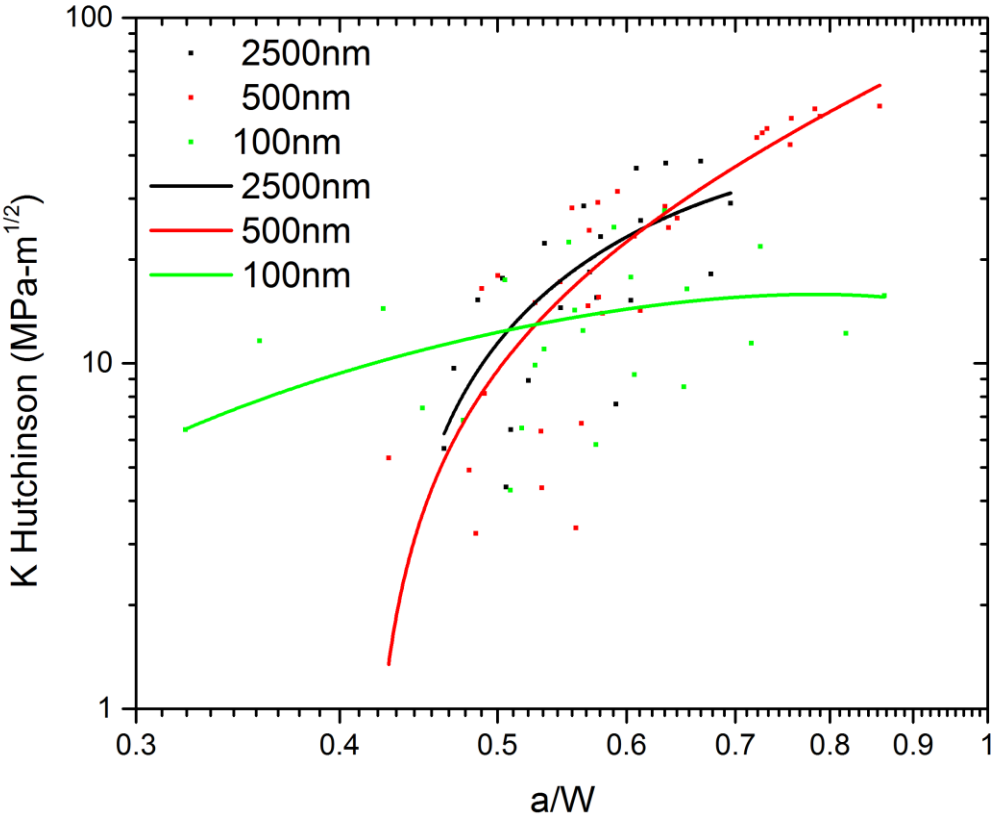

Figure 73: K_q versus a/W for all beams tested, with fit lines

The first step in explaining unexpected results is to discuss practical testing issues rather than inherent material mechanisms. It is true that the 100nm samples were tested in a different microscope and with a different indenter system. One change in particular that accompanies this is the use of a 200keV electron beam on the 100nm samples and a 10keV beam on the larger samples. This results in much higher local heating of the sample, which aids in dislocation nucleation and propagation processes. This should have the effect of increased plasticity and increased toughness, so this cannot explain the observed trend. Additionally, the tip that was used for the 100nm beams was relatively blunter compared to the size of the beams. This would have the effect of reduced stress concentration underneath the indenter and thereby reduce the

amount of dislocation injection into the specimen. Again this difference promotes higher toughness in small scale testing, not lower. Lastly, these specimens should have a higher amount of FIB damage than the larger specimens even though lower beam currents were used to finalize sample fabrication. Gallium ions have a finite penetration depth and this means the damaged portion of the sample is maximized for the smaller beams. This would have the effect of injecting imperfections, including dislocations, and even amorphization of the surface. These amorphized surfaces would serve as a barrier to dislocation termination and promote brittleness. This is therefore a possible explanation. However, the images of the 100nm beams presented in the previous section do not show a high degree of damage. It is also known that iron is a FIB resistant material, compared to other commonly studied materials such as copper and gold.

It seems likely then that real mechanistic and/or material differences are leading to the decreased toughness for the 100nm beams. With regards to a transition from plane strain to plane stress, the plastic zone size for Nitronic 50 is on the order of 100μm, so all tested specimen sizes were well into the plane stress regime. One possibility is that plasticity is enhanced in these 100nm beams as expected, but this leads to highly localized plasticity on the favored slip systems and thereby an enhanced ductile fracture mechanism by void coalescence. However, no evidence of this is observed. Another possible size effect may arise from the decreased distance from the neutral axis to the dislocation source. Since crossing the neutral axis impedes dislocation motion, the only force that exists to push the dislocations across the neutral axis is then dislocation-dislocation interactions. The reduced distance to the source relative to the larger beams means that significant back stresses could build up from this process and exhaust the dislocation sources.

Chapter 6: Conclusions

6.1: What was learned?

This report demonstrates a new type of in-situ fracture testing. The only similar method that has been published is by Jaya et al. The ability to fabricate specimens from bulk using FIB techniques to produce high quality specimens with controllable geometry, all the way from 2500nm to 100nm scale is also demonstrated. The in-situ imaging worked well and provided excellent supplementary information for the load-displacement data generated by the indenter system. Overall, despite some difficulties with analysis, this report demonstrates that this technique is viable and provides important advantages over other small scale fracture testing methods, namely increased visibility of the crack and increased mechanical stability of the crack tip.

There are some completely novel aspects of this work as well. One is the EBSD scanning of the 2500nm beams between test cycles. Although the EBSD signal diminishes with testing cycles due to contamination and severe deformation, this could prove to be a very useful technique with additional refinements. Additionally, notching of the 100nm beams using the TEM electron beam has not before been reported and is a very general technique for fracture testing at the nanoscale.

The analysis methods presented here are only rudimentary attempts, but produce good comparative values at the least. Higher level modeling, such as FEM or dislocation dynamics could be very insightful and propel this technique to be all the more powerful. Another advance that could prove useful is utilization of image correlation, to speed analysis time and allow for many data points of analyzed K values. Employing such a method could detect discrete events

in crack propagation as well as a method to calculate energy release rates from isolated regions of the sample by calculating local strains with great accuracy.

6.2: Future work

6.2.1: Hydrogen Charging

Future experiments with hydrogen charging should prove very interesting to the scientific community. As discussed in the background section, presence of impurities can have a strong effect on the BDT. Hydrogen is an impurity of particular interest due to its abundance and high diffusivity; this means it is very difficult to avoid the presence of hydrogen in materials. It has long been observed that hydrogen can embrittle a variety of metals, particularly high strength alloys. Repeating the experiments presented here after charging with hydrogen may induce a brittleness transition in Nitronic 50. Indeed, this is a cause for concern as Nitronic 50 is often used as a material for chemical plants and nuclear reactors due to its inherently high corrosion resistance, where hydrogen embrittlement is a key concern.

Hydrogen embrittlement is a contentious issue regarding the mechanisms under which it operates [50-61]. Several theories have been put forth to describe its effects; two primary ones are Hydrogen Enhanced Localized Plasticity (HELP) and Hydrogen Enhanced Decohesion (HEDE). These are both illustrated in Fig. 74b. HELP arose due to in-situ TEM experimental observations of enhanced dislocation velocities in the presence of hydrogen. The theory is that hydrogen atmospheres surround dislocations produced at crack tips (this would minimize energy due to the stress field surrounding a dislocation) and thereby reduce interaction of the dislocations' stress field with obstacles, primarily other dislocations, but also other obstacles like grain boundaries and inclusions. This allows for more highly localized plasticity, as a given slip system will be able to sustain more dislocation activity. This doesn't directly constitute a failure

mechanism, but one could theorize that this will lead to enhanced microvoid formation and coalescence into a traditional ductile crack. HEDE is an alternative mechanism that suggests hydrogen would lower the energy cost for crack surface formation, as described by the classic Griffith criterion. For some materials, hydrogen may form hydride phases with the host material, which are typically brittle. This would likely take place at high energy grain boundaries and surfaces; however, this is not a concern for iron-based alloys like Nitronic 50. These three mechanisms are not the only considerations, as it can also be expected that hydrogen would modify the dislocation nucleation process from crack tips. Specifically, the presence of hydrogen should lower the energy needed to nucleate a double kink due to its stress field, but would then lower the kink propagation velocity. In the end, it is a complicated issue that exceeds our current instrumentation limits, but continued work is essential to refinement of our currently existing models and may provide new insights regarding the mechanisms hydrogen embrittlement operates under.

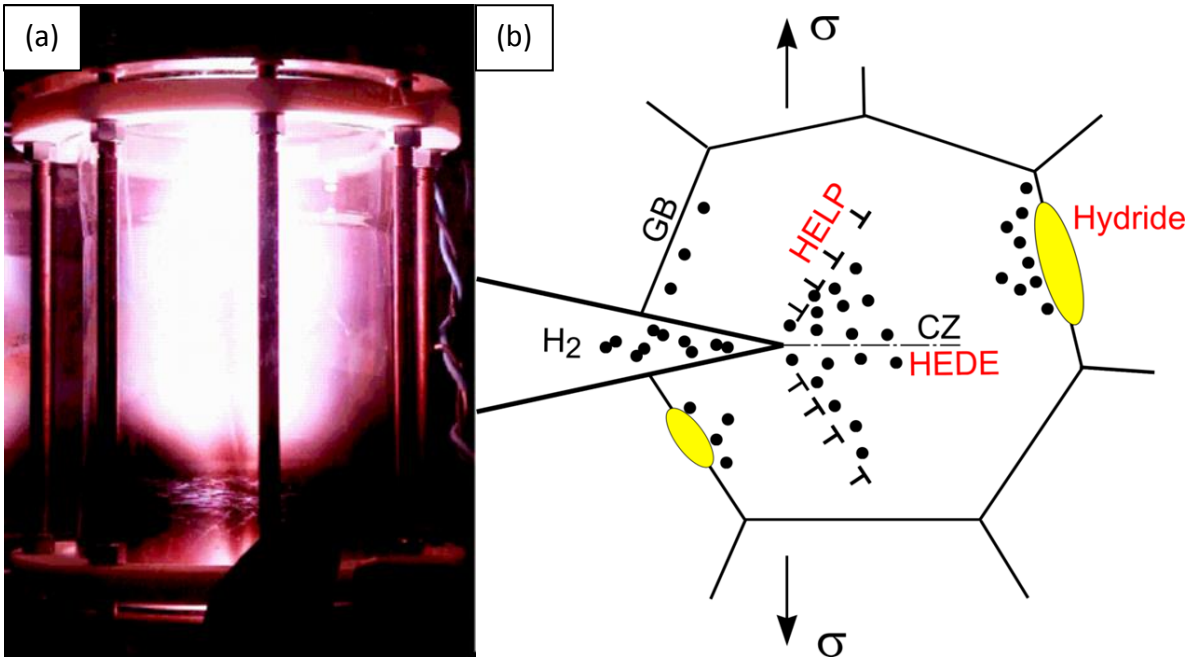

Figure 74:a) Hydrogen Plasma reactor b) illustration showing the different hydrogen embrittlement mechanisms

In order to introduce hydrogen into a material, a number of processes may be utilized. Three methods have been extensively utilized by researchers in the past: electrochemical, gas phase, and plasma methods as shown in Fig. 74a. The goal is to produce atomic hydrogen at the surface of a component and drive it into the material with high temperature diffusion. Previous work has been carried out by the author, which eliminated both electrochemical and gas phase charging methodologies for micro and nano-volumes as it is challenging to preserve the FIBed structures due to the formation of oxide that eats the structures away. It is most dramatic for electrochemical methods that rely on a redox reaction with water, however gas phase charging needs to be performed in an ultra-high purity furnace to avoid oxidation. Although no plasma reactor was available at ESI, one is available at the University of Minnesota. A comparison of pillars charged by the three methods is shown in Fig. 75.

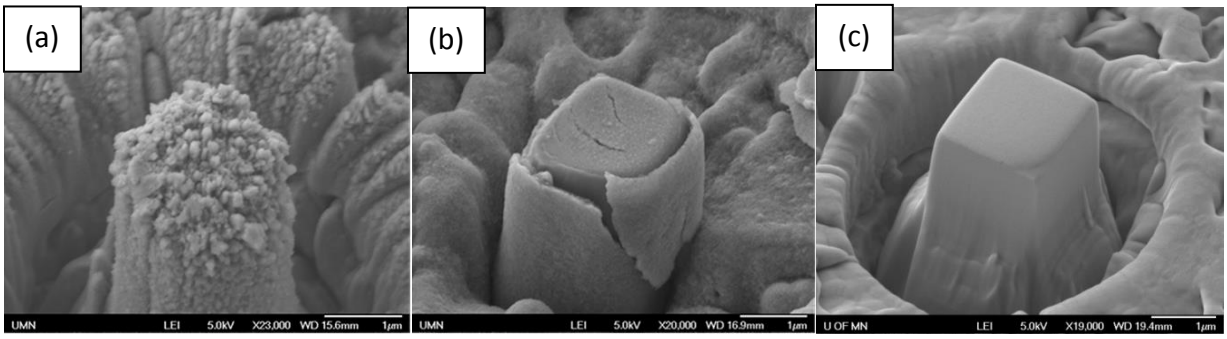

Figure 75:a) Electrochemical charged pillar b) Gas phase charged pillar c) Plasma charged pillar

It can be readily seen that the plasma charging method produces minimal damage to the pillars. Fig 76a shows the pillar in Fig. 75c after testing and the corresponding stress-strain curve is shown in Fig 76b. It can be seen that the stress values are enhanced compared to the pillar shown in the experimental section, Fig. 18 and that qualitatively it appears to have undergone more brittle behavior.

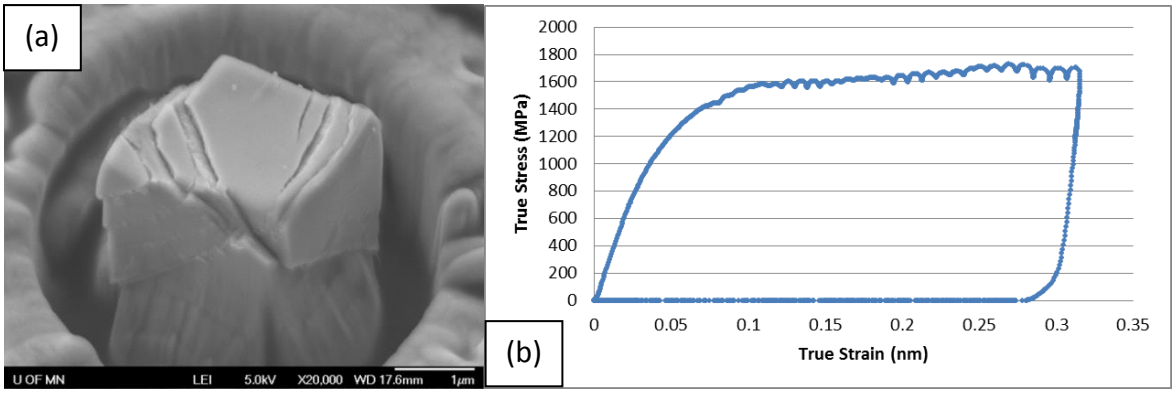

Figure 76: a) Post-compression SEM micrograph of hydrogen charged pillar b) Corresponding stress-strain curve

6.2.2: Other materials

The techniques presented in this report may be extended to other materials of interest. For metallic systems, tungsten could prove very interesting due to its inherently high brittleness for a metal and is a material that is of significant engineering interest due to its high stiffness and wear resistance, as well as a barrier layer for fusion reactors [67-70]. Another material that can be studied is Fe-3%Si. This material is almost pure iron, but by adding 3% Si, it becomes very easy to produce large single crystals. This material is typically used as a model material for a simple BCC system [62-66] and being a single crystal eases analysis issues such as grain boundaries, grain orientation and migration of alloying elements. Additionally, BCC lattices undergo very strong BDT due to their inherently higher energy dislocation processes and fewer slip systems.

With some modification to the methodologies used, the experiments presented here could also be performed on non-metallic systems that are traditionally brittle. Specifically, the electrochemical polishing steps could be replaced by ion milling or wedge polishing to produce an area of suitable thickness for FIB fabrication of test specimens. With the addition of a conductive coating for insulating materials, performing identical experiments should be possible.

These materials could potentially be induced to undergo the reverse BDT from that of metals; specifically a transition from brittle behavior to ductile. This is similar to the size effect BDT presented in the background section for Si, but could incorporate variables like strain rate and presence of hydrogen. Ductile silicon, as a basic concept, could be important technologically, as higher toughness sensors, MEMS/NEMS devices could push the types of applications they would be suitable for. Another type of non-metallic material that would be of interest would be ceramic materials that are commonly found in the earth's crust [71, 72], such as spinel, MgO, and others. There is some interest in the BDT of such materials, as this is suspected by some geologists to be important for formation of faults, and experiments on these materials could provide some insightful data that could be utilized for modeling such behavior.

References:

[1] Gerberich W.W., Mook W.M., Perrey C.R., Carter C.B., Baskes M.I., Mukherjee R., Gidwani A., Herberlein J., McMurry P.H., Girshick S.L. (2003) "Superhard silicon nanospheres." J. Mech. Phys. Solids 51, 6: 979-992

[2] Uchic M.D., Dimiduk D.M., Florando J.N., Nix W.D. (2004) "Sample dimensions influence strength and crystal plasticity." Science 305, 5686: 986-9

[3] Volkert C.A., Lilleodden E.T. (2006) "Size effects in the deformation of sub-micron Au columns." Philos. Mag. 86, 33-35: 5567-79.

[4] Oh, Sang Ho, et al. "In situ observation of dislocation nucleation and escape in a submicrometre aluminium single crystal." *Nature materials* 8.2 (2009): 95-100.

[5] Legros, M., D. S. Gianola, and C. Motz. "Quantitative in situ mechanical testing in electron microscopes." *MRS bulletin* 35.05 (2010): 354-360.

[6] Shen, Z., R. H. Wagoner, and W. A. T. Clark. "Dislocation and grain boundary interactions in metals." *Acta Metallurgica* 36.12 (1988): 3231-3242.

[7] Wurster, Stefan, et al. "Micrometer-Sized Specimen Preparation Based on Ion Slicing Technique." *Advanced Engineering Materials* 12.1-2 (2010): 61-64.

[8] Arsenault, R. J., and N. Shi. "Dislocation generation due to differences between the coefficients of thermal expansion." *Materials Science and Engineering* 81 (1986): 175-187.

[9] Kobrinsky M.J., Dehm G., Thompson C.V., Arzt E. (2001) "Effects of thickness on the characteristic length scale of dislocation plasticity in Ag thin films." Acta Mater. 49, 17: 3597-3607

[10] Zhu .T., Bushby A.J., Dunstan D.J. (2007) "Size effect in the initiation of plasticity for ceramics in nanoindentation." J. Mech. Phys. Solids

[11] Baker, S., Plastic deformation and strength of materials in small dimensions. Materials Science and Engineering, 2001. A319-321: p. 16-23

[12] Arzt E. (1998) "Size effects in materials due to microstructural and dimensional constraints: A comparative review." Acta Mater. 46, 16: 5611-5626

[13] Pippan, Reinhard, et al. "The limits of refinement by severe plastic deformation."*Advanced Engineering Materials* 8.11 (2006): 1046-1056.

[14] Omori, Mamoru. "Sintering, consolidation, reaction and crystal growth by the spark plasma system (SPS)." *Materials Science and Engineering: A* 287.2 (2000): 183-188.

[15] C.St. John: The brittle-to-ductile transition in pre-cleaved silicon single crystals. Philos. Mag. 32(6), 1193-1212 (1975).

[16] P. Gumbsch: Modelling brittle and semi-brittle fracture processes. Materials Sci. and Engng. A 319-321, 1-7 (2001).

[17] Lin, I.-H., and Thomson, R.: Cleavage, Dislocation Emission and Shielding for Cracks Under Load. Acta Metall. 34(2), 187-206 (1986).

[18] M.J. Lii, X.F. Chen, Y. Katz and W.W. Gerberich: Dislocation modeling and acoustic emission obseration of alternating ductile/brittle events in Fe-3 wt% Si crystals. Acta. Mater. 38(12), 2435-2453 (1990).

[19] M. Brede and P. Haasen, "The brittle-to-ductile transition in doped silicon as a model substance," Acta Metallurgica, 36 (1988) 2003-2018.

[20] Hertzberg, Richard W. *Deformation and fracture mechanics of engineering materials*. Vol. 89. New York: Wiley, 1996.

[21] A.H. Cottrell: *The Griffith Centenary Meeting*, Institute of Materials, London, UK, 1993, pp. 4-15.

[22] A.H. Cottrell: *Proc. Roy. Soc. A*, 1963, vol. 279, pp. 1-10.

[23] Amelinckx, Severin. *The direct observation of dislocations*. Vol. 964. New York: Academic Press, 1964.

[24] D. Hull and D.J. Bacon. Introduction to Dislocations. 3rd Edition. International Series on Materials Science and Technology, Volume 37. Pergamon Press. 1984

[25] Hirth, John P., and Jens Lothe. "Theory of dislocations." (1982).

[26] R. Peierls, Proc. Phys. Soc. London 52, 34 (1940).

[27] F.R.N. Nabarro, Proc. Phys. Soc. London 59, 256 (1947).

[28] Schmid, Erich, and Walter Boas. "Plasticity of crystals." (1950).

[29] Dugdale, D. S. "Yielding of steel sheets containing slits." *Journal of the Mechanics and Physics of Solids* 8.2 (1960): 100-104.

[30] Bilby, B. A., A. H. Cottrell, and K. H. Swinden. "The spread of plastic yield from a notch." *Proceedings of the Royal Society of London. Series A. Mathematical and Physical Sciences* 272.1350 (1963): 304-314.

[31] McMeeking, Robert M. "Finite deformation analysis of crack-tip opening in elastic-plastic materials and implications for fracture." *Journal of the Mechanics and Physics of Solids* 25.5 (1977): 357-381.

[32] Rice, James R. "A path independent integral and the approximate analysis of strain concentration by notches and cracks." *Journal of applied mechanics* 35.2 (1968): 379-386.

[33] A. Kelly, W.R. Tyson and A.H. Cottrell: Ductile and brittle crystals. Philos. Mag. 15(135), 567-586 (1967).

[34] A.H. Cottrell and B.A. Bilby: Dislocation theory of yielding and strain ageing in iron. Proc. Phys. Soc. A 62(1), 49 (1949).

[35] Johnson, Gordon R., and William H. Cook. "Fracture characteristics of three metals subjected to various strains, strain rates, temperatures and pressures."Engineering fracture mechanics 21.1 (1985): 31-48.

[36] Schulson, E. M., and D. R. Barker. "A brittle to ductile transition in NiAl of a critical grain size." Scripta metallurgica 17.4 (1983): 519-522.

[37] F. Östlund, K. Rzepiejewska-Malyska, K. Leifer, L.M. Hale, Y. Tang, R. Ballarini, W.W. [38] Gerberich, J. Michler, Adv. Funct. Mater. 19 (15), 2439 (2009).

[38] Srawley, John E. "Wide range stress intensity factor expressions for ASTM E 399 standard fracture toughness specimens." *International Journal of Fracture*12.3 (1976): 475-476.

[39] Designation, A. S. T. M. "E399-90. Standard test method for plane-strain fracture toughness of metallic materials." *1991 Annual Book of ASTM Standards* 3 (1997): 485-51.

[40] San Paulo, A., et al. "Mechanical elasticity of single and double clamped silicon nanobeams fabricated by the vapor-liquid-solid method." *Applied Physics Letters* 87.5 (2005): 053111.

[41] Jaya B, Nagamani, Vikram Jayaram, and Sanjay Kumar Biswas. "A new method for fracture toughness determination of graded (Pt, Ni) Al bond coats by microbeam bend tests." *Philosophical Magazine* 92.25-27 (2012): 3326-3345.

[42] Pugno, N. "Predictions of strength in MEMS components with defects - a novel experimental-theoretical approach." International journal of solids and structures 42.2 (2005):647-61.

[43] Drory, M. D., et al. "Fracture of synthetic diamond." *Journal of applied physics*78.5 (1995): 3083-3088.

[44] Armstrong, D. E. J., et al. "Nanoindentation and micro-mechanical fracture toughness of electrodeposited nanocrystalline Ni–W alloy films." *Thin Solid Films* 520.13 (2012): 4369-4372.

[45] Bei H. Shim S. Miller M.K., Pharr G.M., George E.P. (2007b) “Effects of focused ion beam milling on the nanomechanical behavior of a molybdenum-alloy single crystal.” Appl. Phys. Lett. 91, 11: 111915

[46] S. Shim, H. Bei, M.K. Miller, G.M. Pharr, E.P. George, Effects of focused ion beam milling on the compressive behavior of directionally solidified micropillars and the nanoindentation response of an electropolished surface, Acta Materialia, Volume 57, Issue 2, January 2009, Pages 503-510, ISSN 1359-6454, 10.1016/j.actamat.2008.09.033

[47] Kiener, D., et al. "Advanced nanomechanics in the TEM: effects of thermal annealing on FIB prepared Cu samples." *Philosophical Magazine* 92.25-27 (2012): 3269-3289.

[48] Giannuzzi, Lucille A., Remco Geurts, and Jan Ringnalda. "2 keV Ga+ FIB milling for reducing amorphous damage in silicon." *Microscopy and Microanalysis* 11.S02 (2005): 828-829.

[49] Kato, Naoko I. "Reducing focused ion beam damage to transmission electron microscopy samples." *Journal of electron microscopy* 53.5 (2004): 451-458.

[50] C.A. Zapffe and C. Sims, Trans. AIME 145 (1941) 225.

[51] C.A. Zapffe, Annual Report of the Smithsonian Institution Pub. 4062 (1951) 316.

[52] N.O. Petch and P. Stables, Nature 169 (1952) 842.

[53] A.S. Tetelman and W.D. Robertson, Trans. AIME 224 (1962) 775.

[54] A.S. Tetelman and s. Kunz, in Stress-corrosion cracking and hydrogen embrittlement of iron-based alloys, edited by R.W. Stahle (NACE. Proc., Firminy, France, 1973) p. 359

[55] W.W. Gerberich, P.G. Marsh, J.W. Hoehn, in “Hydrogen Effects on Materials”, edited by A.W. Thompson and N.R. Moody (TMS, Warrendale, PA, 1996) p.539

[56] C.D. Beachem, Metall. Trans. 3 (1972) 437.

[57] I.M. Robertson and H.K. Birnbaum, Acta. Metall. 34 (1986) 353.

[58] J. Eastman, F. Heubaum, T. Masumoto and H.K. Birnbaum, Acta. Metall. 30 (1982) 1579.

[59] H.K. Birnbaum and P. Sofronis, in “Hydrogen Effects in Materials”, edited by A.W. Thompson and N.R. Moody (TMS, Warrendale, Pa, 1996).

[60] C. Altstetter and D. Abraham, in ‘Hydrogen Effects in Materials”, edited by A.W. Thompson and N.R. Moody (TMS, Warrendale, Pa, 1996) p. 599

[61] P.D. Hicks and C.J. Altstetter, in “Hydrogen embrittlement of superalloys”, edited by A.W. Thompson and N.R. Moody (TMS, Warrendale, Pa, 1989) p. 613.

[62] Hook, R. E., and J. P. Hirth. "The deformation behavior of isoaxial bicrystals of Fe-3% Si." Acta Metallurgica 15.3 (1967): 535-551.

[63] Furubayashi, Ei-ichi. "Behavior of Dislocations in Fe-3% Si under Stress."Journal of the Physical Society of Japan 27.1 (1969): 130-146.

[64] Y.Qiao and A.S. Argon: Brittle to ductile transition of cleavage fracture by thermal crack arrest in Fe-3%Si single crystals. Mech. Mater 35(1), 903-912 (2003).

[65] W.W. Gerberich, P.G. Marsh and H. Huang: The effect of local dislocation arrangements on hydrogen-induced cleavage. Fundamental Aspects of stress Corrosion Cracking, TMS/ASM Parkins Symposium, TMS Warrendale, Pa. 191-204 (1992).

[66] P. G. Marsh: Prediction of fracture toughness, stress-corrosion cracking thresholds and corrosion fatigue thresholds in iron-base materials. PhD Thesis, University of Minnesota (1994).

[67] P. Gumbsch: Modelling brittle and semi-brittle fracture processes. Materials Sci. and Engng. A 319-321, 1-7 (2001).

[68] Wurster, Stefan, Christian Motz, and Reinhard Pippan. "Characterization of the fracture toughness of micro-sized tungsten single crystal notched specimens."Philosophical Magazine 92.14 (2012): 1803-1825.

[69] Causey, Rion A., and Thomas J. Venhaus. "The use of tungsten in fusion reactors: a review of the hydrogen retention and migration properties." Physica scripta 2001.T94 (2001): 9.

[70] Neu, R., et al. "Tungsten: an option for divertor and main chamber plasma facing components in future fusion devices." Nuclear fusion 45.3 (2005): 209.

[71] Demouchy, S., S.J. Mackwell, and D.L. Kohlstedt (2007) Influence of hydrogen on Fe-Mg interdiffusion in (Mg,Fe)O and implications for Earth’s lower mantle, Contrib. Mineral. Petrol. 154:279-289, doi:10.1007/s00410-007-0193-9.

[72] Kohlstedt, D.L. (2006) Water and rock deformation: The case for and against a climb controlled creep rate, in Water in Nominally Anhydrous Minerals, eds. H. Keppler and J.R.Smyth, Reviews in Mineralogy and Geochemistry, vol. 62, MSA, pp. 377-396.

[73] A.D. Bakker, “Evaluation of Fracture Mechanics Parameters for Bend Specimens,” Intern. J. Fracture, 71 (1995) 323-343

[74] X-K. Zhu and J.A. Joyce. Engineering Fracture Mechanics, 85 (2012) 1-46

[75] Hutchinson, John W., and Zhigang Suo. "Mixed mode cracking in layered materials." Advances in applied mechanics 29.63 (1992): 191.

[76] W.W.Gerberich, D.D. Stauffer, A.R. Beaber and N.I. Tymiak: A brittleness transition in silicon due to scale. J. Materials Res. 27(3), (2012), 552-561.

[77] Moser, G., et al. "Sample preparation by metallography and focused ion beam for nanomechanical testing." Practical Metallography 49.6 (2012): 343-355.

List of Figures: